

Department of Physics and Astronomy
University of Heidelberg

Master thesis
in Physics
submitted by

Daniel Baitinger
born in Sinsheim (Germany)
2019

Secondary discharge studies in a single-GEM detector in the scope of the ALICE TPC upgrade

This Master thesis has been carried out by Daniel Baitinger
at the
Physikalisches Institut at the University of Heidelberg
and the
GSI Helmholtzzentrum für Schwerionenforschung
under the supervision of
Prof. Dr. Silvia Masciocchi

Sekundäre Entladungsstudien in einem Detektor mit einzelner GEM für die Umrüstung der ALICE Zeitprojektionskammer:

Um die begrenzte Ausleserate der ALICE Zeitprojektionskammer zu überwinden, werden ihre Vieldrahtkammern während der zweiten, langen Stilllegung des LHC (2019–2020) durch eine kontinuierliche Auslese ersetzt, die auf Gas Elektron Vervielfältiger (GEM) Folien basiert. Eine hohe Dichte an Ionisationsladungen in unmittelbarer Nähe eines GEMs kann eine primäre Entladung zwischen der oberen und unteren GEM Elektrode verursachen. In moderaten elektrischen Feldern kann eine sekundäre Entladung durch den Zwischenraum neben dem GEM folgen. Diese kraftvollen Entladungen riskieren eine irreparable Beschädigung der Auslese.

In dieser Masterarbeit werden die Eigenschaften der sekundären Entladungen untersucht, um den zugrundeliegenden Mechanismus besser zu verstehen. Es wurde herausgefunden, dass die Extraktion von Ionen oberhalb des GEMs eine sekundäre Entladung unterhalb des GEMs nicht beeinflusst. Des Weiteren wird die Abhängigkeit vom Elektrodenmaterial untersucht. Das Umkehren des elektrischen Feldes zeigt, dass das Vorkommen sekundärer Entladungen in einem ansonsten identischen Aufbau, in erster Näherung, nur von der Stärke des Feldes abhängt. Die Reduzierung der Wahrscheinlichkeit von sekundären Entladungen durch Widerstände im Stromversorgungspfad wird durch Potentialveränderungen des GEMs nach der primären Entladung erklärt. Außerdem wird der Einfluss verschiedener Gasmischungen untersucht. Diese Arbeit ist Teil einer koordinierten Untersuchung. Jüngste Ergebnisse von Studien mit einem ähnlichen Detektor führten zu einem Vorschlag eines Mechanismus für sekundäre Entladungen, welcher im Zusammenhang mit dieser Arbeit diskutiert wird.

Secondary discharge studies with a single-GEM detector in the scope of the ALICE TPC upgrade:

To overcome the limited readout rate of the ALICE Time Projection Chamber (TPC), its multi-wire proportional chambers are replaced during the LHC long shutdown 2 (2019–2020), with a continuous readout, based on gas electron multiplier (GEM) foils. A high density of ionization charges in the vicinity of a GEM can induce a primary discharge between the top and bottom electrode of the GEM. At moderate electric fields, a secondary discharge through a gap adjacent to the GEM can follow. These powerful discharges risk to damage the readout irreparably.

In this thesis, the characteristics of the secondary discharges are studied in an attempt to understand the underlying mechanism. It is found that the ion extraction at the top of the GEM has no influence on secondary discharges underneath the GEM. Furthermore, the dependence on the electrode material is studied. Reversing the electric field reveals that the occurrence of secondary discharges, to first order, only depends on the strength of the electric field. The mitigation of secondary discharges via resistors in the high-voltage supply path is linked to changes of the GEM potentials after the primary discharge. Moreover, the influence of different gas mixtures is investigated. This work is part of a coordinated effort. Recent results from studies conducted on a similar detector resulted in the proposal of a mechanism for the secondary discharge, which will be discussed in the context of this thesis.

Acknowledgement

The past year has been a time full of new experiences and challenges. Many people have contributed to my scientific, but also my personal progress. I am very grateful for this time and will look back on it with fond memories.

First and foremost, I thank Prof. Masciocchi for the opportunity to spend several months at CERN. Not only is it a great place to conduct research, but it also gave me the opportunity to see ALICE and many steps of the ALICE TPC upgrade. The remaining time at GSI, I felt very welcomed and I will miss the great atmosphere in the group. I also want to thank you, Silvia, for the many rounds of discussions, your advice, and also your hospitality in general.

I also want to thank Dr. Garabatos for the supervision of my research at CERN. With your vast experience and knowledge about gaseous detectors, you provided excellent guidance. You were also kind enough to use any opportunity to show me around CERN, especially everything ALICE (TPC upgrade) related.

Furthermore, I want to thank A. Berdnikova for always having a helping hand when I encountered an unknown or problematic situation in La Totale. You always found some time to teach me about the detector.

Outside of the laboratory, A. Deisting often provided advice for software solutions and participated in many physics discussions. Thank you for your support, Alexander!

For the contribution of helpful comments on my thesis and the valuable explanations of physics in general, I would like to thank especially R. Aeverbeck, D. Miskowiec and K. Schweda.

I am profoundly grateful to Prof. Hansmann-Menzemer, not only for reviewing this thesis, but also for the numerous great lectures and seminars I could participate in. I have been able to see many different aspects of experimental high-energy physics through your teachings, and I believe that my education and studies benefited greatly from it.

The time I experienced at CERN and GSI would not have been the same without the friends I made along the way. I want to thank especially R. Negrão De Oliveira, F. Flor, B. Blidaru and P. Becht for the many discussions and activities we have had together.

For her endless (mental) support, even during the most stressful times, I thank my partner Anne Winkens.

Außerdem möchte ich meinen Eltern danken. Ohne eure Unterstützung während meines gesamten Studiums wäre es mir nicht möglich gewesen, das Studium auf diese Art und Weise zu erleben.

Contents

1	Introduction	8
2	A Large Ion Collider Experiment	10
2.1	The strong interaction in the Standard Model of particle physics . . .	10
2.2	The quark-gluon plasma	12
2.2.1	Quark-gluon plasma in the experiment	13
2.2.2	Experimental observables	13
2.3	The ALICE experiment	18
2.3.1	Design requirements	18
2.3.2	Detectors	19
2.4	The ALICE time projection chamber	21
2.4.1	Design	22
2.4.2	Working principle	22
2.4.3	Operation with MWPC	26
3	ALICE TPC upgrade	31
3.1	Motivation	31
3.2	Gas Electron Multipliers	32
3.2.1	Production	33
3.2.2	Working principle	33
3.3	Design and performance	36
3.3.1	Requirements on the readout chambers	36
3.3.2	Readout chamber design and operation	37
4	Discharges in GEM based detectors	41
4.1	Streamer mechanism	41
4.1.1	Spark formation	43
4.2	Primary discharges	44
4.3	Secondary discharges	52
4.4	Consequences for the operation of GEM stacks	57
5	Secondary discharge studies	62
5.1	Setup	62
5.1.1	Readout	65
5.1.2	Counting of discharges	65
5.2	Methods	69
5.2.1	Inducing discharges	69

5.2.2	Measurement procedure	70
5.2.3	Conditioning of GEMs	71
5.2.4	Permanent short circuits in GEMs and recovery	72
5.3	Definition of measurement variables and uncertainties	72
5.3.1	Secondary discharge probability	72
5.3.2	Time between primary and secondary discharge	73
5.4	Exchanging and recovering GEMs	77
5.5	Drift field dependence	79
5.5.1	Measuring with reversed drift field	79
5.5.2	Results	80
5.6	Influence of the GEM material	81
5.6.1	Results	83
5.7	Influence of the direction of the induction field	84
5.7.1	Secondary discharge probability and time measurement	86
5.7.2	Inspecting the charge flow with antennas	87
5.8	Mitigation of secondary discharges using decoupling resistors	95
5.8.1	General observations	95
5.8.2	Effect of the decoupling resistor on the secondary discharge probability	98
5.8.3	Determining the time between primary and secondary discharges	98
5.8.4	Potential evolution after the primary discharge as driving factor of secondary discharge mitigation	103
5.8.5	Comparison to previous measurements	107
5.9	Employing different gas mixtures	108
5.9.1	Secondary discharge probability and time difference	108
5.9.2	Further investigations	109
5.9.3	Possible mechanism to explain secondary discharges and discussion	114
6	Summary	116
	Appendices	118
A	Supplementary plots	119
A.1	Normalized secondary discharge probability	119
A.1.1	Influence of different GEM materials	119
A.1.2	Employing different gas mixtures	120
A.2	Antenna signals with 200 MHz bandwidth	121
A.3	Time analysis software output	123
B	High voltage settings and measurement data	125
B.1	Drift field dependence	125
B.2	Influence of the GEM material	127
B.3	Influence of the direction of the induction field	128

B.4	Mitigation of secondary discharges using decoupling resistors	129
B.5	Employing different gas mixtures	130
C	Time distribution of secondary discharges	132
C.1	Drift field dependence	132
C.2	Influence of the GEM material	136
C.3	Influence of the direction of the induction field	138
C.4	Mitigation of secondary discharges using decoupling resistors	142
C.5	Employing different gas mixtures	145
D	Bibliography	150

1 Introduction

One of the four main experiments at the Large Hadron Collider (LHC) at CERN is A Large Ion Collider Experiment (ALICE). It is dedicated to the study of heavy-ion collisions, in which a state of matter is created where quarks and gluons are deconfined. This so-called quark-gluon plasma is assumed to having been the predominant state of matter a few microseconds after the Big Bang.

The main tracking device of ALICE is the Time Projection Chamber (TPC). Excellent tracking and particle identification, down to momenta as low as 100 MeV/c, in high-multiplicity environments make it an important tool to study the quark-gluon plasma. Until the end of LHC Run 2 (December 2018), the signal creation in the ALICE TPC has been governed by Multi-Wire Proportional Chambers (MWPCs). A gating grid ensures that ions, which are produced during the signal creation in a MWPC, do not enter the drift region, where they would cause large drift field distortions.

The gating grid, however, limits the operation of the TPC to a maximum collision rate of about 3 kHz. After the Long Shutdown 2 (LS2) of the LHC (2019-2020), a lead-lead collision rate of 50 kHz will be provided. In order to cope with the increased collision rate, the MWPCs will be replaced, during the ALICE TPC upgrade in LS2, with Gas Electron Multipliers: a layer of insulating material sandwiched between two copper electrodes, with a regular hole pattern through all layers. A high voltage difference between the electrodes leads to electron amplification through the holes. Stacks of four GEMs will provide a continuous readout with sufficient signal amplification, while limiting the ion backflow (IBF) into the drift volume to a maximum of 1%. A sophisticated tracking algorithm is going to correct drift field distortions, which are caused by the IBF, so that the tracking and the particle identification performance are maintained after the ALICE TPC upgrade.

A high density of ionization charges close to the GEMs pose a risk to the operation of the readout, as the presence of a high charge density in a single hole might lead to an electrical discharge between the GEM top and bottom electrode. In moderate electric fields, the initial discharge can be followed by a *secondary discharge* between two adjacent GEMs or a GEM and the readout anode. A large amount of energy is released during such discharges, which threatens to permanently damage a GEM. As the readout chambers of the upgraded TPC will not be able to be repaired or replaced until the end of LHC Run 4 (2029), the phenomenon of secondary discharges needs to be understood, so that adequate safety measures can be put in place. This work aims at characterizing the secondary discharges, so that eventually the underlying mechanism can be understood.

The thesis is organized as follows: In Chapter 2, a summary of the characteristics

of the strong interaction (Sec. 2.1), which are relevant for the creation and evolution of the quark-gluon plasma (Sec. 2.2), is given. Based on the experimental observables in heavy-ion collisions, the detectors of ALICE are introduced (Sec. 2.3), with a special focus on the time projection chamber (Sec. 2.4). The upgrade plans for the TPC are presented in Chapter 3. After discussing the need for the upgrade in Section 3.1, gas electron multipliers are introduced (Sec. 3.2) and put into the context of the ALICE TPC upgrade (Sec. 3.3).

The phenomenon of discharges in GEM based detectors is introduced in Chapter 4. Based on the streamer mechanism (Sec. 4.1), discharges between a GEM's top and bottom electrode, so-called primary discharges, are discussed in detail. Section 4.3 summarizes the main aspects, that have been found before the writing of this thesis, regarding secondary discharges. This section also serves as a basis and motivation for the measurements conducted in this work. The consequences of discharges for the operation of the TPC are discussed in Sec. 4.4.

Chapter 5 focuses on the study of secondary discharges in a small detector with a single $10 \times 10 \text{ cm}^2$ GEM. The setup is described in Section 5.1, followed by an explanation of the methodology of the measurements (Sec. 5.2). Important quantities, and their uncertainties, for the following studies are presented in Sec. 5.3. Throughout this thesis, the GEM in the detector had to be exchanged several times or had to be recovered from damage. Section 5.4 gives an estimate of the uncertainties introduced by the mechanical changes in the setup and by the recovery method. The dependence of secondary discharges on the ion extraction of the GEM is investigated in Sec. 5.5 by varying and reversing the electric field between the GEM and the cathode. By comparing a GEM with aluminium electrodes to measurements with the regular copper GEMs, the material dependence of secondary discharges is tested (Sec. 5.6). Reversing the field direction in the gap in which secondary discharges are triggered reveals that they occur at similar field strengths (Sec. 5.7). In addition, the current changes in the high-voltage supply path during discharges are measured with antennas for both field directions (Sec. 5.7.2). The mitigation of secondary discharges to happen at higher electric fields, by the addition of a resistor to the GEM bottom, is linked to the potential evolution of the GEM after a primary discharge (Sec. 5.8). The dependence of secondary discharges on different gas mixtures, including the baseline gas mixture for the ALICE TPC upgrade Ne-CO₂-N₂ (90-10-5), is measured in Sec. 5.9. Based on this measurement, and the previously obtained results, further investigations at CERN were started. They are outlined in Sec. 5.9.2, and a mechanism for the secondary discharge is proposed and discussed in Section 5.9.3.

2 A Large Ion Collider Experiment

A *Large Ion Collider Experiment* (ALICE) [1] is one of the four main experiments at the *Large Hadron Collider* (LHC) at CERN near Geneva, Switzerland. For one month per year, the LHC collides heavy ions at ultra-relativistic energies. In such collisions, a medium with extremely high temperature and energy density, the so-called *Quark-Gluon Plasma* (QGP), is created for a short time, where quarks and gluons can move freely. Interactions in and with this medium, as well as its evolution, are dominated by the strong interaction in the Standard Model of particle physics. Studying the properties of the QGP, one can gain new insights into the strong interaction, especially into its multi-particle aspects.

ALICE is dedicated to measurements of heavy-ion collisions in order to study the properties of the QGP. The main focus is on collisions of lead nuclei (Pb). Additionally, proton-lead (p-Pb) collisions are recorded. Collisions of protons (pp) are also studied, in order to provide a reference for the heavy-ion programme. In 2017, a short xenon-xenon (Xe-Xe) run was recorded, in order to compare different system sizes. A multi-purpose detector system is employed to investigate as many probes of the QGP as possible.

In section 2.1, the properties of the strong interaction relevant for the production and evolution of the QGP are briefly discussed. Then, basic properties of this medium and how it can be probed are presented (Sec. 2.2). Finally, an overview of the ALICE detector system is given (Sec. 2.3), with a focus on the *Time Projection Chamber* (TPC) in Section 2.4.

2.1 The strong interaction in the Standard Model of particle physics

The Standard Model of particle physics describes the fundamental particles we know, as well as the interactions between them. Of the three interactions, the electromagnetic, weak and strong interaction, only the latter is discussed here, since it is the main object of interest of heavy-ion collisions.

The strong interaction is described by *Quantum Chromodynamics* (QCD), a relativistic quantum field theory that is symmetric under SU(3) transformation. The relevant quantum number of particles participating in the strong interaction is the colour charge. While (anti-)quarks only carry one of the three (anti-)colours, the mediator particle, the gluon, carries a combination of colour and anti-colour. However, colour-charged objects cannot be directly observed. Instead, only bound states in the form of colour-neutral objects exist in nature. These can either be a combination

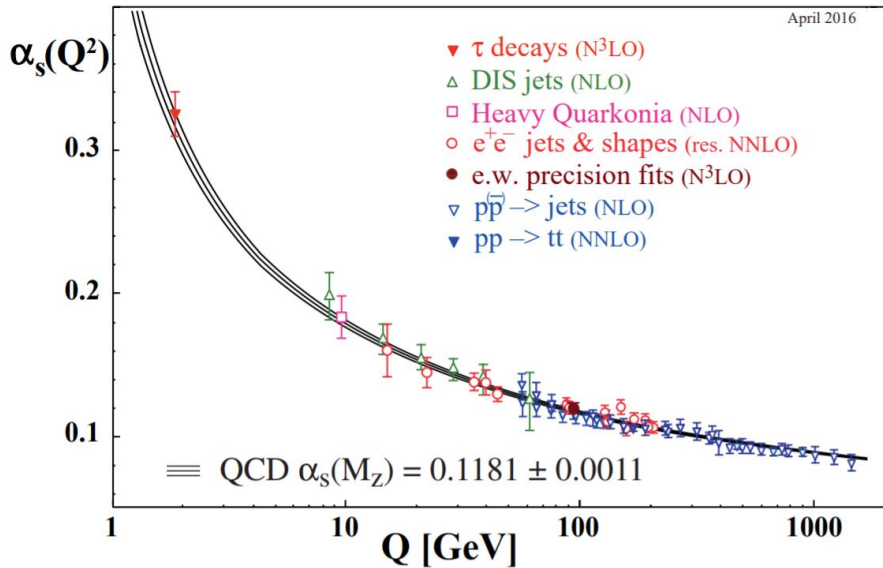


Figure 2.1: Summary of measurements of the strong coupling constant α_S as a function of the energy scale Q . The order of QCD perturbation theory used is indicated in brackets. NLO corresponds to the next-to-leading order, NNLO to the next-to-NLO and so forth [5].

of all three (anti-)colours to build a (*anti*-)baryon or the combination of colour and anti-colour to create a *meson*, for example the proton and pion, respectively. The experimentally well established fact that quarks do not appear as free particles, but only in bound states, is called *confinement* [2]. This phenomenon is not fully understood yet, but is related to the potential of a quark-antiquark pair, which can phenomenologically be described by the Cornell potential [3]:

$$V(r) = -\frac{4}{3} \frac{\alpha_S}{r} + \kappa r, \quad (2.1)$$

where α_S is the coupling constant of the strong interaction. Due to the linear part of the potential, the attractive force between a quark and an antiquark increases towards higher distances r . The strength of this force is of the order of $\kappa = 1 \text{ GeV fm}^{-1}$ [4]. Hence, the energy in the field between the partons increases until it is energetically favourable to produce a new, colour-neutral $q\bar{q}$ -pair. In general, the formation of colour-neutral bound states is called *hadronisation*.

The strong coupling constant cannot be directly measured in experiments. Nevertheless, it can be determined through perturbative calculations of experimental observables that depend on α_S . Calculations employing perturbation theory require series expansions in powers of α_S to converge. Hence, they are only applicable when $\alpha_S < 1$.

Figure 2.1 shows the dependence of the strong coupling constant on the four-momentum transfer Q between two strongly interacting particles. As Q increases (and therefore the distance between the particles decreases), the strong coupling

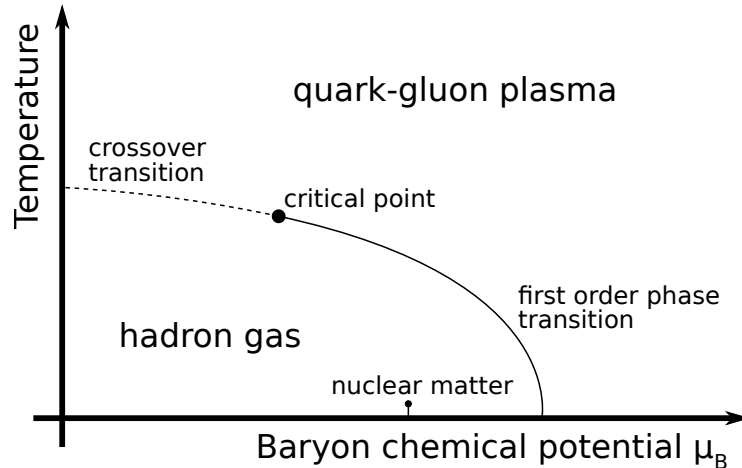


Figure 2.2: Sketch of the QCD phase diagram with respect to temperature and baryon chemical potential. The first order phase transition between two states of QCD matter is depicted as a solid black line and ends at the critical point. At lower μ_B , a crossover between hadron gas and QGP is indicated.

constant decreases. In regimes where the distance between two quarks is smaller than a nucleon radius (≈ 0.9 fm), the quarks are *asymptotically free*, which means they can move quasi-freely over small distances.

In the regime of extreme temperatures or densities, the momentum transfer (distance) between partons becomes large (small). Hence, the linear part of the potential (Eq. 2.1) decreases, which leads to a *deconfined* state of matter, where colour-charged particles move freely over distances much larger than the dimensions of a nucleon [6].

2.2 The quark-gluon plasma

The deconfinement of quarks and gluons at high energy densities or temperatures leads to a state of matter, the quark-gluon plasma, where the partons move freely. Figure 2.2 shows the phase diagram of QCD matter¹ as a function of temperature and baryon chemical potential μ_B , where the latter describes the energy needed to add a baryon to the system and is directly related to the net baryon density of the system.

The properties of the QGP, as well as the transition from ordinary hadronic matter to the quark-gluon plasma, are at the forefront of current research. For the purpose of studying the QGP, it can be created in the laboratory. This is achieved in nucleus-nucleus collisions at various accelerator facilities, such as the CERN LHC,

¹QCD matter refers to all matter that is composed of particles carrying colour charge.

the Relativistic Heavy Ion Collider (RHIC) at the Brookhaven National Laboratory in New York, USA or, in the future, at the Facility for Antiproton and Ion Research (FAIR) in Darmstadt, Germany. By using different centre-of-mass energies per nucleon-nucleon pair $\sqrt{s_{NN}}$ and various sizes of the colliding nuclei, different aspects of the phase diagram can be studied.

The transition between ordinary nuclear matter and a QGP occurs at a *critical temperature* T_C of the order of 150 MeV. A temperature of 100 MeV corresponds to about 10^{12} K. In this regime, α_S is too large to rely on calculations based on perturbation theory. Hence, non-perturbative QCD calculations on a space-time lattice were developed for small baryon chemical potential $\mu_B \approx 0$. With this method, the *critical temperature* could be estimated to be $T_C \sim (154 \pm 9)$ MeV [7]. At the collision energies provided by the LHC, the baryon chemical potential is small. Hence, calculations from lattice QCD apply to describe such collisions.

2.2.1 Quark-gluon plasma in the experiment

The evolution of the system created in heavy-ion collisions is schematically illustrated in Fig. 2.3. During the initial collision of the ultra relativistic nuclei, hard parton scatterings take place. Large momentum transfers of $Q \gtrsim 10$ GeV/c allow to produce particles containing heavy quarks, i.e. c or b quarks, jets, or the heavy, colourless gauge bosons W^\pm , Z . After a time of $\tau \sim 0.2$ fm/c, with 1 fm/c corresponding to about 3×10^{-24} s, a strongly interacting partonic medium, also called *fireball*, is formed. The size and geometry of this medium depends on the overlap region of the colliding nuclei and their initial state fluctuations of the energy distribution. Pressure gradients drive the expansion of the system. The system thermalizes quickly after about $\tau \lesssim 1$ fm/c. When the system is in thermodynamic equilibrium, its dynamics can be described by hydrodynamics. This phase lasts about $\tau \sim 10 - 20$ fm/c, until the system has expanded and cooled down to the critical temperature $T_C \approx 154$ MeV [8], where the system undergoes a transition from QGP to hadron gas. When the system cools down even further, inelastic collisions cease to occur, at which point the particle composition of the system is fixed (*chemical freeze-out*). With the progressing expansion of the hadron gas, the density of the system is reduced until the hadrons do not elastically collide with each other any further (*kinetic freeze-out*). The emerging hadrons can finally be detected to gain information about the quark-gluon plasma.

2.2.2 Experimental observables

This section presents a selection of observables of the quark-gluon plasma in heavy-ion collisions, which on the one hand give complementary information on the evolution of the QGP (Sec. 2.2.1) and on the other hand determine the design requirements for a heavy-ion collider experiment (Sec. 2.3.1).

One of the key observables is the *multiplicity* of produced charged particles. It is a

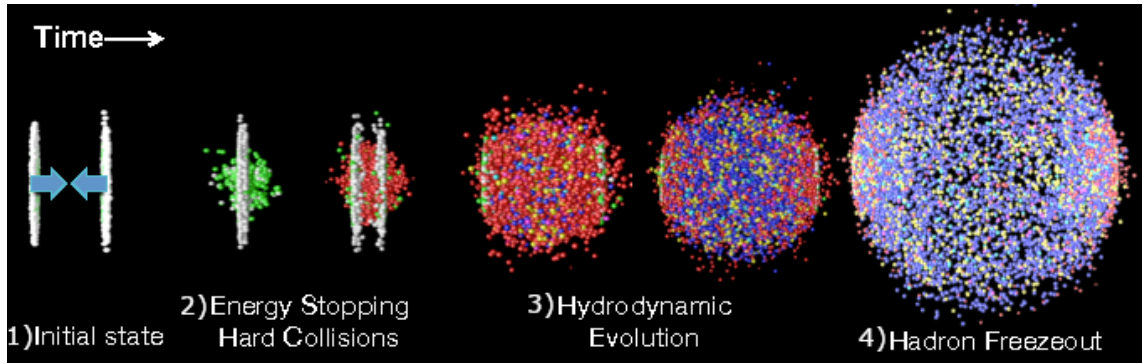


Figure 2.3: Evolution of an ultra-relativistic heavy-ion collision. 1) Two Lorentz-contracted nuclei approaching each other. 2) The two nuclei pass through each other, while hard collisions take place. The QGP starts to form. 3) The QGP reaches thermal equilibrium and expands. This results in the cooling down of the system. 4) When the expanding system reaches the critical temperature, colour-neutral hadron states are formed. Upon further expansion, inelastic hadron collisions cease to occur, fixing the particle composition (hadron freezeout) [9].

measure of the number of primary charged particles² N_{ch} produced per rapidity unit dN_{ch}/dy , where the rapidity y is a logarithmic measure of the longitudinal velocity of a particle. The charged-particle multiplicity is related to the collision energy and geometry, and it can be used to classify events. It is particularly useful to compare data between different experiments or collision systems.

By comparing the charged-particle multiplicity distributions to the purely geometrical *Glauber model* [10], which treats nuclear collisions as a superposition of binary nucleon-nucleon collisions, the measured particle multiplicity can be related to geometrical parameters such as the distance between the centers of the colliding nuclei (*impact parameter* b), the number of binary nucleon-nucleon collisions N_{coll} or the number of nucleons participating in the collision N_{part} , i.e. the number of nucleons participating in at least one binary collision. In order to do so, a Monte Carlo simulation of the Glauber model is employed. The collision process of two nuclei, composed of nucleons according to a realistic spatial distribution, is simulated on an event-by-event basis. Many nucleus-nucleus collisions are simulated where the value of the impact parameter is randomized. The resulting simulated charged-particle multiplicity depends on N_{part} and N_{coll} . A negative binomial distribution is then fitted to the charged-particle multiplicity distribution of the measured data and all simulated events [11].

The particle multiplicity distribution can then be divided into so-called *centrality classes* by sharp cuts on the particle multiplicity, which acts as a proxy to percentile intervals of the total nuclear interaction cross section (Fig. 2.4). A centrality

²A primary particle is a particle which is directly produced in the collision. Particles from interactions with the material are excluded.

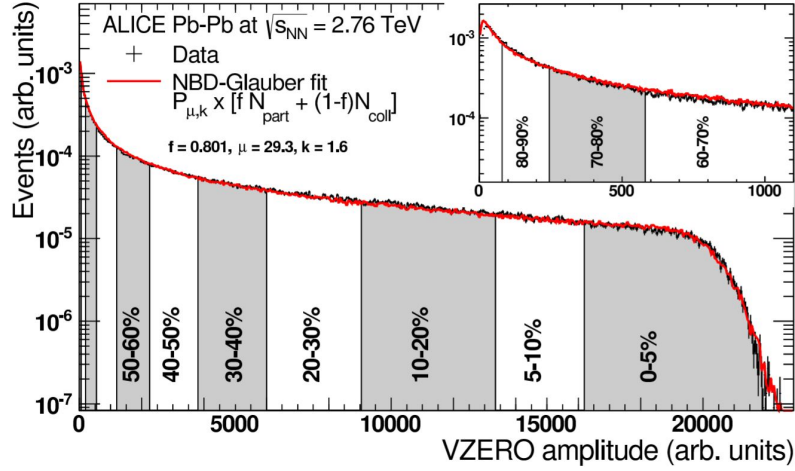


Figure 2.4: Distribution of the sum of amplitudes in the ALICE V0 detector (cf. Sec. 2.3). The distribution is fitted with a negative binomial distribution (NBD) Glauber fit (red line). Then, centrality classes can be defined as indicated in the figure [11]. A more detailed explanation can be found in the text.

class in the measured distribution corresponds to the same centrality class in the simulated distribution. Therefore, a mapping between measured quantities and those obtained from phenomenological calculations with well defined geometrical properties is established. From the Glauber model, the mean number of binary collisions $\langle N_{coll} \rangle$ and the mean number of participants $\langle N_{part} \rangle$ in a centrality class can be calculated. A head-on (central) collision of two nuclei corresponds to 0% centrality, whereas collisions with little overlap (peripheral) have large centrality. In ALICE, the centrality is mainly determined with the V0 detectors (Sec. 2.3.2).

Particles created in the hard parton scattering in the initial collision phase, also called *hard probes*, offer a unique way to examine properties of the QGP. In the initial hard scattering, particles of large (transverse) momentum and mass, the latter addressing particles containing c or b quarks, can be produced. As they are produced before the QGP is created, they experience the full evolution of the fireball. Moreover, heavy particles cannot be produced thermally in the medium, even at the highest temperatures of the QGP produced at the LHC. Therefore, hard probes from the initial scattering are also called *external probes*. When a colour-charged object traverses the Quark-Gluon Plasma, its phase-space distribution is modified through interactions in the medium.

Distributions of particles from hard parton scattering can usually be calculated with perturbative QCD methods. Thus, their propagation through the medium can provide information on the properties of the medium they traverse. Interactions with the medium result in a modification or loss of (transverse) momentum of single partons or jets (*jet quenching*). Additionally, bound states can be "melted" into their partonic constituents by the high-temperature medium. The quarks can then

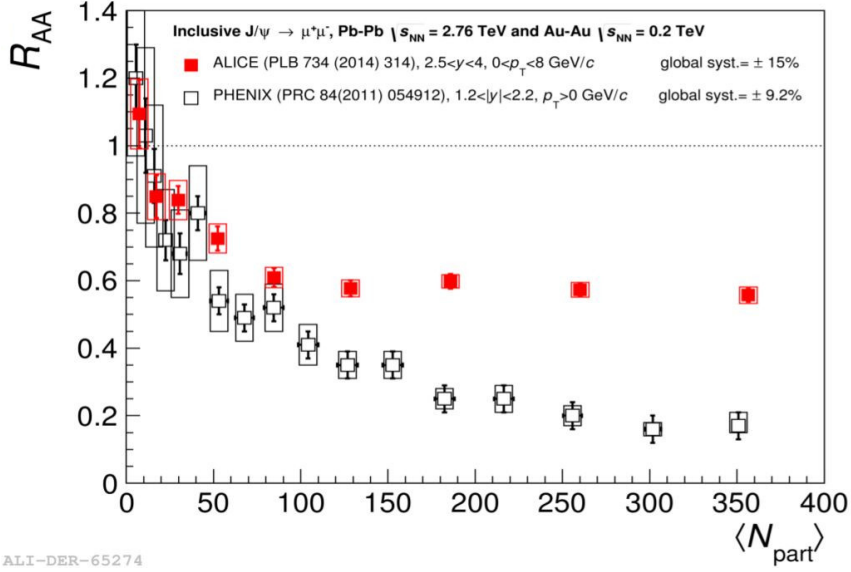


Figure 2.5: Nuclear modification factor R_{AA} of inclusive J/ψ production as a function of $\langle N_{part} \rangle$ in Pb-Pb collisions at $\sqrt{s_{NN}} = 2.76$ TeV by ALICE compared to results at PHENIX-RHIC in Au-Au collisions at $\sqrt{s_{NN}} = 200$ GeV. An enhancement of the J/ψ yield in ALICE compared to PHENIX is visible [14].

take part in the collective motion of the medium.

Quarkonia, i.e. bound states of $c\bar{c}$ or $b\bar{b}$, are predicted to show a *sequential melting* depending on the binding energy of the quarkonium state [12]. As a consequence, a decrease in the yield of quarkonia states in nucleus-nucleus (AA) collisions compared to primary-collision scaled pp collisions, where no QGP is produced, is expected. However, at increasingly higher collision energies, the total amount of produced heavy quarks rises. Statistical recombination at the phase transition of, for example, c and \bar{c} quarks, as predicted by the *statistical hadronization model* [13], can lead to an enhancement of quarkonia states, such as the J/ψ , in heavy-ion collisions. Since the combining quarks have thermal energies, most of the generated quarkonia have low p_T .

A common tool to compare the same quantity, for example particle yields, in AA collisions with pp collisions is the *nuclear modification factor* R_{AA} :

$$R_{AA} = \frac{1}{\langle N_{coll} \rangle} \frac{dN_{AA}/dp_T}{dN_{pp}/dp_T}. \quad (2.2)$$

The R_{AA} can be differently defined depending on the comparison made. In this example, the p_T -differential particle yield measured in pp and AA collisions is compared. By including the factor $1/\langle N_{coll} \rangle$, the AA collision is compared with a superposition of $\langle N_{coll} \rangle$ independent pp collisions. If the heavy-ion collision would simply be an overlap of binary collisions, the R_{AA} should be equal to 1. However, if the formed medium in AA collisions affects the examined quantity, the R_{AA} is

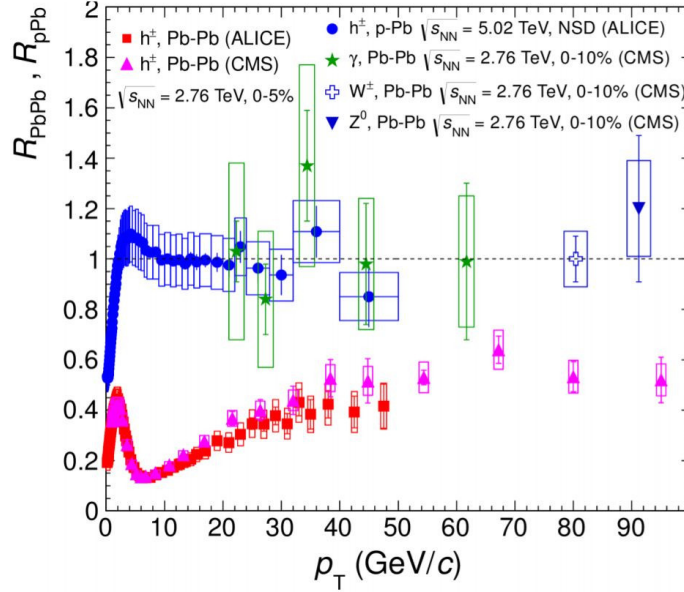


Figure 2.6: Nuclear modification factor R_{AA} for charged hadrons (h^\pm), γ , W^\pm and Z as a function of p_T in different collision systems and experiments. Particles that do not participate in the strong interaction (γ , W^\pm , Z) show an R_{AA} consistent with 1, indicating that they are not affected by the medium formed in Pb-Pb collisions [14].

modified. For example, a suppression (enhancement) of the J/ψ yield in heavy-ion collisions would result in an R_{AA} lower (higher) than 1. Indeed, a strong suppression of J/ψ was found at RHIC with $R_{AA} \approx 0.2$ for most central collisions. At the LHC, which operates at $\sqrt{s_{NN}}$ more than 10 times higher, ALICE found an $R_{AA} \approx 0.6$ in the p_T range $0 < p_T < 6$ GeV/c at similar $\langle N_{part} \rangle$ as RHIC [15]. Figure 2.5 shows a comparison of the two measurements. The difference can be attributed to the recombination mechanism discussed above.

Particles that do not carry colour charge, i.e. γ , Z and W^\pm , are not modified by the QGP and show an R_{AA} consistent with 1 (Fig. 2.6).

The bulk of the particles produced in heavy-ion collisions stems from soft collisions in the QGP. Observables focusing on the bulk properties are called *soft probes* and have low transverse momenta $p_T < 2$ GeV/c.

One observable is the collective particle motion, also known as the *flow*. In non-central collisions, the overlap region of the two nuclei is lenticularly shaped. The exact shape depends on the impact parameter (or centrality), the spatial density profile of the nucleus and initial state fluctuations. As a consequence, large pressure gradients during the initial phase of the QGP are present. During the expansion of the medium, pressure gradients are reduced by the collective motion of the QGP constituents. The initial azimuthal asymmetry of the medium is reflected in an azimuthal momentum asymmetry of the final state particles, which is described by a Fourier expansion with coefficients v_n , of which the *elliptic hydrodynamic flow* v_2

is usually the largest. The anisotropic flow is sensitive to transport properties, the initial geometry of the overlap and the equation of state of the system [16].

2.3 The ALICE experiment

ALICE is located at the LHC at CERN. For one month per year, either lead-lead collisions with energies up to $\sqrt{s_{NN}} = 5.02$ TeV or p-Pb collisions are recorded. Recently, also a short run with Xe-Xe collisions at $\sqrt{s_{NN}} = 5.44$ TeV was performed.

In order to study these collisions, the previously introduced observables have to be measured with high precision. This leads to a multifaceted set of requirements on the detectors. Since most particles created in heavy-ion collisions are soft, i.e. they have low transverse momentum $p_T < 2$ GeV/c, it is especially important to measure low-momentum particles and to keep the amount of material, that particles have to traverse, as low as possible. Furthermore, excellent particle identification is required.

In this section, ALICE and its detectors are introduced. A special focus is put on the *Time Projection Chamber* (TPC), as it is the most important apparatus for the studies presented in this thesis.

2.3.1 Design requirements

Before we can discuss the design, it is necessary to introduce the coordinate system. The origin is placed at the point of the collision, also called the *interaction point*. The longitudinal direction (z -axis) is following the beam axis, the x -axis points towards the accelerator centre following the local horizontal plane and the y -axis points upwards, perpendicular to the x -axis (Fig. 2.7). A more useful representation is obtained by considering the radial symmetry of the detector. In the transversal plane, the distance to the beam axis $r = \sqrt{x^2 + y^2}$ is used as well as the azimuthal angle ϕ in the xy -plane. The polar angle θ measures the angle in the longitudinal plane between the beam axis and the point of interest. It can be used to define the *pseudo-rapidity* η of a particle:

$$\eta = -\ln \left(\tan \frac{\theta}{2} \right) = \frac{1}{2} \ln \left(\frac{p + p_L}{p - p_L} \right). \quad (2.3)$$

Here, p is the absolute value of the three momentum vector \mathbf{p} and p_L is the longitudinal momentum in z -direction. Regions with low pseudo-rapidity ($\eta \sim 0$) are called *mid rapidity* while regions at high values ($|\eta| \gtrsim 2$) are called *forward* or *backward rapidity*.

When analysing heavy-ion collisions, it is crucial to know the geometrical parameters of the collision. As explained in Sec. 2.2.2, information on the nuclear interaction cross section or the number of colliding or participating nucleons can be retrieved by measuring the multiplicity of particles and comparing it to simulations based on the Glauber model. Alternatively, the energy of *spectator particles*, nucleons that do not participate in the collision, can be measured [11]. Dedicated detectors are needed to classify events by their multiplicity or centrality. They usually cover regions of

high η , so that correlations between measurements (at low to mid rapidity) and the centrality are avoided.

Due to the high multiplicity in heavy-ion collisions, the tracking of particle trajectories requires fine granularity in the tracking devices. To measure the momentum of charged particles as well, the tracking devices are superimposed with a magnetic field. Neutral particles are detected in calorimeters, where their energy is measured. This is especially important for precise photon energy measurements, as they are used as probes for different stages of the QGP.

In order to measure the bulk of the particles, which are produced with thermal energies, tracking at low p_T is needed. For this reason the magnetic field cannot be too large, otherwise charged low-momentum particles start to spiral before they can reach the tracking devices. Additionally, the material budget of the (innermost) tracking detectors needs to be minimized, so that the low p_T particles are not stopped before being fully characterized, while also reducing the deterioration of the momentum resolution by multiple scattering, which is dominant at low momenta.

Devices for Particle IDentification (PID) usually only operate well in relatively small momentum ranges. However, in heavy-ion experiments the measurement of hard and soft probes requires PID for momenta spanning several orders of magnitude. Therefore different technologies need to be combined to achieve reliable particle identification.

2.3.2 Detectors

The ALICE detector system consists of a broad variety of technologies to meet the requirements mentioned before. A schematic view of the ALICE detector, as it is used during the LHC Run 2, can be seen in Fig. 2.7. The whole system spans $16\text{ m} \times 16\text{ m} \times 26\text{ m}$ and weighs about 10 000 t. It consists of two parts. One is the *central barrel*, which is contained inside the L3 solenoid magnet. This room temperature magnet can provide magnetic fields of up to $B = 0.5\text{ T}$. The central barrel is mainly used to detect hadrons, electrons and photons. Located in the backward rapidity range is a muon spectrometer with a 0.6 T dipole magnet.

In the following, a short overview over the most commonly used detectors is given. For further information [1] can be consulted.

The **Inner Tracking System (ITS)** of the central barrel consists of three different types of silicon detectors with two layers for each type. Going from the beam pipe outwards, there are two layers of silicon pixel detectors (SPD), then silicon drift detectors (SDD) and finally silicon strip detectors (SSD).

To determine the primary vertex of the collision and secondary decay vertices as precisely as possible, the ITS sits close to the beam pipe while minimizing the material budget to only 7.2% of a radiation length. A resolution of about $100\text{ }\mu\text{m}$ for the primary vertex is achieved. Additionally, PID information can be obtained in momentum regions from $200\text{ MeV}/c$ to $1\text{ GeV}/c$ by measuring the energy loss of charged particles through ionization in the SDD and SSD.

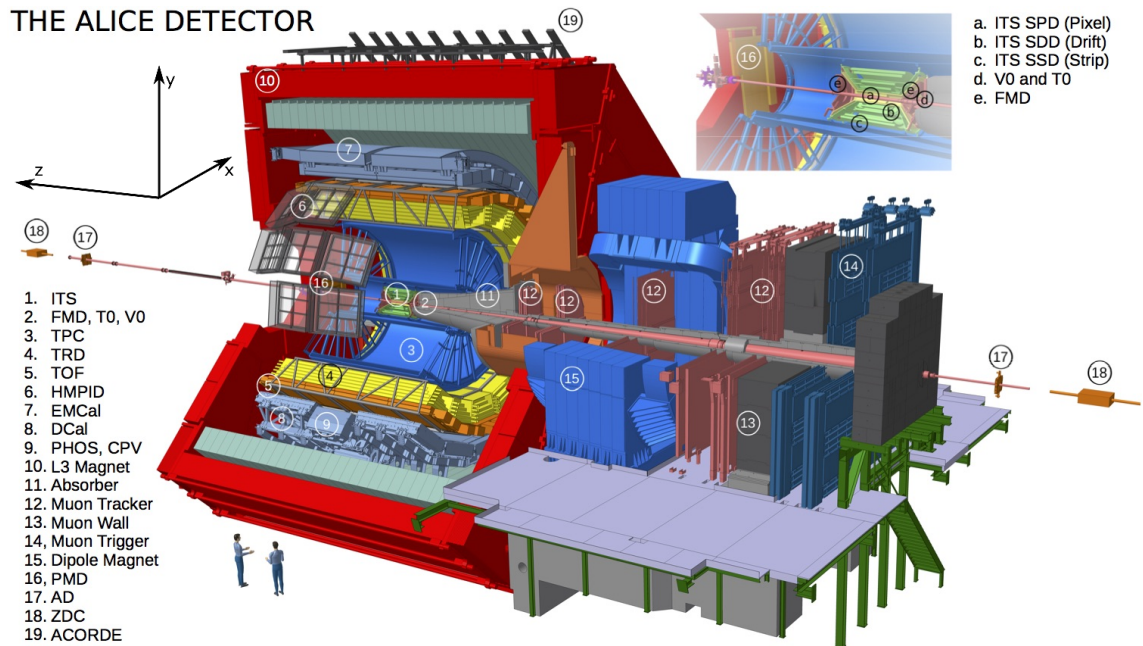


Figure 2.7: Layout of ALICE during the LHC Run 2. The coordinate system is shown in the top left corner, where the origin is chosen to be in the interaction point and the x -axis points to the middle of the collider ring in the local horizontal plane [17].

The main tracking detector, the **Time Projection Chamber (TPC)**, surrounds the ITS. It is a gas tracking detector with *Multi-Wire Proportional Chamber (MWPC)* readout that combines 2D position and drift time measurements to reconstruct 3D space-point information. By measuring the charge deposit from ionising particles passing the volume and combining it with the momentum information, excellent particle identification capabilities are obtained. A more detailed description of the TPC can be found in chapter 2.4.1.

At momenta above a few GeV/c, the TPC cannot discriminate between electrons and pions anymore. Complementary PID information is provided by the **Transition Radiation Detector (TRD)**. Six layers of 48 mm thick radiator induce transition radiation for traversing electrons with $p > 1 \text{ GeV}/c$. The photons convert in the following 30 mm long drift region, which is filled with a Xe-CO₂ (85-15) gas mixture. Since this effect only occurs for particles with Lorentz factor $\gamma = 1/\sqrt{1 - (v/c)^2}$ greater than 1000, only the light electrons are subject to it, while pions do not induce transition radiation. Moreover, the tracking capabilities of the TRD combined with the ITS allow to correct space-point distortions in the TPC.

The **Time Of Flight detector (TOF)** utilizes *Multi-gap Resistive-Plate Chambers (MRPC)* to measure the arrival time of a particle in the detector with a resolution of 50 ns. Comparing this to the time of the collision, measured by the **T0** detector,

PID can be provided for particles with momenta of a few GeV/c.

The **High-Momentum Particle Identification Detector (HMPID)** provides additional PID for particles with momenta $p_T > 1$ GeV/c. It uses *Ring Imaging Cherenkov detectors* (RICH) to cover the high momentum range, where exploiting energy loss through ionization becomes less reliant. However, it does not cover the full azimuthal angle.

ALICE has different types of calorimeters. The **ElectroMagnetic Calorimeter (EMCal)** is a lead-scintillator sampling calorimeter that is used to measure the energy of electrons with high transverse momentum, to detect photons and to study jet physics. Together with the **Di-jet Calorimeter (DCal)**, a two-arm electromagnetic calorimeter is formed, which allows to measure back-to-back jet correlations.

The **PHOTon Spectrometer (PHOS)** is a highly segmented lead-tungstate crystal calorimeter. It is designed to detect and measure photons. A small Ar-CO₂ (80-20) drift volume on the side facing the beam pipe suffices as charged-particle veto. The PHOS provides additional PID of photons against charged hadrons and (anti-)neutrons. Both PHOS and EMCal do not cover the full azimuthal angle.

Located at a distance of 116 m in forward and backward rapidity is the **Zero Degree Calorimeter (ZDC)**. During nucleon-nucleon collisions, only a fraction of all nucleons collide. Nucleons outside of the overlap region (spectator nucleons) continue to travel along the beampipe. Knowing the amount of spectators in a collision allows to classify events by centrality. The ZDC is able to quantify the amount of spectators.

Further characterisation of events is achieved with the multiplicity detectors **V0**, the **Forward Multiplicity Detector (FMD)** and the **Photon Multiplicity Detector (PMD)**. They cover different regions at high pseudo-rapidity ($1.7 < \eta < 5.1$). In addition to measuring the particle multiplicity, the V0 is also used to trigger events.

The **muon spectrometer** detects muons at backward rapidity. An absorber in the central barrel for hadrons, electrons and photons ensures that only muons reach the detectors. Outside of the central barrel, a 0.6 T strong dipole magnet is placed to improve the momentum measurement of muons. The muon tracker consists of a series of tracking plates inside of the L3 solenoid, in the dipole magnet and behind it. Two trigger stations employing resistive plate chambers follow after a 1.2 m thick iron wall. They can provide triggers for muons in the momentum range from about 0.5 GeV/c to 2 GeV/c.

2.4 The ALICE time projection chamber

The main tracking device of ALICE is the Time Projection Chamber (TPC). It is a gaseous ionization detector that is capable of three-dimensional track reconstruction.

By measuring the energy loss of charged particles which traverse the chamber, the TPC is able to distinguish between different particle species with p_T up to the GeV/c scale.

The ALICE TPC is a gas filled cylinder of 5 m length, an inner radius of 85 cm and an outer radius of 2.5 m. With an active volume of almost 90 m³, it is the largest TPC in the world. Its capabilities to record up to 20 000 tracks per event combined with its excellent particle identification make it a great tool for studying heavy-ion collisions.

In this section, the TPC's design, its working principle and its performance during the LHC Run 2 are presented.

2.4.1 Design

The TPC of ALICE (Fig. 2.8) is a 5 m long cylinder that is divided in the middle by a 22 μm thick *central electrode* made of an aluminised mylar foil. Each drift volume is closed off by an endplate with 18 trapezoidal segments. Due to the large dimensions of the TPC, each segment is again divided into two sectors, holding an *inner readout chamber* (IROC) and an *outer readout chamber* (OROC). The readout chambers are equipped with an amplification stage for electrons from ionization and a pad plane. Until the end of LHC Run 2 (December 2018), Multi-Wire Proportional Chambers (MWPC, Sec. 2.4.3) were employed to amplify the electrons. The created signal is then detected by the pad plane, which consists of 159 rows of pads along the r -axis. The ALICE TPC was operated with a Ne-CO₂-N₂ (90-10-5)³ gas mixture in Run 1 and was then changed to Ar-CO₂ (90-10) for most of Run 2.

A potential of 100 kV is applied to the central electrode. To achieve a homogeneous electrical field from the electrode to the readout chambers, so-called *inner* and *outer field cages* at a radius of 85 cm and 2.5 m, respectively, are employed. They consist of many equally spaced strips which guide the decreasing potential towards the readout plane. In this way, a homogeneous electric field of $E_{Drift} = 400 \text{ kV cm}^{-1}$ (anti-)parallel to the z -axis is created. Additionally, the L3 magnet provides a homogeneous magnetic field of up to 0.5 T that is, in first order, aligned with the electrical field. Corrections for inhomogeneities of the magnetic or electric fields are applied. A detailed description of the detector can be found in [18].

2.4.2 Working principle

A time projection chamber is a type of drift chamber that is capable of reconstructing three dimensional space-points. Through measurements of the momentum and the

³Originally, a Ne-CO₂ (90-10) mixture was used. However, it was found that adding five parts of nitrogen increases the stability of the operation against discharges. Therefore, the notation Ne-CO₂-N₂ (90-10-5) was introduced, showing not percentages, but parts. In percentages, the mixture is Ne-CO₂-N₂ (85.7-9.5-4.8). However, the historical notation will be adopted in this thesis.

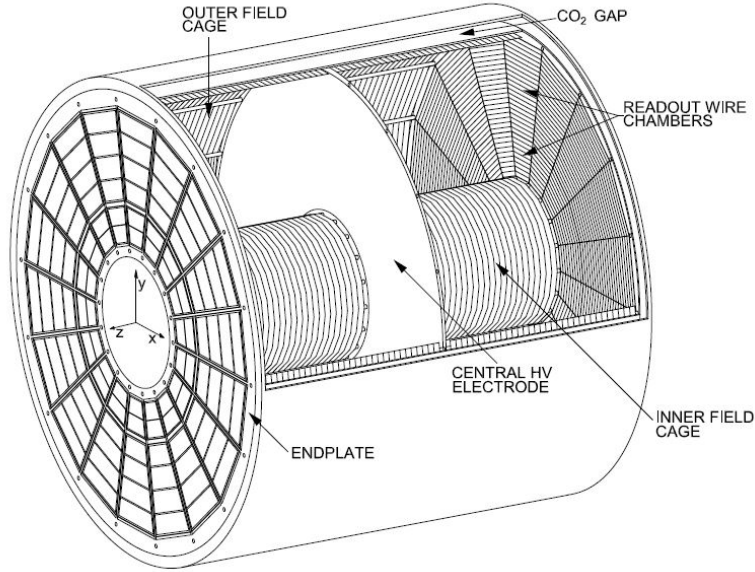


Figure 2.8: Sketch of the ALICE TPC [18].

energy deposited by traversing charged particles, it is possible to identify the particle species. In this section the working principle is described considering a single particle passing through the detector.

When a charged particle traverses the gas volume of the TPC, it loses energy through random collisions with the gas molecules. Electrons are liberated from their atoms or ions, creating electron-ion pairs along the track of the charged particle. The average energy loss through ionisation is described by the *Bethe-Bloch formula* (see also Eq. 2.7). The liberation of electrons by the traversing particle is called *primary ionisation*. Some of the electrons carry enough energy to further ionise nearby atoms. This so-called *secondary ionisation* creates clusters of electrons around the locations of primary ionisation. Typical energies deposited per electron-ion pair are ~ 30 MeV [19]. Nevertheless, the energy loss distribution shows a pronounced tail towards higher energies, especially due to highly-energetic electrons, the so-called δ -electrons, which create further electron clusters far away from the point of primary ionisation. Since particles at the LHC are produced at energies significantly higher than the average energy loss through ionisation, the charged particle continues on its path almost undisturbed.

The applied electrical field causes the ions to drift to the central electrode, whereas the electrons drift towards the readout plane. In a homogeneous electrical field, as given in the ALICE TPC, the drift velocity w of the electron can be described as

$$w = \frac{e}{2m} E \tau, \quad (2.4)$$

where e and m is the charge and the mass of the electron, respectively [20]. The average time between two collisions of an electron with a gas molecule is indicated by

τ and depends on the gas mixture, the electric field strength E , and environmental parameters such as temperature and gas pressure. Small changes or non-uniformities of these parameters can lead to fluctuations of the drift velocity. Therefore, these parameters need to be well controlled. In addition to regular monitoring of the relevant (environmental) parameters, a laser system is used to calibrate the electron drift velocity. An ultra-violet laser is guided into the TPC, where it is split and produces many tracks at well-defined positions in the chamber's volume. The arrival time of the electrons liberated by the laser define the drift velocity. This laser calibration is applied regularly during data taking. As a result, the electron drift velocity can be accurately measured throughout the whole operation time. The maximum drift time of an electron in the ALICE TPC is of the order of 90 μs , corresponding to a full drift length from the central electrode to the readout chambers.

Since the charge created by ionisation is many times smaller than the electrical noise of the readout electronics, the electrons have to be amplified to produce a measurable signal. This is realised with MWPCs and will be explained in more detail in section 2.4.3. The position of the deposited charge on the pad plane gives direct information about the xy -coordinates, while the z -coordinate can be calculated by measuring the arrival time (relative to the time of the collision) of the electrons, and multiplying it with the drift velocity.

In heavy-ion collisions, many thousands of charged particles pass through the active gas volume of the TPC, each leaving a track of ionisation clusters. The three dimensional reconstruction of these space-points with high granularity makes it possible to reconstruct the tracks with the help of a highly sophisticated algorithm. An example for such a track reconstruction of a single event can be seen in Fig. 2.9.

Once the particle tracks are reconstructed, the momentum of the respective particle can be derived from the curvature radius r_p with the relations

$$p_T[\text{GeV}/c] \approx 0.3 \cdot q[e] \cdot B[\text{T}] \cdot r_p[\text{m}] \quad (2.5)$$

$$p = \frac{p_T}{\sin(\theta)}. \quad (2.6)$$

Here, the electrical charge q is given in units of electron charge e and θ is the inclination angle of the track with respect to the beam pipe.

In addition to measuring the position of ionisation clusters, the TPC also counts the charge which is deposited along a track. This makes it possible to quantify the specific energy loss per path length dE/dx of a particle. Theoretically, combining the energy loss with the momentum of the particle, one can determine the particle species by exploiting the *Bethe-Bloch* formula [5]

$$-\left\langle \frac{dE}{dx} \right\rangle = Kz^2 \frac{Z}{A} \frac{1}{\beta} \left[\frac{1}{2} \ln \left(\frac{2m_e c^2 \beta^2 \gamma^2 T_{max}}{I^2} \right) - \beta^2 - \frac{\delta(\beta\gamma)}{2} \right]. \quad (2.7)$$

It describes the mean energy loss dE for heavy particles with mass $M \gg m_e$ through ionisation per path length dx in the absorber material, i.e. the counting gas of the

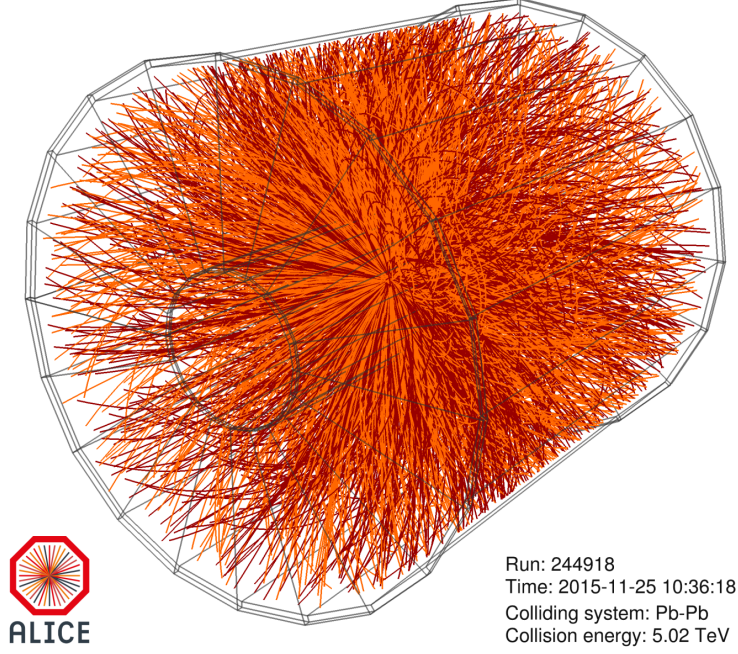


Figure 2.9: Event display of a lead-lead collision at $\sqrt{s_{NN}} = 5.02$ TeV [21].

TPC. The other variables in Eq. 2.7 are the following:

K = Constant factor;

z = Charge of the incident particle q : $z = \frac{q}{e}$;

Z = Atomic number of the absorber;

A = Atomic mass of the absorber;

$\beta = v/c$;

m_e = Electron mass;

γ = Lorentz factor $1/\sqrt{1 - \beta^2}$;

T_{max} = Maximum kinetic energy transfer;

I = Mean excitation energy;

$\delta(\beta\gamma)$ = Density effect correction;

The equation is only valid in an intermediate momentum range of $0.1 \lesssim \beta\gamma \lesssim 500$, where

$$\beta\gamma = \frac{p}{mc}. \quad (2.8)$$

Since the Bethe-Bloch equation is dependent on the mass of the ionising particle, the identity of a particle can be determined. However, due to the long tail of the ionisation towards higher deposited energies, the average energy loss does not perform

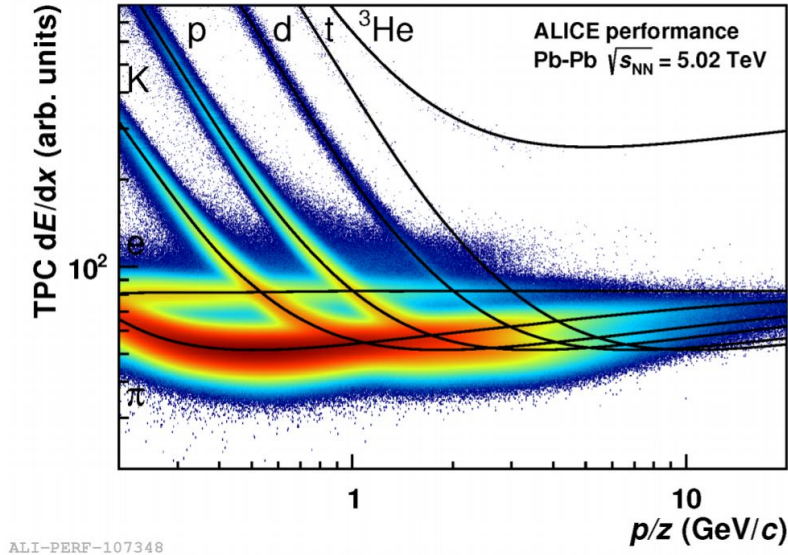


Figure 2.10: TPC signal of the specific energy loss dE/dx as a function of particle momentum p normalized by its charge number z in Pb-Pb collisions at $\sqrt{s_{NN}} = 5.02$ TeV. Black lines depict the parametrization of the specific energy loss according to Eq. 2.9 for different particle species [23].

well as an estimator for the mass hypothesis. Thus, the method of *truncated mean* is used. Along a particle's track, a maximum of 159 charge measurements—one per pad row—can be obtained. Only the lowest 60% of the energy loss per unit path length are used to form a (truncated) mean value [22], which is also called *TPC signal*. The experimental data is parametrized as

$$f(\beta\gamma) = \frac{P_1}{\beta^{P_4}} \left(P_2 - \beta^{P_4} - \ln\left(P_3 + \frac{1}{(\beta\gamma)^{P_5}}\right) \right), \quad (2.9)$$

where P_i , $i \in \{1, 2, 3, 4, 5\}$ are fit parameters [18]. The resulting curves are also known as *splines*. This function is an adaptation of the Bethe-Bloch equation, which was first proposed by the ALEPH collaboration [20].

Figure 2.10 shows the TPC signal for different tracks as a function of their momentum. As the curve is shifted for each particle species, a hypothesis about the particle species can be made depending on its relative position to the splines. In regions where two or more curves overlap, additional information from other PID detectors, for example the TOF or TRD, is necessary to resolve ambiguities.

2.4.3 Operation with MWPC

A Multi-Wire Proportional Chamber (MWPC) is a gaseous detector sensitive to charged particles. Through amplification of ionization electrons, the position and deposited energy of the traversing charged particle can be measured.

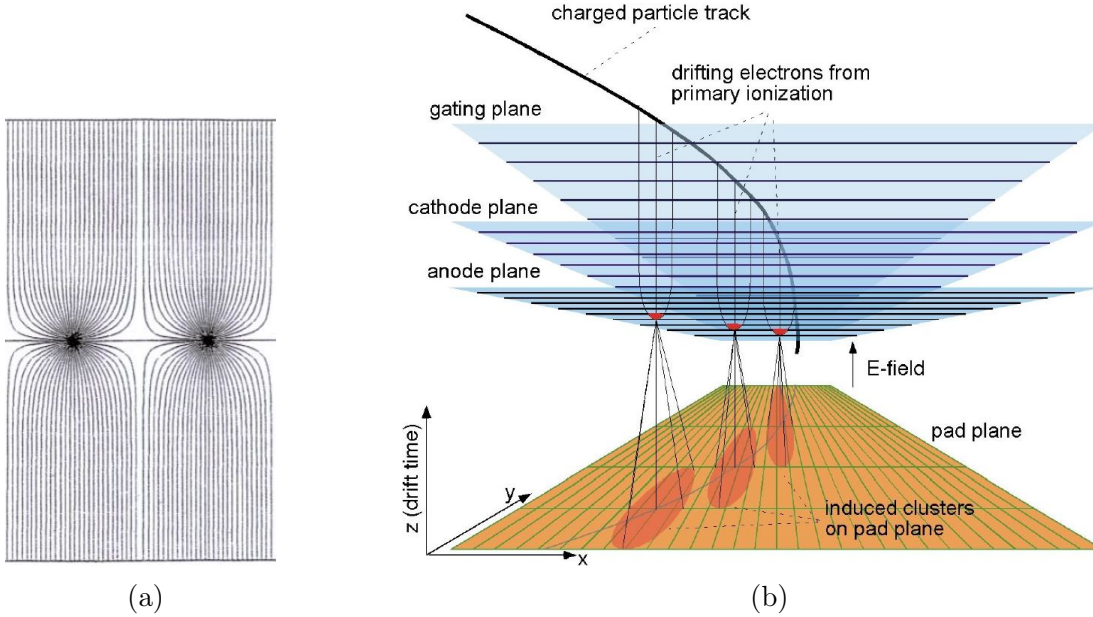


Figure 2.11: (a) Electrical field lines of a MWPC, where every wire is on the same potential. A strong radial field is present in the vicinity of the wires, while the field is homogeneous close to the cathodes. (b) Sketch of the signal creation in the ALICE TPC. The electron clusters produced by the traversing charged particle drift towards the pad plane and are amplified at the anode plane. Ions from the multiplication (indicated in red) slowly drift towards the cathode plane. They induce a mirror charge in the pad plane which is shown as red circles. By taking the center-of-mass of the induced charge, a resolution much smaller than the pad size is achieved. The z -coordinate is calculated from the drift time [24].

Multi-wire proportional chambers consist of a plane of thin wires between two electrodes. Each wire is supplied with the same high potential. This creates a strong, radial electrical field close to the wires (Fig. 2.11a). Electrons, which are liberated from the gas through ionization of the traversing charged particle, will be accelerated towards the closest wire and gain energy. Eventually they have enough energy to further ionize gas molecules. The generated electrons are also accelerated and start an *avalanche process*. The electrons are quickly collected by the anode wires while the remaining ions, slower by a factor of ~ 1000 (cf. Eq. 2.4), drift towards the nearest cathode.

The layout of the ALICE MWPC can be seen in Fig. 2.12. An additional cathode wire grid close to the anode wires separates the multiplication region from the drift volume and allows to quickly collect back-drifting ions.

Figure 2.11b shows the signal creation in the ALICE TPC. The anode wires in the TPC readout have a diameter of $20\ \mu\text{m}$. Pad sizes are optimized to the particle track

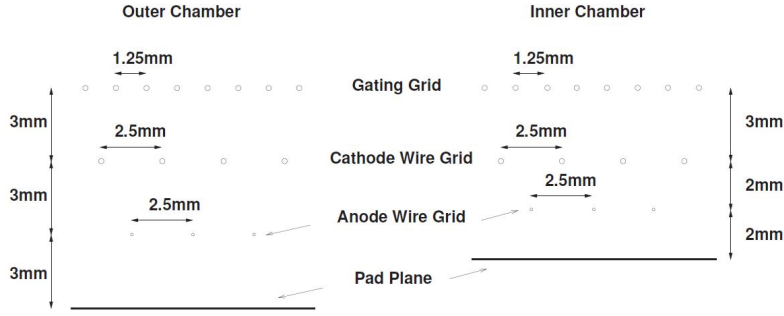


Figure 2.12: Wire geometry of the outer (left) and inner (right) readout chambers of the ALICE TPC [18].

densities at different radii, leading to $4 \times 7.5 \text{ mm}^2$ pads in the IROC, and $6 \times 10 \text{ mm}^2$ and $6 \times 15 \text{ mm}^2$ in the OROC. Electrons that enter the amplification region are multiplied by a factor, the so-called *gain*, of about 2×10^4 . The produced ions drift to the cathode wires and induce a mirror charge in the pad plane. The geometry of the wire and pad plane is chosen so that the induced signal spreads over several pads. By taking the center-of-gravity of the induced charges, a space-point resolution much better than the pad sizes can be achieved.

Apart from the readout geometry, the space-point resolution is also affected by the drift length, track inclination angle and the deposited charge on the anode wire [25]. Including these effects, a space-point resolution of 0.2 mm to 2 mm in $r\phi$ and z direction can be achieved in ALICE [18]. The transverse momentum resolution of the TPC, when combined with information about the vertex or with the ITS tracks, is of the order of 1% [22]. Figure 2.13 shows the inverse- p_T resolution, which is related to the relative transverse momentum resolution via

$$\frac{\sigma_{p_T}}{p_T} = p_T \cdot \sigma_{1/p_T}, \quad (2.10)$$

in p-Pb collisions.

In order to stop ions from the multiplication area to enter the drift region, where they would cause immense electrical field distortions, the readout chambers use a *gating grid*. Its working mechanism is displayed in Fig. 2.14. When an event is triggered for recording, the wires of the gating grid are switched to the same potential, allowing electrons to enter the amplification region. Without a trigger, they are biased with a bipolar voltage $V_G \pm \Delta V$. This prevents electrons from entering. While the gate is closed, the ions from the multiplication drift to the cathode wires and are collected there. Since no new electrons can enter, the space charge is removed in one ion drift time from the anode to the cathode wires. As a result, distortions of the electric field in the TPC by back drifting ions are avoided.

However, this method has a caveat. After the trigger signal, the gate has to stay open for $100 \mu\text{s}$ to collect all electrons from the drift volume. Afterwards the gate needs to be closed for another $180 \mu\text{s}$ in order to collect the slowly drifting ions from

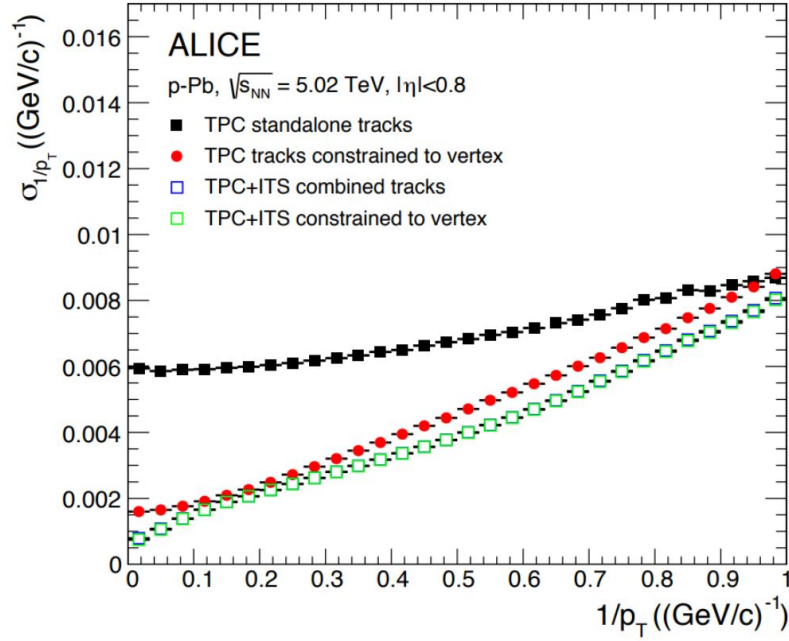


Figure 2.13: The inverse- p_T resolution of the ALICE TPC with and without track matching with the ITS or to the vertex. The relation to the relative p_T resolution is given in Eq. 2.10. [22].

the amplification region. This adds up to a readout time of almost $300 \mu\text{s}$ for a single event. Therefore, the TPC is limited to a maximum operation rate of ~ 3.5 kHz. In the specific case of central heavy-ion collisions, the data read-out rate during Run 1 was limited to only ~ 300 Hz [1]. After an upgrade of the electronics in LHC long shutdown 1, this rate was doubled [27]. The limited readout rate has resulted in an upgrade of the ALICE TPC that will be discussed in the next chapter.

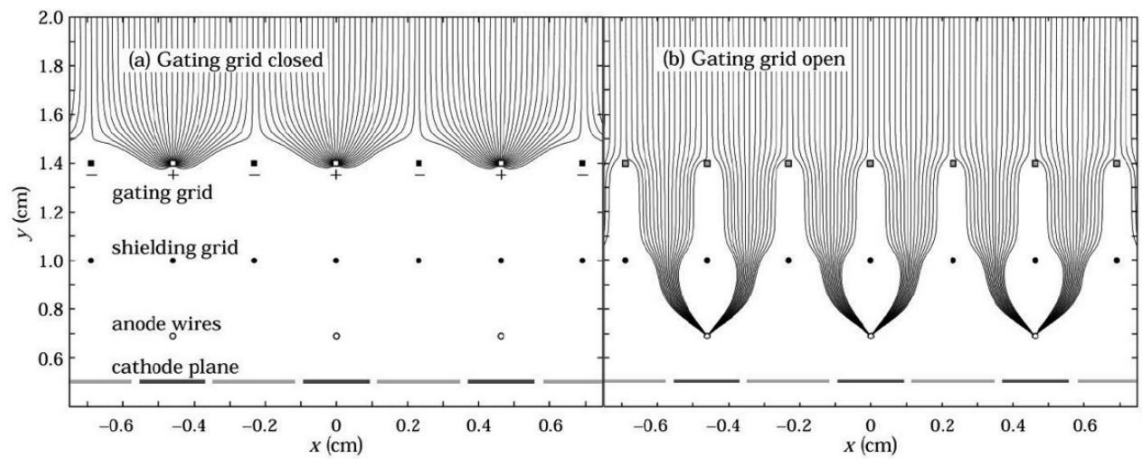


Figure 2.14: Working mechanism of a gating grid for MWPC readout [26]. The axis and distances do not correspond to the ones used in the ALICE TPC. **(left)** MWPC readout with closed gating grid. An alternating potential $V_G \pm \Delta V$ is applied to the wires of the gating grid to stop new electrons from entering the amplification region and to block ions, which are created close to the anode wires, from entering the drift volume. **(right)** All wires of the gating grid are on the same potential, allowing electrons to enter the multiplication region.

3 ALICE TPC upgrade

In December 2018, the LHC stopped its operation and the Long Shutdown 2 (LS2) started. During the following two years, the accelerator chain is upgraded to reach maximum collision energies and to provide higher rates of heavy-ion collisions. The maximum interaction rate of lead-lead collisions will increase to 50 kHz. As already described in section 2.4.3, the main tracking device of ALICE, the TPC, is limited to a maximum readout rate of about 3.5 kHz. In order to fully profit from the increased collision rate, the ALICE TPC readout will be replaced with a continuous readout employing *Gas Electron Multipliers* (GEMs).

After a short motivation for the upgrade, the GEM technology is introduced in Sec. 3.2 and the application for the future ALICE TPC is presented in Sec. 3.3.

3.1 Motivation

During Run 1 and Run 2 of the LHC, an integrated luminosity of $\mathcal{L}_{int} = 0.16 \text{ nb}^{-1}$ and $\mathcal{L}_{int} = 0.9 \text{ nb}^{-1}$, respectively, in heavy-ion collisions was reached. These numbers include minimum-bias triggers, which require at least one charged particle to be detected, as well as rare triggers. If the ALICE experiment is able to exploit the full lead-lead collision rate of 50 kHz in Run 3 and Run 4, $\mathcal{L}_{int} = 10 \text{ nb}^{-1}$ in minimum-bias events can be recorded, which corresponds to an increase of a factor of 100 in minimum-bias events. This gives rise to a substantial enhancement of sensitivity to rare probes or measurements with a low signal-to-background ratio, which is typically the case at low p_T . An overview of observables in heavy-ion collisions can be found in section 2.2.2. Figure 3.1 gives an example of the significant improvements that can be achieved with the increase of statistics and the upgraded detectors. The inclusive e^+e^- invariant low-mass spectrum of a typical month of heavy-ion data taking at $\mathcal{L}_{int} \sim 3 \text{ nb}^{-1}$ is simulated for the detector of LHC Run 2 (left) and for the upgraded version with continuous readout (right). With an increase of about two orders of magnitude in statistics and the improved tracking detectors, a much clearer spectrum can be obtained.

In order to fully exploit the increased rate of lead-lead collisions in Run 3, the current MWPCs have to be replaced. Simply opening the gating grid continuously would lead to a vast amount of ions drifting from the multiplication region back into the TPC drift volume, causing immense electric field distortions. The resulting space-point distortions cannot be corrected with sufficient resolution. To overcome this obstacle, the MWPC will be replaced with a GEM based readout. It will provide a similar performance as the MWPC while having intrinsic ion backflow blocking capabilities that allow a continuous readout.

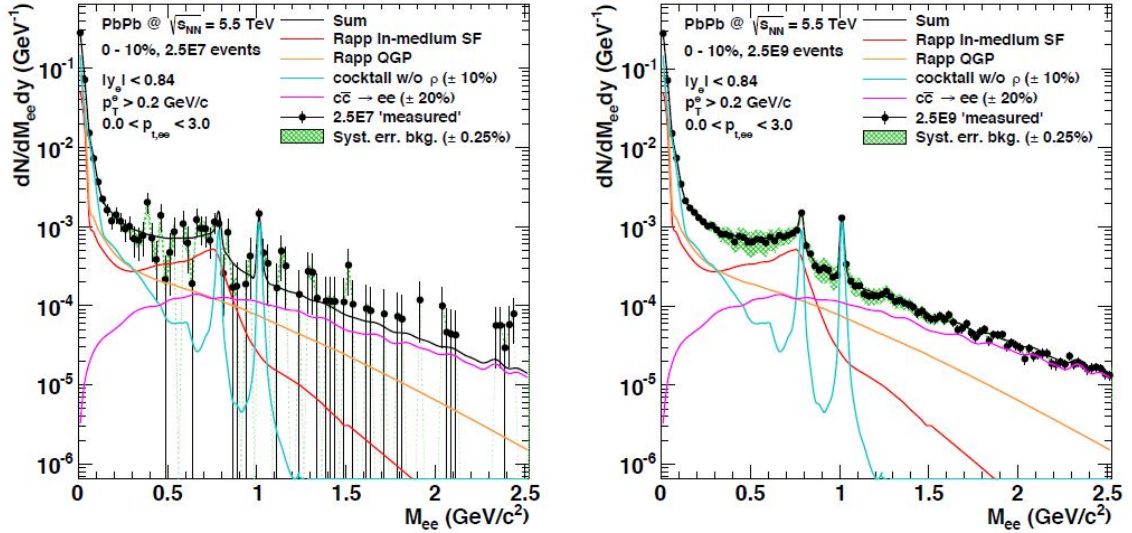


Figure 3.1: Comparison of the simulated inclusive e^+e^- invariant mass spectrum at $\sqrt{s_{NN}} = 5.5$ TeV for 0-10% most central Pb-Pb collisions. The left panel uses the detector design of Run 2 and 2.5×10^7 events, whereas the right panel uses the conditions of Run 3 with 2.5×10^9 events. The improvement of the spectrum can be attributed to the larger statistics, as well as an improvement of the upgraded detectors. Coloured lines show the contributions of different spectra: thermal radiation from hadron gas (red) and QGP (orange), light hadron decays (blue), charm decays (magenta) [28].

3.2 Gas Electron Multipliers

The Gas Electron Multiplier (GEM), invented by Fabio Sauli in 1997 [29], is a device used for charge amplification in gaseous ionization detectors and that belongs to the group of *Micro-Pattern Gaseous Detectors* (MPGD). It is a thin polyimide foil that is coated with a fine metal layer on both sides, the so-called GEM top and bottom electrodes, and is perforated with a regular hole pattern. By applying a high potential difference to the electrodes, a strong electric field is created inside the holes, which initiates avalanche multiplication when an electron passes through a hole. GEMs possess intrinsic ion backflow blocking capabilities, which makes them valuable in high-energy physics experiments.

The standard design uses a 50 μm thick Kapton foil [30] and a 5 μm layer of copper on each side. A hexagonal pattern of double-conical holes is used. The distance between a hole and its nearest neighbour, called the *pitch*, is 140 μm . The outer and inner radius of the hole is ~ 70 μm and ~ 50 μm , respectively. An electron microscope picture of a standard GEM foil is shown in Fig. 3.2.

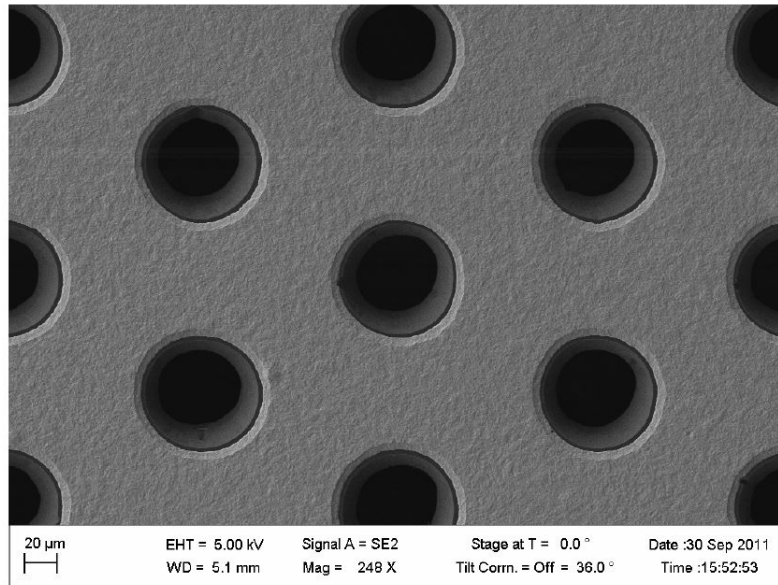


Figure 3.2: Electron microscope photograph of a standard GEM foil with a pitch of $140\ \mu\text{m}$, an outer hole radius of $70\ \mu\text{m}$ and an inner hole radius of $50\ \mu\text{m}$ [28].

3.2.1 Production

The GEM holes are created using different etching techniques for the Kapton and copper layers. The production process is sketched in Fig. 3.3.

In the standard *double-mask technique* [31], a photosensitive resin is applied to both sides of the metal. Through masks on both sides of the foil, ultra-violet light transfers the hole pattern to the coating. An alignment precision of the two masks of $\sim 10\ \mu\text{m}$ is required. The copper is then chemically removed following the masks pattern. The now perforated metal layer acts as a mask for the polyimide etching: By immersing the foil in a solvent, chemicals etch through the Kapton, creating a double-conical hole. Unfortunately, mechanical limitations only allow to produce foils of a size up to $40 \times 40\ \text{cm}^2$ with this method. To overcome this limitation, the *single-mask* technique has been developed [32]. Following the masking and etching described before, the foil is etched only from one side. A second metal etching is then applied through the holes in the polyimide, while the already etched top layer is protected. Through the holes on the bottom side, another polyimide etching creates the double-conical shape. Constraints on the availability of base material as well as the required machinery limits the width per foil to $60\ \text{cm}$ [28].

3.2.2 Working principle

Applying a voltage difference ΔU_{GEM} between the metal layers of the GEM results in a strong electric field in the GEM hole. Figure 3.4 shows the electric field lines in

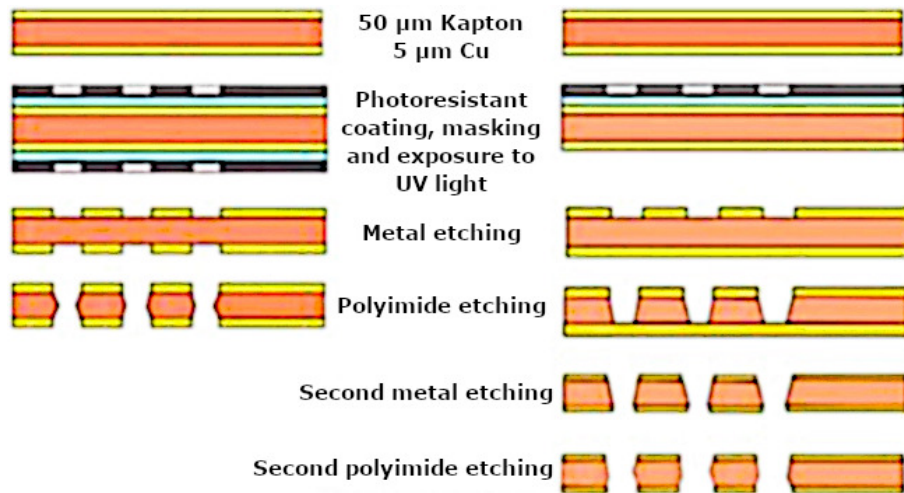


Figure 3.3: Double- (left) and single-mask (right) technique for GEM manufacturing. The figure has been adapted from [31].

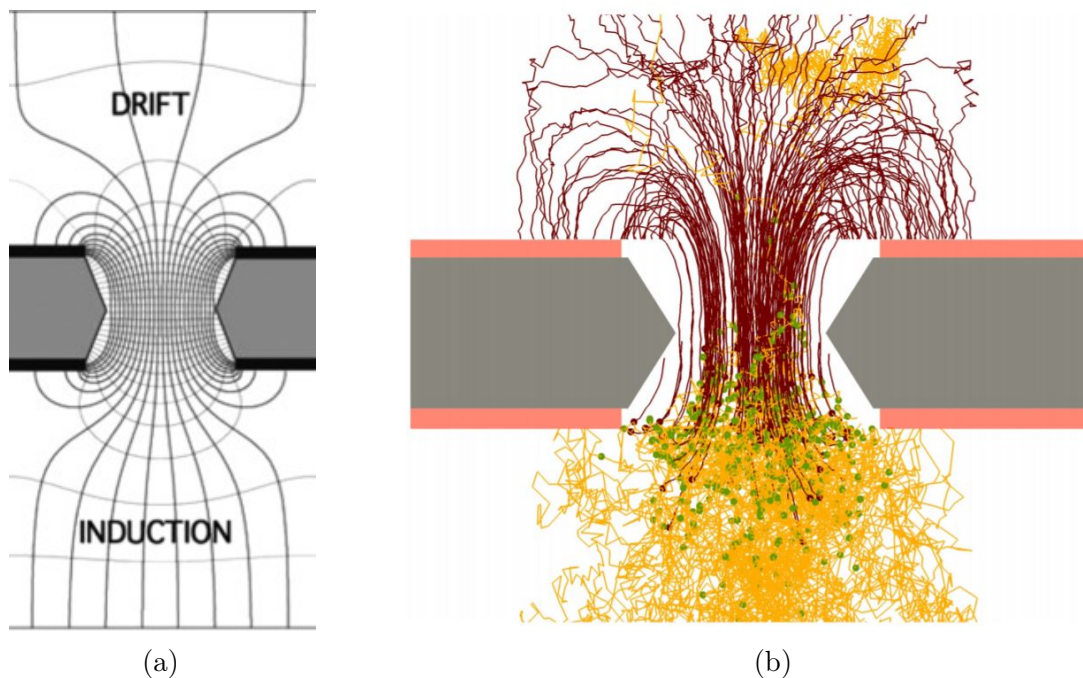


Figure 3.4: (a) Sketch of the electric field lines of a GEM between a cathode (top) and anode (bottom). The drift field is weaker than the induction field. This creates an asymmetrical field where more field lines end on the top of the GEM [31]. (b) Simulation of two electrons entering a GEM hole. Yellow lines show electron paths, dark red lines show ion paths and dots depict points of ionization [33]. Due to the higher mass of the ions, they follow the field lines closely, while electrons diffuse more strongly. If an asymmetric field is applied, many ions are trapped on the top side of the GEM, whereas most electrons exit the hole.

a double-conical GEM hole as well as a simulation of charge movement in a hole. Due to the small dimensions and the shape of the hole, a ΔU_{GEM} of only 300 – 400 V creates fields of the order of 50 kV cm^{-1} [33]. In the simulation shown in Fig 3.4b, a drift and induction field of 250 V cm^{-1} and 3.75 kV cm^{-1} , respectively, is applied, with $\Delta U_{GEM} \sim 350 \text{ V}$. The field in the GEM hole is strong enough to start avalanche multiplication processes, where most of the electrons and ions are created near the bottom of the GEM. The electrons from the amplification are directly used for the signal creation in the readout anode, which is usually below the GEM.

Figure 3.4 shows that some electric field lines end up on the top and bottom side of the GEM. This has two consequences: first, electrons might not enter the hole or might not be extracted from the GEM, but end up on the bottom electrode instead. Consequently, the effective gas gain

$$G_{eff} = \epsilon_{coll} \times G \times \epsilon_{extr} \quad (3.1)$$

is reduced, with ϵ_{coll} (ϵ_{extr}) being the collection (extraction) efficiency and G being the absolute gas gain of the GEM. The efficiencies are governed by the ratio between the respective fields above (ϵ_{coll}) or below (ϵ_{extr}) the GEM and the field in the GEM hole [34]. Second, ions from the avalanche drift back into the GEM hole and are then either guided towards the GEM top side or exit the hole. Since ions are much heavier, and therefore slower, than electrons, they follow the field lines more closely. As the created ions are distributed over the full width of the hole, the extraction efficiency depends on the fraction of field lines that do not end up on the top electrode. By applying asymmetrical fields above and below the GEM, the amount of extracted ions can be regulated. The total amount of ions drifting back towards the cathode is defined as the *ion backflow*

$$IBF = \frac{1 + \varepsilon}{G_{eff}}, \quad (3.2)$$

where ε is the number of ions extracted from the GEM per incoming electron. The intrinsic ion backflow of a single GEM is similar to the ratio of the field above and below the GEM [31]. Thus, a lower drift field results in lower IBF. However, this also implies that there is always a finite amount of ions being extracted from the GEM. The intrinsic ion blocking is highly desirable, especially in a TPC, as it allows the reduction of space-charge distortions in the drift volume.

Usually, a stack of several GEM foils is used for amplification purposes. This way, a significantly lower ion backflow can be achieved than a single GEM can, while simultaneously increasing the stability of the detector. In a stack, each foil can be operated at lower ΔU_{GEM} than with a single foil while achieving the same overall gain. The decreased gain per foil, as well as diffusion of electrons in the gaps, result in a lower charge density in each hole, which significantly reduces the probability of discharges in GEMs. A detailed discussion of discharges in GEMs is presented in chapter 4. Parameters such as gain, electron collection efficiency, ion backflow, and the stability against discharges depend on the GEM voltages and the electrical field

strengths in the gaps. Thus, a variety of requirements can be met by a GEM stack. In the following section, the specific application of a GEM stack as amplification stage in the future ALICE TPC is presented.

3.3 Design and performance

The goal of the ALICE TPC upgrade is to replace the rate-limited MWPC readout with a continuous GEM readout, while preserving the performance of the old MWPCs. A large research and development program was necessary to design readout chambers that fulfil the requirements. In order to change to a continuous readout, two major components of the TPC have to be replaced: the readout chambers (ROCs) and the electronics. Most other parts, such as the field cages, the central electrode and the support structures (cf. Sec 2.4), are re-used for the upgrade. The 36 new inner (IROC) and outer readout chambers (OROC) are built from scratch. Because the signal creation using GEMs relies on electron collection at the pad plane instead of the induced mirror charge of the ions created in MWPCs, the readout electronics have to be adapted to the different polarity. Additionally, the immensely increased collision rate as well as the huge data volume in heavy-ion collisions require significant improvements of the readout rate and data transfer. A description of the readout electronics is out of the scope of this thesis, but can be found in [28].

In this section, the requirements on the performance of the GEM-based readout are presented. These requirements drive the design of the readout chambers and their operation parameters, which are described in Sec. 3.3.2. A detailed description of the TPC upgrade is available in [28, 35].

3.3.1 Requirements on the readout chambers

The readout chambers of the ALICE TPC upgrade are required to preserve the performance of Run 2. To quantify the performance, the energy resolution of the future TPC is defined by the width of the characteristic 5.89 keV photopeak of a ^{55}Fe source. In order to maintain the resolution of the MWPC readout, $\sigma(^{55}\text{Fe}) = 12\%$ is required. The increased heavy-ion collision rate of Run 3 leads to a large current density in the most occupied regions of the TPC ($r = 85\text{ cm}$) of about 10 nA cm^{-2} . In order to maintain the energy resolution in such an environment, a low ion backflow is essential. The specific requirements which are placed on the ROC design will be explained in the following sections.

Due to the ion backflow introduced by a GEM readout, space charge accumulates in the TPC drift volume, where it causes drift field distortions. The slow ion drift time of about 210 ms in Ne-CO₂-N₂ (90-10-5) from the readout to the central electrode [36] leads to a pile-up of space charge. At collision rates of 50 kHz, ions from about 10 000 interactions accumulate in the TPC volume. Every collision introduces a disk of ions drifting from the readout to the central electrode. Non-active regions along the sector boundaries, as well as local gain variations, break the symmetry of

the space-charge density. Additional variations in the interaction rate and charged particle multiplicity lead to space-charge fluctuations in time. In order to be able to correct the drift field distortions, dynamic space-charge maps will be created. They will be updated every 5 ms to cope with fluctuations. A detailed description of the correction procedure can be found in [28].

It was estimated that the TPC's momentum and position resolution of Run 2 can be maintained with an ion backflow of less than 1%. For the ALICE TPC, a gain of 2000 is foreseen. As of such, less than $\varepsilon = 20$ ions per incoming electron are allowed to drift back into the gas volume. This introduces space-point distortions of up to 10 cm in the $r\phi$ -direction [37]. Nonetheless, the sophisticated correction algorithm will be able to achieve a space-point resolution of the same order as the intrinsic detector resolution ($\mathcal{O}(0.1 - 1 \text{ mm})$).

3.3.2 Readout chamber design and operation

Ion backflow and energy resolution are competing factors. Decreasing IBF also decreases the electron transmission of a GEM (stack), and therefore the energy resolution. In order to meet the stringent requirements on the performance, a stack of 4 GEMs is necessary⁴. Only then, the energy resolution of $\sigma(^{55}\text{Fe}) = 12\%$ can be maintained while keeping the IBF below 1%.

The correlation between energy resolution and IBF can mostly be explained by the influence of the GEM facing the drift volume (GEM 1). A large percentage of ions from the amplification in GEM 1 directly enter the drift volume. Therefore, a low gain in GEM 1 would be favourable to minimize IBF. As a consequence, a lower number of electrons is created and will be transmitted to the holes of the next GEM. Since the number of electrons is already low at the first multiplication stage, a loss of only a few electrons between the first and second GEM has a large effect on the following multiplication, and hence the transmission of the whole stack. To optimize the energy resolution, a higher electron transmission and therefore gain is preferable.

In order to minimize the IBF of a GEM stack, most of the amplification is shifted towards the last GEM. Additionally, a low transfer field above this GEM minimizes ion transmission from the last to the previous GEM. The remaining ions are then blocked by the other GEMs. This effect can be improved by misaligning the hole patterns of GEMs in a stack.

For the ALICE TPC upgrade to keep the ion backflow low enough, a quadruple GEM stack is necessary. Two different types of GEMs are used (Fig. 3.5a). GEM 1 and GEM 4 have a standard pitch (S) of $140 \mu\text{m}$ while the pitch is doubled for GEM 2 and GEM 3 (large pitch, LP). Each GEM is rotated by 90 degrees with respect to the previous GEM.

Studies employing this S-LP-LP-S scheme using a small detector with $10 \times 10 \text{ cm}^2$ GEMs were done to find optimal voltage settings. Figure 3.5b shows the correlation of the energy resolution with the IBF in such a setup. There, ΔU_{GEM1} is varied

⁴Stacks of three GEMs were tested intensively, but could not meet the requirements.

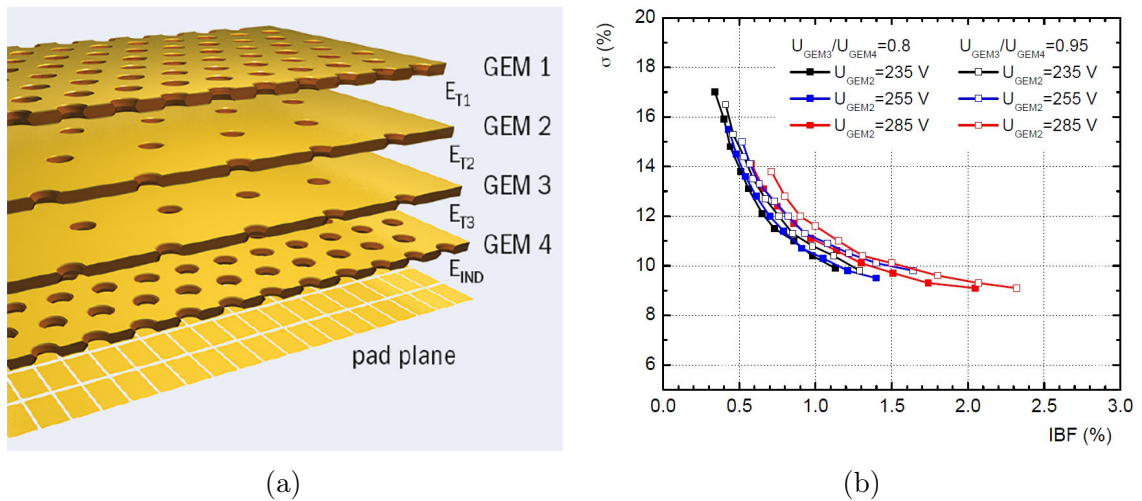


Figure 3.5: (a) Schematic view of the GEM stack design for the ALICE TPC upgrade. A S-LP-LP-S configuration is used, where layer 1 and 4 and layer 2 and 3 are rotated by 90 degrees with respect to each other. The transfer fields are denoted as E_i , $i = T1, T2, T3$ and the induction field as E_{IND} [38]. (b) Correlation between ion backflow and energy resolution using the characteristic 5.9 keV photopeak of ^{55}Fe in a quadruple S-LP-LP-S GEM detector in Ne-CO₂-N₂ (90-10-5) for various ΔU_{GEM2} settings. The voltage of GEM 1 increases in 10 V steps from 225 V to 315 V going from left to right in one curve. Voltages on GEM 3 and GEM 4 are adjusted such that a gain of 2000 is achieved while keeping their ratios fixed. The electric fields are $E_{T1} = E_{IND} = 4 \text{ kV cm}^{-1}$, $E_{T2} = 2 \text{ kV cm}^{-1}$, $E_{T3} = 0.1 \text{ kV cm}^{-1}$ [28].

ΔU_{GEM1}	ΔU_{GEM2}	ΔU_{GEM3}	ΔU_{GEM4}	E_{T1}	E_{T2}	E_{T3}	E_{IND}
270 V	230 V	288 V	359 V	$4 \frac{\text{kV}}{\text{cm}}$	$4 \frac{\text{kV}}{\text{cm}}$	$0.1 \frac{\text{kV}}{\text{cm}}$	$4 \frac{\text{kV}}{\text{cm}}$

Table 3.1: High voltage settings foreseen for the ALICE TPC upgrade with Ne-CO₂-N₂ (90-10-5) counting gas. The actual voltages of each chamber have to be slightly calibrated to reach the desired gain, energy resolution and ion backflow. The drift field is 400 V cm^{-1} [39].

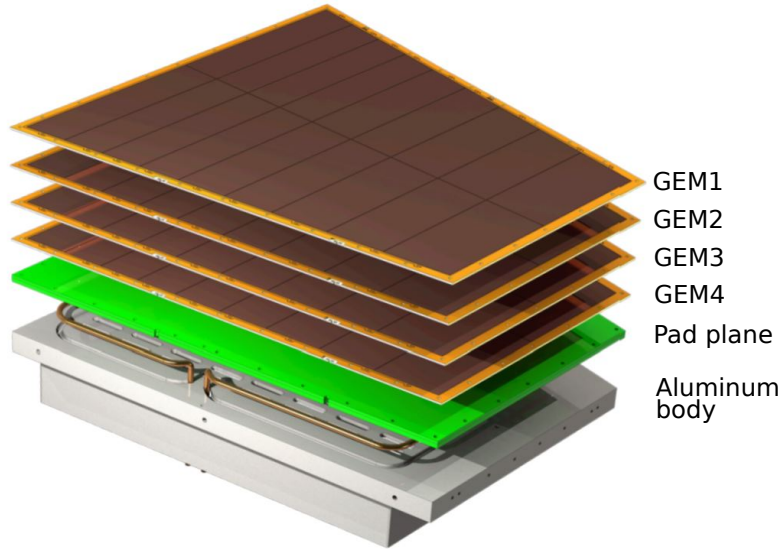


Figure 3.6: Exploded view of an inner readout chamber for the ALICE TPC upgrade utilizing GEMs. The segmentation of each foil can be seen [39].

from 225 V to 315 V in 10 V steps. Various GEM 2 voltage settings are investigated. The voltages on GEM 3 and GEM 4 are adjusted so that a gain of 2000 is achieved while the ratio of their voltages stays constant. Ne-CO₂-N₂ (90-10-5) is chosen over Ar-CO₂ (90-10) as a working gas, since ions move about 1.7 times faster in the neon-based gas mixture [36], which reduces the space-charge density in the TPC significantly. The competing nature of IBF and energy resolution is shown well in this measurement. For the TPC upgrade, the voltage settings of Table 3.1 have been chosen.

Figure 3.6 shows an exploded view of an inner readout chamber. Every ROC consists of a quadruple GEM stack that is mounted on a pad plane. Each GEM is separated by a 2 mm gap from each other or from the pad plane. An aluminium body holds the readout electronics and acts as a base of the readout chamber, which connects to the support structure of the TPC. The top side of every GEM is divided into segments with an area of about 100 cm², so that, in case of a discharge, less energy is released and less area is affected (cf. Sec. 4). The GEMs are powered by cascaded power supplies. Since the width of a single GEM foil is limited to 60 cm, three separate foils are needed to cover the whole area of an OROC. A photo of each foils size can be seen in figure 3.7. Foils of the inner readout chamber are labelled as I and foils of the OROC, going from smaller towards larger radii, as O1, O2 and O3.

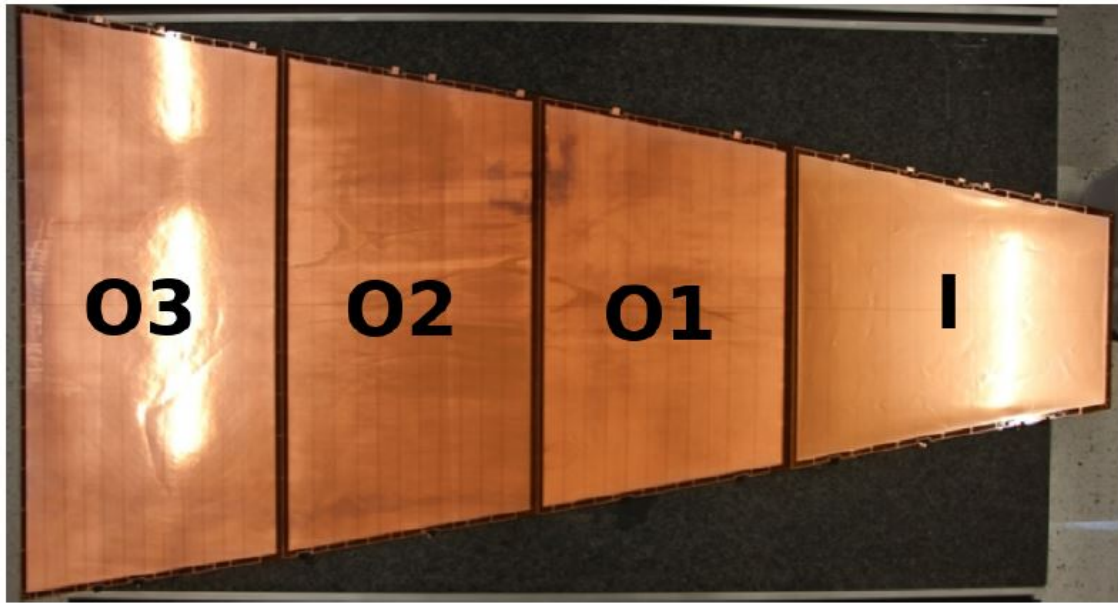


Figure 3.7: Photograph of GEM foils in all four sizes used to make one sector of the ALICE TPC [40]. Three foils of different sizes are used to make one OROC (O1, O2, O3), whereas an IROC utilizes only one foil size (I).

4 Discharges in GEM based detectors

A (gas) discharge describes the creation of a flow of electric current via ionization of the medium in an electric field. In general, the creation of a conducting channel through an insulating medium is also called *electric breakdown*.

The combination of strong electric fields and fragile microscopic structures makes *Micro-Pattern Gaseous Detectors* (MPGD) prone to electric discharges. High-energetic discharges can lead to mechanical damages of the material of a MPGD, which possibly alter performance parameters, or in the worst case create a mechanical short between the electrodes. This poses a severe threat to the operation of a detector. Therefore, the study of discharge physics is of great practical interest.

The GEM is a particular micro-pattern gaseous detector. This chapter gives an introduction to discharges in GEMs and presents discharge characteristics, which are relevant for the studies performed in Chapter 5. Additionally, several methods to mitigate discharges and the consequences for the ALICE TPC upgrade are discussed.

In general, the breakdown of a gas-filled gap between a cathode and an anode does not discriminate between a self-sustained current or a short circuit through the gap. The former implies the existence of a current through a path with finite electrical impedance that can be sustained by the power supply (PS) without a significant drop in the voltages. In contrast to that, a short circuit corresponds to a large current through a path with very low impedance, followed by the bridging of the electrode potentials. In order to discriminate the two cases, the latter will be referred to as *full breakdown*.

4.1 Streamer mechanism

A *streamer* is a weakly ionized, thin channel which can develop from a primary electron avalanche in a sufficiently strong electric field. The streamer can grow into either direction towards the electrodes or in both directions simultaneously. Upon reaching one of the electrodes, the streamer can modify the field so that the current and the level of ionization increase. If the streamer bridges the gap between the two electrodes, it can induce a *spark discharge* (Sec. 4.1.1).

In this section, a model of the streamer development is presented following the explanation in [41]. To simplify the process, a streamer in a strong, homogeneous electric field E_0 between a parallel cathode and anode is assumed. The electric field created by the space charge will be called E_Q .

In order to induce the growth of a streamer, the number of charges in a primary avalanche has to reach a critical number where the resulting electric field E_Q , created by the space charge, is of a similar strength as the external field E_0 . As a result, the

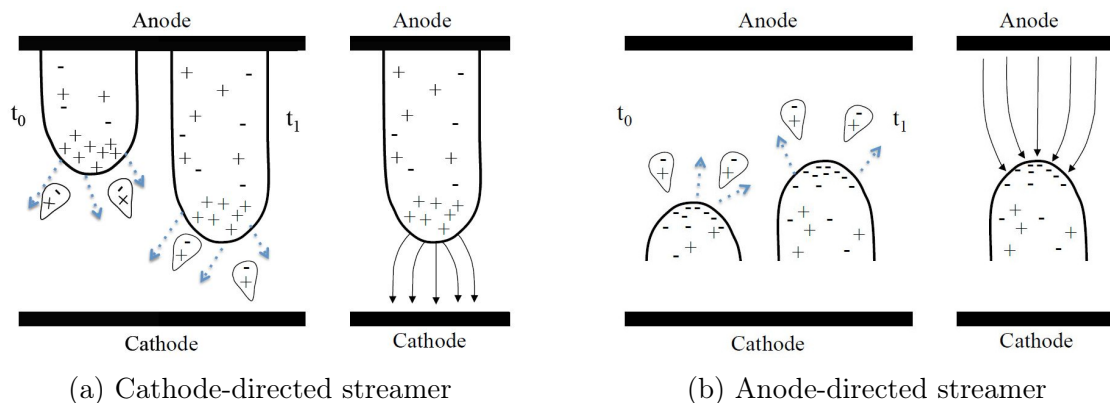


Figure 4.1: Streamer development at two moments in time, where $t_1 > t_0$ (left hand side of each figure). Electrical field lines created by the space-charge are sketched on the right hand side of each figure. Dashed lines represent photons. The outlines of the quasineutral plasma are indicated by the black lines. Cathode-directed streamers (a) evolve against, whereas anode-directed streamers (b) follow the direction of secondary avalanches. The figure has been taken from [36].

electric field, and therefore the gas amplification, is enhanced in the vicinity of the space charge. This is a necessary condition for the streamer to form, otherwise there is no reason to disrupt the regular avalanche growth. The time scale of an avalanche is governed by the electrons' velocity. Ions are usually slower than electrons by more than 2 orders of magnitude and can therefore be considered stationary.

Cathode-directed streamer

Figure 4.1a illustrates the growth of a cathode-directed streamer between two parallel electrodes. Electric field lines created by the streamer are indicated by black arrows. In this example, overvoltages are assumed to not be too high, so that a primary electron avalanche exhausts its reserves for amplification when it reaches the anode. Therefore, the space charge, which is composed of the remaining ions, is highest close to the anode and streamer development towards the cathode is initiated at the anode. Secondary avalanches, which are attracted to the positive streamer head, feed the growth. These avalanches are initiated by ionization due to photons created in the vicinity of the streamer head, or by photons created in the path of previous avalanches. Electrons that are liberated close to the streamer head accelerate towards it, eventually starting new avalanches. This again creates photons which start a next generation of secondary avalanches and so forth. The electrons intermix with the static ions and form a *quasineutral plasma*.

Because the (lightly) conducting streamer connects to the anode, it acts as a “metallic needle” which conducts the anode potential. Thus, the potential at the streamer head is significantly higher than in the unperturbed external field. Consequently the

electric field between the ion front and cathode is greatly enhanced. The more the streamer head approaches the cathode, the stronger the field becomes, which in turn accelerates the streamer growth. As the electric field is greatly enhanced, the drift velocity of electrons in this region is significantly higher than in the external field. Therefore streamers evolve with a velocity that can be up to one order of magnitude higher than the electron drift velocity.

Note that in more recent studies [42], simulations show that, under certain conditions, cathode-directed streamers can grow even without photoionization. Electrons near the positive ion front can diffuse against the field direction. Due to the strong ion density gradient at the streamer front, they are exposed to large electric fields, in which they are amplified. This propagates the ion front towards the cathode.

Anode-directed streamer

If an electron avalanche reaches the critical charge at a distance to the anode, the avalanche transforms into a streamer without connection to an electrode (Fig. 4.1b). It then can grow in both directions. The growth towards the cathode works as previously described. In the case of the anode-directed streamer, the streamer head consist of electrons. As this front approaches the anode, the electric field between them grows similar to the cathode-directed streamer. Because electrons from photoionization drift in the same direction as the streamer front, secondary avalanches start in front of it. The streamer head connects to the ionic trails of the secondary avalanches to form the plasma. As the negatively charged streamer head approaches the anode, the electric field between grows strongly, eventually leading to electron multiplication at the streamer front.

4.1.1 Spark formation

If a streamer connects both cathode and anode, a *spark* between the two electrodes can occur. It is characterized by a large current between cathode and anode as well as the release of a vast amount of photons. This can be seen by eye and is also accompanied by an audible shock wave. The spark evolves fast between the electrodes and usually only exists for a short moment. A famous example for a spark discharge is the *lightning*.

The original streamer is not capable of conducting such high currents. However, the transition from streamer to spark discharge is not fully understood. In [41], the spark formation is qualitatively described as follows: when the streamer grows from the anode towards the cathode, the potential of the streamer head is higher than that of the external, non-perturbed field at the same point. As the head approaches the cathode, the field in between them grows. Just before connecting to the cathode, this enhanced field leads to an immense amplification of electrons liberated from atoms or the cathode. A front of electrons is then propagating back along the streamer channel to the anode, similarly to the anode-directed streamer. The “reversed streamer” is close to the potential of cathode. Therefore, a strong potential difference and electric

field develops at the electron front. This process is much stronger than the original streamer, causing intense ionization.

When the highly ionized channel reaches the anode, a spark channel is created. A high current flows through it, which results in a full breakdown of the gap. During the discharge, the internal and external capacitances available, for example charges in the gas or the capacitance of the detector system, respectively, are exhausted. Joule heating⁵ increases the temperature in the channel rapidly to up to 20 000 K. Thus the gas expands, creating a cylindrical shock wave that can be heard. The temperature behind the front is high enough to thermally ionize the gas. Hence, the spark channel grows in diameter. The intense ionization and the high current through the spark channel are accompanied by the creation of many photons. The spark lasts until the energy stored in the system, for example in the capacitance of the detector system, is exhausted. Usually, the spark is quenched by a drop of the potentials between cathode and anode. If the power supply can sustain high enough currents through the spark channel, it can evolve into a permanent arc discharge.

In MPGD, discharges are usually accompanied by a spark. As this happens in the close proximity of the fragile structures of a MPGD, the heat and shock wave can pose a serious risk to the detector. Therefore, it is crucial to understand the discharge formation and how to mitigate it. A review of discharge studies for MPGD can be found in [43]. The studies presented in Sec. 5 focus on discharges in GEM-based detectors. Section 4.2 and 4.3 summarize the main characteristics of discharges in GEMs, including possible damages and methods to mitigate them.

4.2 Primary discharges

A so-called *primary discharge* in a GEM foil is a full breakdown between the GEM top and bottom electrodes through one of the holes. If a critical amount of charge accumulates in a hole [44], for example due to a highly-ionizing particle in the vicinity of a GEM, a streamer evolves between the two electrodes. Eventually, it connects both sides which results in a spark temporarily shorting the GEM.

In this section, different aspects of the primary discharge are presented. First, the discharge mechanism is described. Then, the current knowledge on primary discharge propagation from one GEM to another is summarized. Based on these findings, different methods to mitigate discharges are presented. Since it is impossible to fully avoid them in high rate and multiplicity environments, factors that influence the strength of the discharge are identified in order to minimize them.

⁵Joule heating, or Ohmic heating, describes the heating of a conducting passage by an electric current. The generated power of heating is proportional to the resistance and the square of the current.

Streamer growth in GEM holes

By applying a voltage ΔU_{GEM} across the GEM, a strong electric field E_0 in the hole of the GEM is created. In the following, this field will also be called *external field*. As electrons approach the hole, avalanche multiplication through the hole occurs. Let Q be the amount of charge created in the hole. The space charge accumulated at the base of the hole produces an electrical field E_Q .

In order to create a streamer, the combined electric field created by the GEM (E_0) and by the space charge (E_Q) needs to be strong enough for gas amplification. In the following calculation, the amount of charge carriers needed to create such a field is estimated, closely following what is presented in [36]. This will also give an estimate of the minimum amount of electrons that have to enter a GEM hole to create a primary discharge.

For the estimation, a spherical space charge with radius $R_Q = 25 \mu\text{m}$ is assumed, which corresponds to half of the GEM hole diameter. The calculation is done for Ar-CO₂ (90-10), as it is used for most of the studies presented in this thesis (Sec. 5). Gas amplification starts at slightly lower fields than 10 kV cm^{-1} at room temperature and atmospheric pressure [28, 36]. This leads to the following condition for gas breakdown in the GEM hole:

$$\begin{aligned} \frac{10 \text{ kV}}{\text{cm}} &< E_0 + E_Q \\ \frac{10 \text{ kV}}{\text{cm}} &< E_0 + \frac{eN_{ion}}{4\pi\epsilon_0\epsilon_r R_Q^2} \\ \frac{1 \text{ V}}{\mu\text{m}} &< E_0 + \frac{eN_{ion}}{4\pi\epsilon_0\epsilon_r (25 \mu\text{m})^2}. \end{aligned} \tag{4.1}$$

Here, N_{ion} corresponds to the number of ions, ϵ_0 and ϵ_r are the permittivity of the vacuum and the relative permittivity of the medium, respectively.

In the region where most ions are created—the lower end of the hole (cf. Fig. 3.4b)—the external electric field is not strong enough anymore for further amplification. Therefore E_0 is neglected. In a sphere with $R_Q = 25 \mu\text{m}$, the number of ions N_{ion} necessary for E_Q to be large enough to create further ionization is

$$N_{ion} > \frac{1 \text{ V}}{\mu\text{m}} \frac{4\pi\epsilon_0 \cdot 1 \cdot (25 \mu\text{m})^2}{e} \sim 0.4 \times 10^6, \tag{4.2}$$

where we used the approximation $\epsilon_r = 1$. This calculation gives us the order of magnitude of N_{ion} . As the radius R_Q is arbitrarily chosen and cannot be observed, it poses the biggest uncertainty to this calculation. Varying R_Q by $\pm 10 \mu\text{m}$ leads to $N_{ion} \sim (0.2 - 0.9) \times 10^6$. In [44] the *critical charge* to create a discharge in a GEM hole is found to be $(5.0 \pm 0.3) \times 10^6$ in Ar-CO₂ (90-10), which is of similar order as the rough estimate presented here.

Given the number of ions N_{ion} after multiplication and the gas gain, one can estimate the number of electrons that have to enter a GEM hole to induce a discharge.

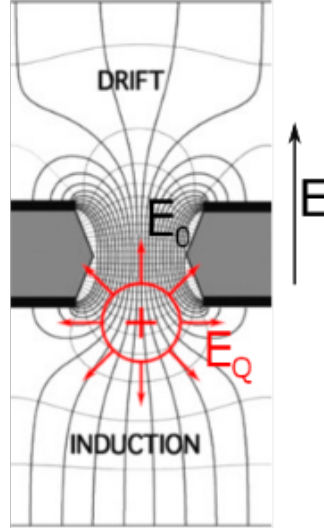


Figure 4.2: Sketch of the space-charge after the amplification process in a GEM hole. The black lines represent the external field E_0 . The direction of the field is indicated by an arrow on the right. Positive space charge has accumulated at the bottom of the hole. The charge is assumed to be spherical and its electrical field E_Q is depicted in red. The effective field $E_0 + E_Q$ increases towards the center of the hole. The figure has been adapted from [31].

Using a single-GEM detector, the authors of [44] observe primary discharges at a gain of $G_{discharge} \approx 500$, which corresponds to $\Delta U_{GEM} \approx 400$ V in Ar-CO₂ (90-10). A similar voltage is also seen to cause discharges in the work presented in chapter 5. Using this value, the number of electrons that need to enter one hole to cause a discharge can be estimated to be

$$N_e = \frac{N_{ion}}{G_{discharge}} \sim \frac{(0.2 - 0.9) \times 10^6}{500} = 400 - 1800. \quad (4.3)$$

The presentation above is a simplified description of the situation. Further effects have to be considered in order to have a more realistic description. They are listed below.

The externally applied electric field E_0 has to be accounted for. The radial field E_Q from the space charge superimposes with E_0 , which leads to an enhancement above or a weakening of the local field below the space charge (Fig. 4.2). Additionally, constraints of the external field cause the ions to rather form an ellipsoid or disk than a sphere. Moreover, they slowly drift towards the top of the GEM, where the field strength increases again. Given these factors, the number of ions necessary to reach the streamer condition (Eq. 4.1) can be lower. On the other hand, charge screening effects can also reduce the E_0 experienced by the ions, in which case a higher N_{ion} is needed to reach the streamer condition. On top of that, other effects

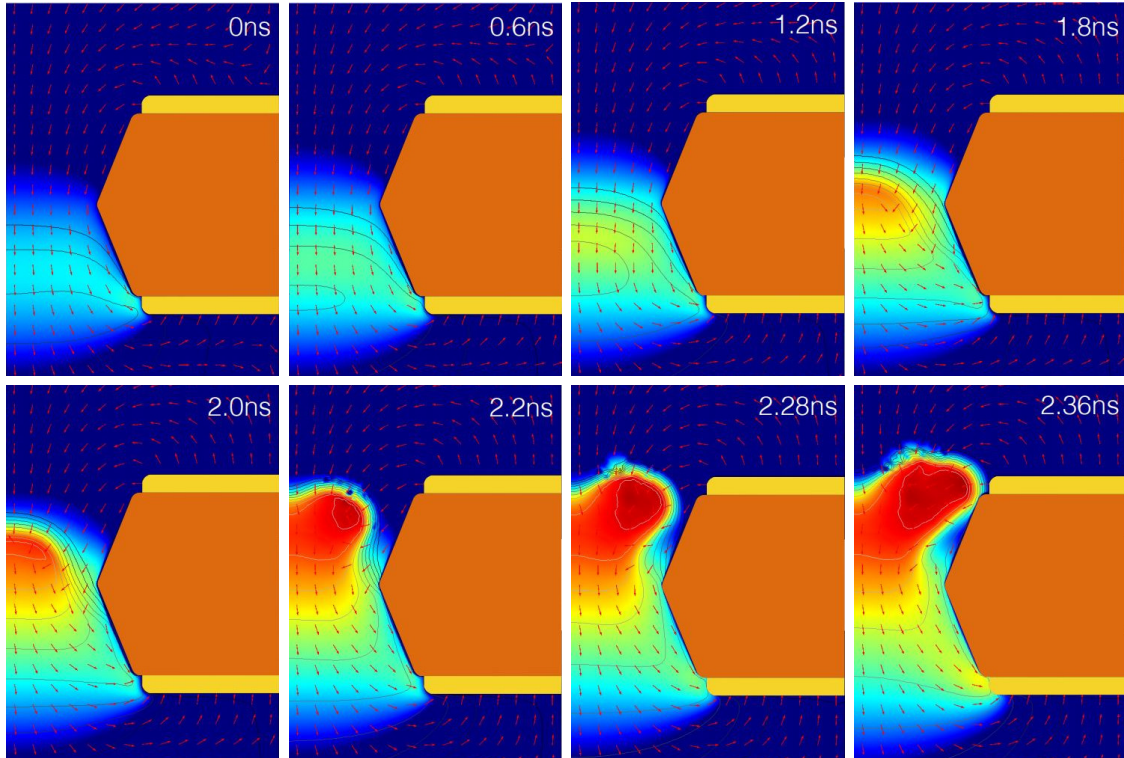


Figure 4.3: Simulation of the streamer development in a GEM hole. The red arrows correspond to electrical field lines and the blue to red colour scale to the ion density. [45]

such as different hole geometries from different production processes or defects can have an influence on the number of charge carriers necessary to fulfil the streamer condition.

Since the electric fields E_0 and E_Q add up between the space-charge and the GEM top electrode, the streamer starts to grow towards the cathode (Fig. 4.3). Above the ion cloud, the electric field is the strongest. Electrons that enter the hole after the bulk of charges was amplified, or that are liberated by photoionization, start amplification processes above the space-charge. The streamer starts to grow a weakly conducting path towards the cathode, following the multiplication backwards. When the positively-charged streamer head connects to the top electrode, the streamer acts as a conductor with a certain resistance. The other end of the streamer is located close to the bottom electrode, where the initial avalanche deposited most of the ions. The large potential difference and the small distance between the streamer's end and GEM bottom causes a large local electric field, which accelerates the anode-directed streamer growth. Eventually, GEM top and bottom are connected through the weakly conductive path of the streamer. As a consequence, a spark channel is created that shortens both sides (cf. Sec. 4.1.1). In the measurements of this thesis, the potentials approach each other within 10 ns (Fig. 4.4a). A more precise time estimate cannot be made as the reaction time of the employed high-voltage probes is not

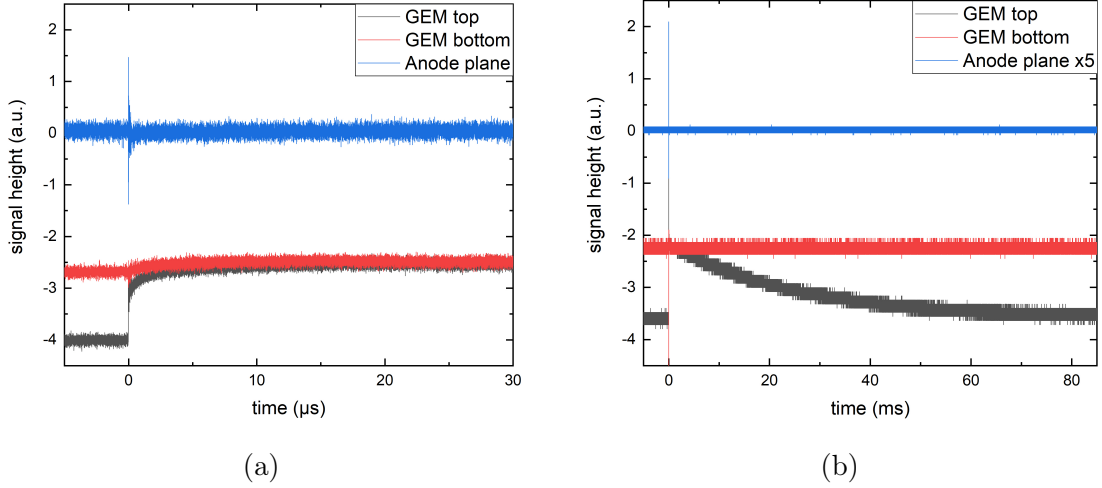


Figure 4.4: High voltage probe signals of a GEM during a primary discharge. After the primary discharge at $t \approx 0 \mu\text{s}$, the GEM top potential (black) drops to the bottom potential (red) in less than 10 ns. A strong signal is induced on the anode plane (blue). Note the different magnitudes of the horizontal axes. A detailed description of the experimental setup can be found in section 5.1. The waveforms have been recorded (a) in Ar-CO₂ (90-10) at an induction field of 4.5 kV cm^{-1} , a drift field of 440 V cm^{-1} , $\Delta U_{GEM} = 416 \text{ V}$ with $R_{top} = 5 \text{ M}\Omega$ and $R_{bot} = 0$. (b) in Ne-CO₂-N₂ (90-10-5) at an induction field of 3.75 kV cm^{-1} , a drift field of 433 V cm^{-1} , $\Delta U_{GEM} = 468 \text{ V}$ with $R_{top} = 5 \text{ M}\Omega$ and $R_{bot} = 0$.

known. The spark is accompanied by the release of many photons that can easily be observed by eye. A photo of a discharge can be seen in Fig. 4.5b.

Propagation of primary discharges

It was observed that, when GEMs are operated in a stack, a primary discharge in one GEM can lead to a primary discharge in another GEM in less than 10 ns [36, 46, 47]. It is said that the discharge *propagated* to another GEM. The time scale on which this happens excludes charge carriers crossing the gap as a cause, since electrons would need about 40 ns to cross a 2 mm gap in electric fields in the range between 1 kV cm^{-1} and 5 kV cm^{-1} [36]. Therefore it is likely that photons created in the initial primary discharge cause ionization of the gas close to a hole of another GEM, or eject electrons from the GEM material. The resulting electrons drift into the hole where they are amplified. If enough photoionization takes place, the critical charge for a streamer is reached and the GEM discharges.

Discharges were found to propagate both from the upper GEM to the lower GEM and vice versa. The field direction seems to have a slight influence on the propagation probability, but does not prevent propagation [46]. Bachmann et al. also found that at constant transfer field strengths, the propagation probability depends strongly

on the voltage difference across the GEM to which the discharge is propagated to. When exceeding a certain voltage, the probability of propagation rises from 0 to 1 within a 20–50 V window.

In recent measurements [48] it was found that the propagation probability P_{Prop} also depends on the electric field between two GEMs. At constant voltages across the GEMs, a linear increase of P_{Prop} with the electric field was found.

The conclusions on this effect are not final and the topic requires further investigations.

Mitigation of primary discharges

During the operation of a GEM-based readout, it is desirable to have as few discharges as possible. As the primary discharge is caused by large electric charge densities in a GEM hole, the reduction of charge accumulation is crucial to minimize the discharge occurrence. In a GEM stack, each foil can be operated at a lower ΔU_{GEM} than in a single-GEM detector, while achieving the same overall gain. Consequently, a higher space charge in the reduced field in a GEM hole is needed to transition from the avalanche to a streamer. Moreover, the discharge propagation from one foil to another is reduced [46].

Furthermore, the electron cloud is subject to transversal diffusion while drifting from one GEM to the following one. The significance of this effect in the upgraded ALICE TPC is estimated here, based on simulations of electron diffusion in a magnetic field of $B = 0.5$ T, which corresponds to the magnetic field of the ALICE TPC, in Ne-CO₂-N₂ (90-10-5) [37]. For this estimation, a constant electric field between the GEMs is assumed. This obviously does not hold in the close proximity of a GEM, but it suffices for a qualitative discussion.

From the classical kinetic theory of gases, one finds that the diffusion of electrons in a gas follows a Gaussian distribution. The width in transversal direction is increasing with time as

$$\sigma_t^2 = 2D_t t = \frac{2D_t}{v_D} d, \quad (4.4)$$

where D_t and v_D correspond to the transversal diffusion coefficient and the drift velocity, respectively. Both values depend strongly on the gas mixture, the electric field and environmental parameters. In the case of ALICE, a magnetic field parallel to the electric field is employed. This has a strong focusing effect on the electron cloud, which spreads perpendicular to the magnetic field lines, therefore reducing D_t . The drift time and distance are given by t and d , respectively. A commonly used quantity, derived from Eq. 4.4, is the *drift length independent diffusion coefficient* D_T , which characterizes the diffusion of electrons in a gas in units of $\mu\text{m}/\sqrt{\text{cm}}$:

$$D_T = \frac{\sigma_t}{\sqrt{d}} \quad (4.5)$$

In the future ALICE TPC readout, an electric field of 4 kV cm^{-1} is applied in the first (T1) and second (T2) transfer gap, while there is only a 0.1 kV cm^{-1} field in T3

to minimize the ion backflow (cf. Sec. 3.3.2). The foils at the bottom of each gap are of the large pitch type (280 μm) for T1 and T2 and standard pitch type (140 μm) for T3. From the transverse diffusion coefficients D_T simulated in [37], the spread of the electron cloud per gap (2 mm) is found to be $\sigma_t(E = 4 \text{ kV cm}^{-1}) \approx 135 \mu\text{m}$ in T1 and T2 and $\sigma_t(E = 0.1 \text{ kV cm}^{-1}) \approx 100 \mu\text{m}$ in T3. Electrons are assumed to be collected in a hole if they are within half of the pitch size of the lower foil, i.e. within 140 μm for T1 and T2 and 70 μm for T3, from the center of the hole after crossing the gap. Hence, only a small fraction of electrons are shared in the middle layers, while a considerable amount is spread over several neighbouring holes in the last layer, where most of the amplification occurs. Considering the misalignment of the GEMs, this effect is enhanced in all layers. This results in a significantly reduced charge density in the individual GEM holes. It was found in [46] that the primary discharge probability in a GEM stack is reduced by about an order of magnitude per additional (standard design) GEM at the same effective gain⁶.

Damages by primary discharges

During a primary discharge, the energy stored in the GEM foil is released. This energy can be approximated by the formula of the energy stored in a capacitor:

$$E_C = \frac{1}{2} C_{GEM} (\Delta U_{GEM})^2 \quad (4.6)$$

For a $10 \times 10 \text{ cm}^2$ standard design GEM foil, the capacitance C_{GEM} is approximately 5 nF. This results in a stored energy of $E_C \approx 400 \mu\text{J}$ for $\Delta U_{GEM} = 400 \text{ V}$. Here we assume that the GEM is properly decoupled from the power supply and no parasitic capacitances, for example from cables, are present. When the energy is released in a discharge, a large amount of heat is released. The following expansion of the gas in this area leads to an audible cracking noise. The heat damages the foil components. Electron microscope photos of GEM holes after a single discharge show damages of the polyimide layer as well as melted copper, which is projected away from the hole. Figure 4.5a shows such a photo. The damage can sometimes be seen by eye as a dark spot around one or several holes. Damages can range from the ones depicted in the figure over strong deformations of the hole, to a permanent mechanical short between the top and bottom sides of the GEM. The authors in [49] found that a GEM can withstand several thousands of radiation induced discharges per hole before a short occurs, given that the capacitances are small ($\sim 5 \text{ nF}$) and the GEM is decoupled from the power supply path.

In order to minimize the damage from a primary discharge, the energy and duration of the discharge have to be reduced. The latter can be realized by adding a resistor R_{top} to the top side of the GEM. In the event of a discharge, the top potential drops to the lower bottom potential. The power supply then needs to charge the top

⁶The effective gain corresponds to the amount of charge collected at the anode divided by the primary charge. A fraction of charge is collected by the GEM electrodes or the gas. These are not taken into account.

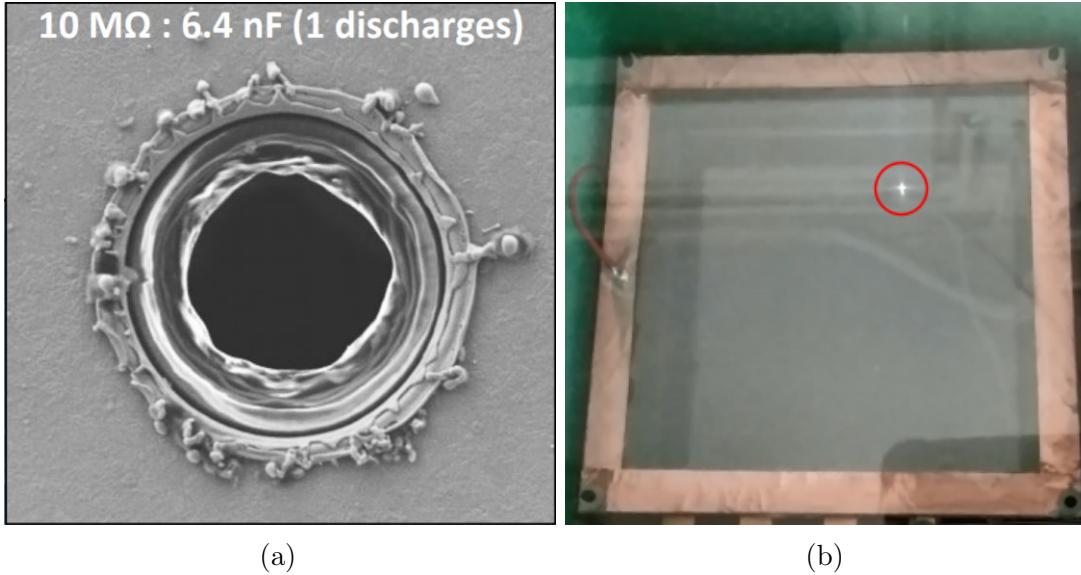


Figure 4.5: (a) Electron microscope picture of a single GEM hole after one primary discharge in Ar-CO₂ (70-30). A 10 MΩ loading resistor is used. The capacitance and powering scheme differs from the one used in the upgraded ALICE TPC and the studies of this thesis. Therefore the magnitude of damage can differ. Here, a deformation of the polyimide layer can be seen. Additionally, the copper around the hole melts during a discharge and rolls up on itself. Copper residues are projected away from the hole [49]. (b) Photo of a discharge in a 10 × 10 cm² standard GEM. The picture was extracted from a video recorded at a rate of 30 frames/s with a simple mobile phone camera. A description of the setup can be found in Sec. 5.1. The structure seen on top is the cathode mesh, whereas the discharge happens in the GEM underneath.

potential up to its nominal value. The charging towards the applied voltage can be described by

$$U(t) = U_{GEM}(1 - e^{-t/\tau}), \quad (4.7)$$

where τ is the RC time constant $\tau = RC$ and U_{GEM} is the nominal voltage across the GEM. In case of $R_{top} = 5 \text{ M}\Omega$ and $C_{GEM} = 5 \text{ nF}$, the RC time constant is 25 ms. Hence, the time until the full ΔU_{GEM} is recovered is of the order of 100 ms. The fact that the voltage across the GEM is reduced for such a long time after a primary discharge quenches the spark (Fig. 4.4).

Following equation 4.6, minimizing the energy can be achieved through the capacitance and the voltage across the GEM. The former suggests to keep the area of the GEM as small as possible. This can be realized by either using many small GEMs or by segmenting large area GEMs. An additional advantage of this design is that in the case of a permanent damage, only a small fraction of the active area becomes dysfunctional. It is also important to reduce parasitic capacitances. In large high-energy physics experiments, it is often necessary to power the detectors with extremely long high-voltage cables. If the GEM is not decoupled from the cable, additional capacitances will contribute to the energy released in the discharge too. To avoid this, a *decoupling resistor* in the high voltage path of the bottom electrode can be added. It should sit as close to the GEM as possible.

When employing a stack of GEMs, a lower ΔU_{GEM} per GEM foil can be employed to reach the same gain as with a single-GEM detector. Due to the dependence of the energy in a discharge on $(\Delta U_{GEM})^2$, the amount of released energy, and therefore also heat, sinks drastically.

4.3 Secondary discharges

In addition to the initial discharge between a GEM's top and bottom sides, it was found that under certain conditions a subsequent full breakdown of the gap between two adjacent GEMs or a GEM and the anode plane can occur. The phenomenon of a discharge between a GEM and the anode was first reported by V. Peskov *et al.* as *delayed breakdown* [43]. Moreover, it seems that the *fully propagated discharges* observed in [46] also correspond to what we call *secondary discharges*. Only later in studies with a single-GEM detector it was observed that the probability for a secondary discharge to occur depends on the strength of the field between the GEM and the anode, the so-called induction field E_{Ind} [50]. Furthermore, Gasik *et al.* found that secondary discharges only occur after a primary discharge, which explains the choice of names. A characteristic feature of the secondary discharge is that the probability to occur rises sharply from 0 to 1 when a threshold in the electric field above or below a GEM is passed. The study of secondary discharges was then greatly extended by [36] and [47]. In a recent research effort with our collaborators, many complementary measurements were combined to extend the knowledge and a mechanism for the production of the secondary discharge is proposed [48]. However,

further research is needed to confirm and further extend the findings. The research presented in this thesis is a part of this work.

In order to understand the motivation of this work and to be able to follow the studies presented in Chapter 5 in greater detail, a summary of the knowledge about secondary discharges, that was obtained before the writing of this thesis, is given in this section. A complete discussion of the mechanism of secondary discharges is presented in Sec. 5.9.3.

Basic properties

A *secondary discharge* corresponds to a full breakdown in the gas gap between two adjacent GEMs or a GEM and the anode plane (Fig. 4.6a). It has only been observed to occur after a primary discharge in at least one GEM. Recent recordings with a high-speed camera confirm that the secondary discharge develops directly underneath or above the initial discharge⁷ [51].

It was first found by P. Gasik et al. in single-GEM studies that secondary discharges only occur after a critical electric field strength E_{ind} in the induction gap—the gap between the GEM and anode plane—is reached. The probability of observing a secondary discharge then rises quickly from 0 to 1 if the electric field is further increased. Moreover, the mean time between primary and secondary discharge decreases exponentially with increasing electric field: from several 10 μs to less than 1 μs when powering the set-up with individual channel power supplies [50]. The electron drift time ($\sim 50\text{ ns}$ through the 2 mm gap) is shorter by several orders of magnitude. Ions would need about 15 μs to cross the 2 mm gap. However, the decrease in time between initial and secondary discharge for increasing fields is much stronger than the decrease in ion drift time. Furthermore, the electric field direction transports the ions towards GEM top. Therefore, charge carriers produced during the primary discharge crossing the gap cannot be fully responsible for the secondary discharge. These studies have then been reproduced by A. Deisting [36] and extended to studies of secondary discharges between two adjacent GEMs, in the so-called *transfer field*. It was observed that the onset field E^{on} of secondary discharges, which is defined as the field at which $P_2 = 0.5$, is systematically earlier for the field between two GEMs than for E_{Ind} . No dependence on the voltage across the GEM ΔU_{GEM} could be identified in a narrow range of $400\text{ V} < \Delta U_{GEM} < 440\text{ V}$.

Secondary discharges - An effect in the gas

In [36], the anode potential was investigated while employing a high resistance to ground in the attenuator. This increases the sensitivity of the oscilloscope signal to small currents. An increase of the anode potential is observed after the primary

⁷In the measurements in [51], only secondary discharges between the GEM and anode plane have been investigated, therefore they only occur underneath the GEM. However, it was found in [48] that secondary discharges can also evolve above a GEM hole against the direction of the electric field.

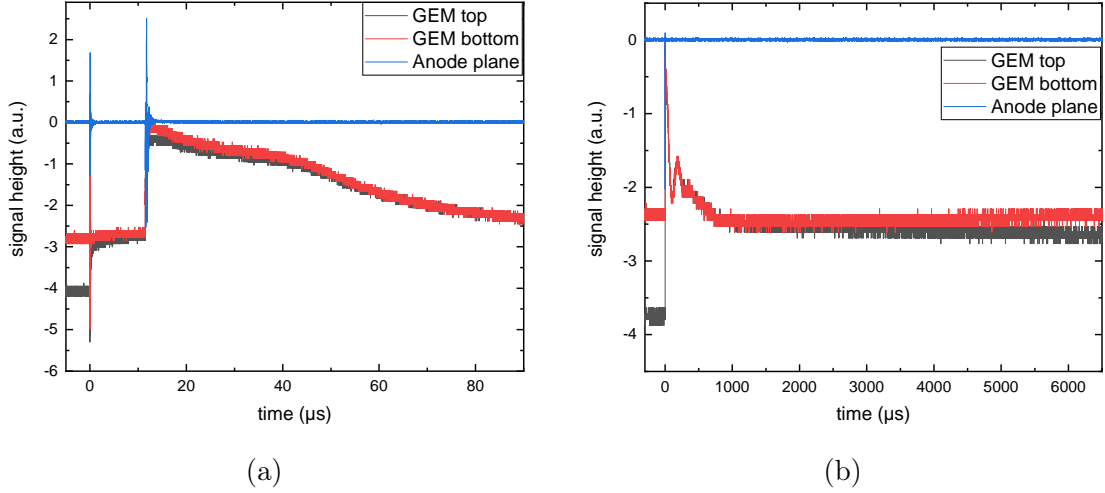


Figure 4.6: High voltage probe signals displaying a primary and a secondary discharge in the induction gap of a single-GEM detector. After the primary discharge ($t = 12 \mu\text{s}$, the GEM top and bottom electrodes are on the same potential. At the time of the secondary discharge ($t \sim 12 \mu\text{s}$ in (a)), both drop towards the anode potential. A detailed description of the experimental set-up can be found in section 5.1. (a) Secondary discharge recorded in Ar-CO₂ (90-10) at an induction field of 4.5 kV cm^{-1} , a drift field of 440 V cm^{-1} , $\Delta U_{GEM} = 416 \text{ V}$ with $R_{top} = 5 \text{ M}\Omega$ and $R_{bot} = 0$. Oscillations in the anode shortly after the discharges can be seen. (b) During the recovery of the potentials from the secondary discharge, oscillations are visible. It takes about 1 ms until the nominal GEM bottom voltage is reached again. Then, the recovery of the GEM top potential as in a primary discharge (cf. Fig. 4.4b) starts. Therefore, a secondary discharge does not significantly increase the recovery time of the GEM. The waveform was recorded in Ne-CO₂-N₂ (90-10-5) at an induction field of 4 kV cm^{-1} , a drift field of 428 V cm^{-1} , $\Delta U_{GEM} = 467 \text{ V}$ with $R_{top} = 5 \text{ M}\Omega$ and $R_{bot} = 0$.

discharge, which decays over 10 μs to 20 μs . This is a strong indication for a current through the induction gap. The current increases again approximately 1 μs before the secondary discharge. This feature points to a mechanism in the gas building up the secondary discharge.

In order to identify if the observed features are a result of the counting gas or the electric circuit elements, several tests with Gas Discharge Tubes (GDTs), which allow to decouple the electric circuit elements from the gas, were carried out. A GDT is a gas filled container with two electrodes which is designed to discharge when the applied voltage exceeds its nominal breakdown voltage. It was found that the secondary discharge is not caused by the electric components, but is an effect in the gas [48].

Dependence on the gas mixture

Secondary discharges appear at different electric field strengths in different gas mixtures [48, 52]. In Ne-CO₂-N₂ (90-10-5) secondary discharges start to appear at transfer fields about 20 % lower than in Ar-CO₂ (90-10). The time between primary and secondary discharges in the neon-based mixture was found to be significantly smaller than in argon, which could be a result of higher electron and ion drift velocities in neon than in argon [36].

Effects of the biasing scheme

Parasitic capacitances introduced by long cables shift the onset of secondary discharges to lower electric fields. However, the dependence on the cable length can be removed to a large degree by introducing a *decoupling resistor* $R_{bot} \sim 100 \text{ k}\Omega$ as close to the bottom side of the GEMs as possible [53]. When comparing measurements with different decoupling resistors from $R_{bot} = 0$ to $R_{bot} = 100 \text{ k}\Omega$ and otherwise unchanged set-up, the onset of secondary discharges moves to higher electric fields proportional to the amount of resistance [36, 47, 48].

Biasing the detector with a cascaded power supply or distributing the voltages via a resistor chain, instead of using individual channel power supplies, also changes the onset field to higher values. This could be a result of a different GEM potential evolution after the primary discharge, effectively changing the electric field, since over-voltages between electrodes are suppressed with either cascaded PS or a resistor chain. In addition, the time between the initial and secondary discharge drops by about one order of magnitude when using a resistor chain [36]. Choosing a power supply that allows to apply higher electric fields until secondary discharges occur can therefore improve the safety of the detector.

Reignition of secondary discharges

In the measurements conducted in this thesis, it was observed that sometimes a few μs after a secondary discharge, the GEM potentials drop towards the anode again (Fig. 4.7). This seems to occur randomly. Using a high-speed camera, it was found in

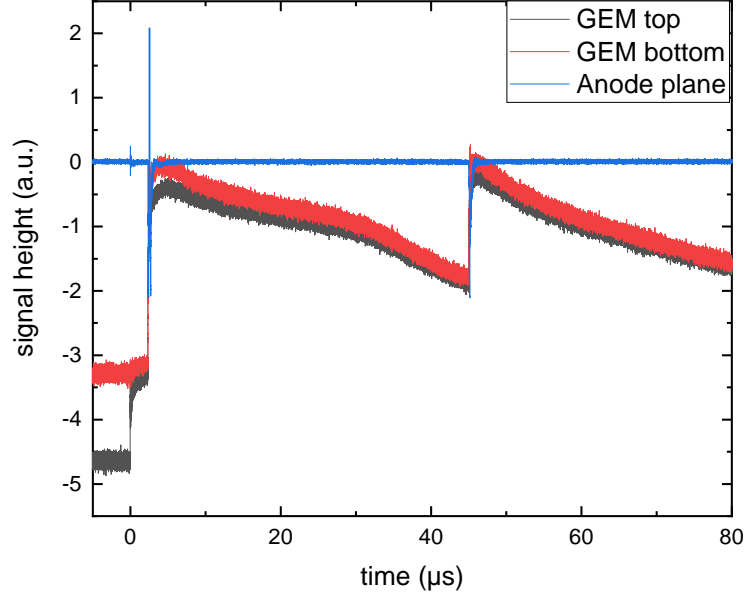


Figure 4.7: High voltage probe signals displaying a secondary discharge ($t \sim 3 \mu\text{s}$) that is reignited ($t \sim 45 \mu\text{s}$). The waveform was recorded in Ar-CO₂ (90-10) at $E_{Ind} = 5.5 \text{ kV cm}^{-1}$, $E_{Drift} = 435 \text{ V cm}^{-1}$, $\Delta U_{GEM} = 415 \text{ V}$, $R_{top} = 5 \text{ M}\Omega$ and $R_{bot} = 0$.

[51] that these additional potential drops are caused by a reignition of the secondary discharge, at the same position as the original one.

Dependence on mechanical parameters

Exchanging a GEM by the same type in a setup affects the onset by as much as 15%. It does not seem reasonable that mechanical misalignment when changing a GEM can cause large deviations like this. However, the bending of GEM frames could slightly decrease the distances in the detector locally, which increases the electric field [47]. Another hypothesis is that production parameters such as hole geometries or material thickness play a role. Therefore one needs to be cautious when comparing measurements that use different GEMs.

Mitigation of secondary discharges

In order to minimize the occurrence of secondary discharges, one wants to operate the detector at electric fields that are lower than the onset of secondary discharges. Based on the observations above, the following ways to increase the onset are found: 1) Maximizing the resistance of the decoupling resistor on GEM bottom, 2) optimizing the gas mixture for stability against secondary discharges, for example by using an argon-based instead of neon-based gas mixture, or by adding more quencher, 3)

powering the GEM stack with a cascaded PS or using a resistor chain to distribute the voltages instead of using individual channel power supplies for every electrode.

The damages caused by secondary discharges are not well documented. However, since much larger potential differences are involved, the energy of such a discharge is usually larger than in the case of the primary discharge.

4.4 Consequences for the operation of GEM stacks

Discharges in a GEM stack and the subsequent potential changes have a big impact on the performance and safety of the detector. Before discussing how primary and secondary discharges affect the data taking of the upgraded ALICE TPC, it is presented what measures are taken to mitigate the occurrence of and the damage caused by discharges.

In the upgraded TPC, a stack of four GEMs will be utilised as amplification stage. Since the electron multiplication is shared between all GEMs, a relatively low ΔU_{GEM} per foil can be used, which decreases the charge density in the holes and the energies released in discharges. Additionally, diffusion of the electron clouds between the stacks reduces the likelihood of primary discharges to occur. GEMs with different pitch size are rotated with respect to each other (Sec. 3.3.2) to spread the charges over several holes, which reduces the probability of primary discharges further. In case of a primary discharge, the GEM top potential drops towards the bottom potential. A $5\text{ M}\Omega$ resistor on the top side ensures that the spark is quenched (cf. Sec. 4.2). Furthermore, each GEM top side is divided into segments of about 100 cm^2 , so that a smaller area is affected by a discharge and less energy is released. A $100\text{ k}\Omega$ resistor on GEM bottom decouples the GEMs from the power supply and shifts the occurrence of secondary discharges to higher electric fields.

Recovery from discharges

The full recovery of the GEM potentials after a primary discharge in a $10 \times 10\text{ cm}^2$ large GEM takes about 100 ms. When using an individual channel PS, this time is not significantly altered by the occurrence of a secondary discharge. Since the segments of the top sides of the GEMs for the ALICE TPC upgrade have similar areas, the recovery time from a primary discharge is comparable. During a secondary discharge, however, the potential of the full, unsegmented bottom side of a GEM drops. In this case the recharging of the potential might take longer because of the larger area. We are not aware of any dedicated measurement of the recovery from secondary discharges in a full-sized ROC. Therefore a recovery time of 100 ms is assumed in the following discussion.

The ROCs of the upgraded ALICE TPC will be powered with cascaded power supplies, i.e. each potential in the stack uses the previous potential as ground and the absolute voltages are defined by the chosen voltage differences between subsequent potentials.

Therefore, when a discharge occurs, the voltage differences between all non-discharging GEM electrodes are kept constant, while in the electrodes that are affected by a discharge, $\Delta U = 0$ V is maintained until the recovery starts. The effects of a primary or secondary discharge on the voltages and electric fields in a GEM stack are presented in the following. A stack of two GEMs is considered, where capacitive coupling and other (time dependent) effects are ignored. Let the upper GEM (GEM 1) face the drift cathode and be on a more negative potential than the lower GEM (GEM 2), which faces the (grounded) anode plane. In the following, a potential drop (rise) refers to a quick change of the potential towards less (more) negative values. The potentials in case of a primary and a secondary discharge between the GEMs are sketched in Fig. 4.8.

When a primary discharge occurs, the potential of the discharging segment of GEM top drops towards the less negative bottom potential. Due to the 100 k Ω decoupling resistor, the GEM bottom potential moves slightly towards the GEM top. Since the absolute voltage of all non-discharging GEM top potentials is dependent on GEM bottom, their absolute voltages increase slightly too.

A secondary discharge between two GEMs causes a drop of the GEM 1 bottom and a rise of the GEM 2 top potential. It was observed that during a secondary discharge, the GEM that did not have the primary discharge (in this example GEM 2) will shorten too⁸ [47]. Thus, the discharging GEM 1 and GEM 2 top potential are at the same value as their respective bottom potential. However, the two GEMs do not necessarily meet at the same potential [36, 47]. As a consequence, the electric fields below GEM 2, between the two GEMs and above GEM 1 are altered. In this discussion, other effects that can shift the GEM potentials have been ignored. These include capacitive coupling between different GEMs or segments, and currents through the gas gap between two GEMs, which occur after a primary discharge [48].

Since the absolute voltages of the (not discharged) GEMs closer to the drift electrode fall to lower absolute voltages, the GEM facing the drift volume now has a lower absolute voltage than before. Local drift field distortions occur, which might also affect the trajectories of particles in the neighbouring segments or stacks. The change of several electric fields in the GEM stack alter the performance and the IBF of it. Without a correction of the drift field distortions, the different gain and IBF, no useful data can be produced by a stack that is affected by a secondary discharge.

If only a primary discharge occurs, the slight increase of the affected GEM bottom potential causes small changes of one electric field and of the absolute voltages of the non-discharged segments, including GEMs which are higher in the stack. It has to be tested if this slight change has a significant effect on the data taking, and if capacitive coupling to other segments or GEMs induce further distortions. If this is not the case, only the small area of one segment of the stack cannot produce useful

⁸This phenomenon could be a result of the electrode, which faces the discharging gas gap, quickly changing its potential. As a result, ΔU_{GEM} increases fast, which leads to overvoltage across the GEM and ultimately to a discharge. Alternatively, the mechanism that causes the secondary discharge might also lead to an increase of the charge density or electric field in the GEM hole, which causes it to discharge.

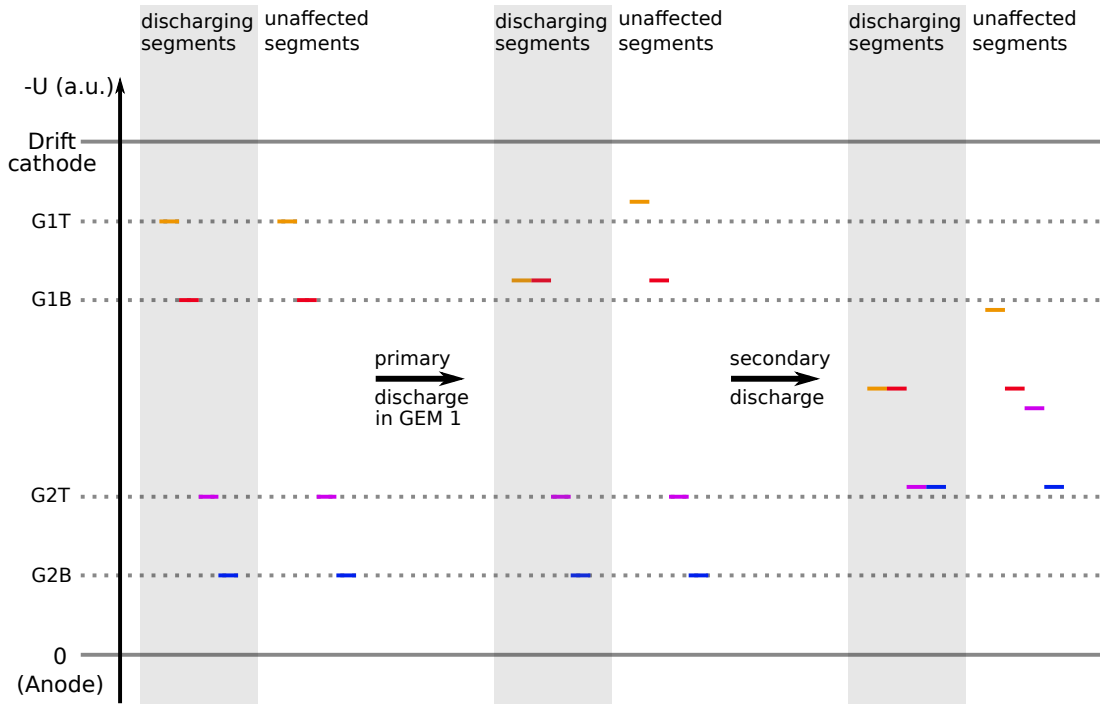


Figure 4.8: Sketch of the (negative) voltages U in a double-GEM setup, which is biased with a cascaded power supply and $R_D > 0\Omega$, in case of no discharge (left), after a primary discharge in GEM 1 (middle) and after a secondary discharge between the two GEMs (right). The GEM top potentials which are not directly affected by the discharge are also shown (*unaffected segments*). The relative positions of the potentials after a discharge can differ in reality, where capacitive couplings or currents after the primary through the gas have to be considered. The figure is not to scale. The following colour code is used for the different potentials: GEM 1 top (G1T, orange), GEM 1 bottom (G1B, red), GEM 2 top (G2T, purple), GEM 2 bottom (G2B, blue). Dotted lines represent the nominal voltages of each GEM electrode.

data.

Dedicated studies of the discharge rate with a prototype of an IROC, with the design as described in Sec. 3.3, have been conducted at CERN's *Super Proton Synchrotron*, where the chamber was placed in hadron showers caused by high-intensity pion beams impinging on an iron absorber. During the beam-time, a discharge rate of $(6.4 \pm 3.7) \times 10^{-12}$ per incoming hadron was measured [35]. During a full month of lead-lead collisions at 50 kHz in LHC Run 3, about 5×10^{13} particles are expected to cross the readout planes of the TPC. Including a factor of 2 for background events, about 7×10^{11} particles cross each of the 144 GEM stacks during a full lead-lead run [35]. Hence, between 2 and 8 discharges per GEM stack per month of heavy-ion data taking are expected. Assuming a recovery time of 100 ms from a discharge and 8 discharges per GEM stack in a full month, only about 2 min of the running time are affected.

However, the ion backflow of a GEM stack is defined by its gain and electrical fields. As discussed above, the voltages of GEMs, as well as the electric fields, can be altered after a (secondary) discharge. Since the tracking of the upgraded ALICE TPC will rely on dynamic space-charge maps that are created during data taking (see 3.3.1), the track reconstruction algorithm has to account for the different IBF in a recovering stack. Drift field distortions in front of the affected stack have to be considered too. If these effects cannot be corrected, one has to wait until the ion density in the drift volume has recovered. This takes at least as long as the maximum drift time of ions over the full drift length of the TPC (2.5 m). At a drift field of 400 V cm^{-1} in Ne-CO₂-N₂ (90-10-5), this takes about 210 ms [36]. Combining the ion drift with the recovery time (~ 100 ms), about 6 min of the data taking time is affected.

A more considerable loss of data is to be expected if the power supply of a GEM stack cannot sustain the currents during a discharge and trips. In this case, the cascaded power supply will need a considerably higher time to safely bring the GEMs back to their nominal voltages. The data loss in this scenario can be of the order of a few percent. In order to keep the data loss at a minimum, the tracking algorithm needs to be able to exclude the area of the tripped stack, and possibly also the neighbouring stacks, which are affected by the drift-field distortions. If no corrections can be applied, the side of the TPC which is affected by the discharge cannot record data until the GEM voltages and the space-charge density in the drift volume have recovered.

Damages by secondary discharges

Since the large, unsegmented GEM bottom electrodes in the ROCs of the future ALICE TPC are involved in a secondary discharge, a large amount of energy will be released during the discharge, which could lead to permanent damage of the GEMs. Furthermore, secondary discharges in the induction gap are associated with large currents in the anode plane. Thus, the readout electronics need to be protected against the discharges. Voltages induced in the pads of the readout, due to primary

discharges in GEMs or from secondary discharges in the transfer gap, are small and consequently do not endanger the electronics.

Once the new readout chambers are installed in the TPC, they will be used for LHC Run 3 and Run 4. No repairs are possible during that time, which means the chambers are in use until 2029. Therefore, minimizing the risk of (secondary) discharges is crucial to ensure a successful operation of the detector.

In order to avoid secondary discharges, the voltages should be chosen such that the electric fields stay below the secondary discharge onset field. In a transfer field between two GEMs, the electric field strength is defined by the potential difference between the GEM bottom potential of the upper GEM and the GEM top potential of the lower GEM. Since a primary discharge in a GEM induces a drop of the top potential to its bottom potential, the real transfer field after a primary discharge is higher by approximately $\Delta U_{GEM}/d$, where d corresponds to the gap length between two GEMs. Therefore, when choosing the GEM voltages and electric fields, one has to consider the field $E = E_T + \Delta U_{GEM}/d$ after a primary discharge.

The onset field in the induction gap of a single-GEM detector, using Ne-CO₂-N₂ (90-10-5) with the high-voltage scheme of the ALICE readout chambers, has been measured to be about 5.7 kV cm^{-1} [54]. The highest applied fields in the ROC's of the upgraded TPC are 4 kV cm^{-1} . The highest electric field in the ALICE TPC are reached when a discharge occurs in GEM 3, which has a voltage of $\Delta U_{GEM3} = 288 \text{ V}$. Hence, the transfer field T2 increases to approximately 5.4 kV cm^{-1} after a primary discharge, which is only slightly below the measured onset field. Therefore, it cannot be excluded that secondary discharges occur during the operation of the upgraded ALICE TPC. Understanding the mechanism behind secondary discharges is an important step towards a safer operation of GEM-based detectors and might yield more possibilities to mitigate them.

5 Secondary discharge studies

The phenomenon of secondary discharges was already introduced in Section 4.3. In this chapter, research is presented which aims at further characterizing the secondary discharge. A setup, which is described in Sec. 5.1, with a single GEM is used in order to exclude additional effects that occur in multi-GEM structures. The methodology of inducing and measuring discharges is explained in Section 5.2. During all measurements, the anode signal and the GEM potentials are recorded, which can be used to deduce quantities such as the secondary discharge probability and time between primary and secondary discharge (Sec. 5.3), and to compare the potential evolution of the GEMs after discharges in different biasing schemes, gas mixtures or high voltage settings.

In Section 5.5, the dependence of secondary discharges on the drift field is investigated. Measurements with no or reversed drift field allow to draw conclusions on the role of the GEM top electrode during the secondary discharge. A custom-made GEM with aluminium electrodes is employed in Section 5.6 in order to study the importance of the GEM material. Secondary discharges are measured with a reversed induction field in Sec. 5.7. In Section 5.8, the mitigating effect of decoupling resistors on secondary discharges is linked to the potential evolution of the GEM after a primary discharge. As part of a larger research effort, the secondary discharge probability is measured for Ar-CO₂ gas mixtures with varying concentration and for Ne-CO₂-N₂ (90-10-5) in Sec. 5.9. Continued investigation by our collaborators (Sec. 5.9.2) lead to a proposal of the mechanism responsible for secondary discharges, which is discussed in Section 5.9.3. The high-voltage settings and relevant data for all measurements in this thesis can be found in Appendix B. Distributions of the time between primary and secondary discharge are shown in Appx. C.

5.1 Setup

For the measurements presented in this chapter, a small detector employing one gas electron multiplier foil of $10 \times 10 \text{ cm}^2$ size, as sketched in Fig. 5.1, is used. A copper GEM of standard design and a single-mask aluminium GEM (see also Sec. 5.6) are employed. Figure 5.2 shows a photograph of the opened setup. The GEM is enclosed by the gas-tight detector volume, which is flushed with Ar-CO₂ (90-10) at 10 L/h for most measurements. In dedicated measurements of the influence of the gas mixture on secondary discharges, Ar-CO₂ in different ratios or Ne-CO₂-N₂ (90-10-5) at 10.5 L/h is used. A sensor in the gas exhaust line measures the relative water content. The GEM sits on top of a strip readout anode, where the foil is separated from the anode by a 2 mm thick glass-fibre frame. A mesh 28 mm above

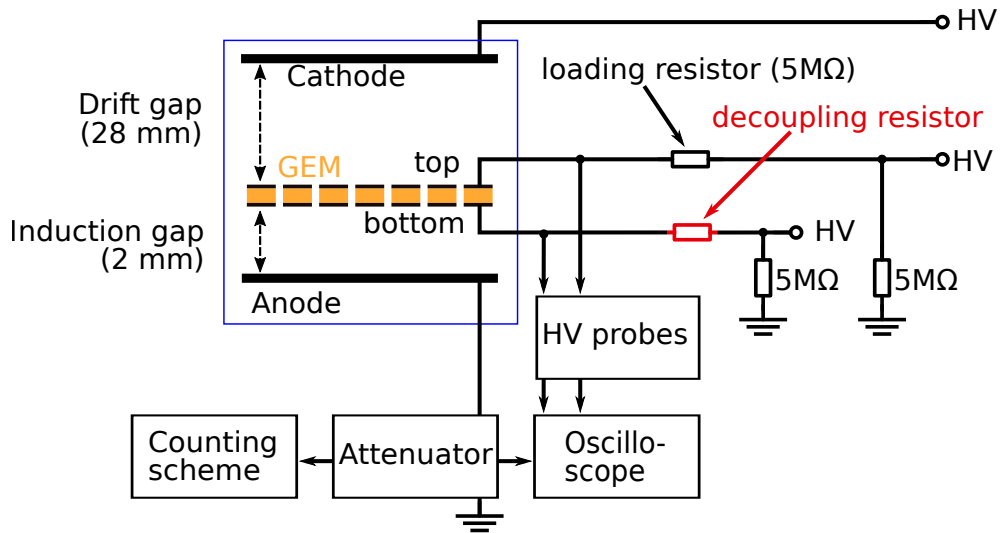


Figure 5.1: Schematic view of the setup used for the measurements in this thesis. A GEM is placed between a grounded anode and a cathode mesh in an enclosed detector volume (blue). A highly ionizing source triggers discharges in the GEM when a sufficient voltage is applied. Discharges induce signals in the anode plane, which are counted with NIM modules (Sec. 5.1.2). Two high voltage (HV) probes read the potential at the GEM electrodes. An oscilloscope stores the signals of the anode and the GEM potentials when a discharge occurs. The decoupling resistor is optional.

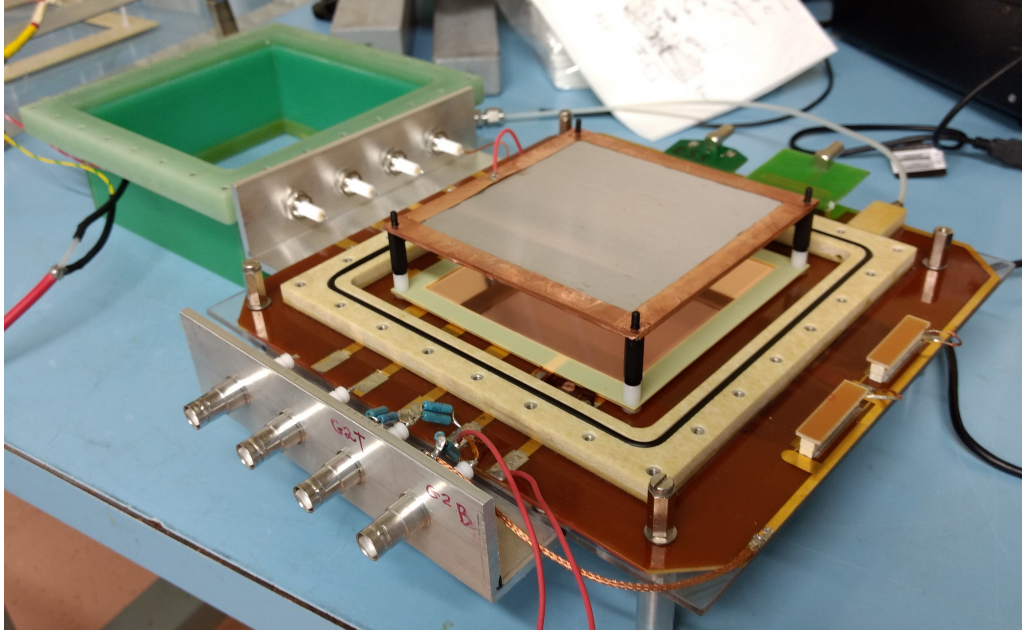


Figure 5.2: Photograph of the opened detector. The cathode mesh is kept at a distance of 28 mm to the GEM by black and white spacers. Additional screws on top of the cathode are not depicted. The glass-fibre GEM frame ensures a distance of 2 mm from the anode. The green box in the top left corner is screwed on top of the detector to guarantee gas tightness. The (disconnected) HV path to the GEM can be seen in the front, with the resistors to ground and to GEM top. The red wires connect to the high voltage probes.

the GEM foil serves as cathode, which allows particles drift through it. The electric field defined by the cathode (anode) and the GEM top (bottom) electrode is referred to as *drift field* E_{Drift} (*induction field* E_{Ind}).

To power the GEM electrodes and the cathode, a CAEN N470 [55] power supply with 4 independent channels and a CAEN N471 [56] power supply are employed, respectively. The power supplies are operated with a current limit that is set at a few 100 μA above the expected currents. If the current limit is reached during a discharge, the voltage is slowly ramped down, so that the current is kept at the chosen limit. Consequently, the power supplies do not trip during a short-lived discharge in the GEM. In case of a primary discharge, the GEM top potential drops towards the bottom potential. A 5 M Ω *loading resistor* (R_L) between the GEM top electrode and the PS causes the ΔU_{GEM} to recover on a time scale of 100 ms. The relatively large time at $\Delta U_{GEM} \approx 0\text{V}$ quenches the spark. In the bottom HV path, an optional *decoupling resistor* (R_D) can be employed. In order to sink excess currents during discharges, a path to ground with a 5 M Ω resistor is added to each high voltage supply path. The anode is grounded through the attenuator.

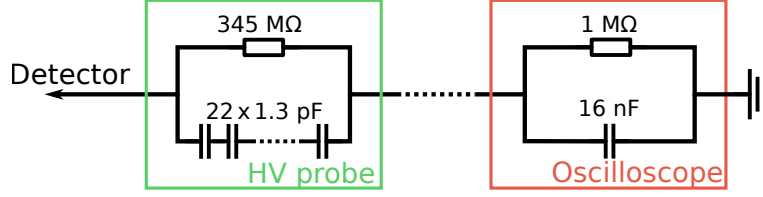


Figure 5.3: Electric circuit diagram of the high voltage probes. The impedance is approximately matched to the oscilloscope’s input impedance.

5.1.1 Readout

During a primary or secondary discharge, a signal is induced in the anode. The signal is read out by a Rohde & Schwarz RTE 1054 oscilloscope [57]. Two 12 dB t-type attenuators in series are employed to match the signal amplitude with the oscilloscope’s dynamical range. Additionally, the attenuated anode signal is used to count the number of primary and secondary discharges. A detailed description of the counting scheme is given in Sec. 5.1.2.

The GEM potentials are examined by two custom made high voltage probes (Fig. 5.3), each with a resistance of $\sim 345 \text{ M}\Omega$. This forms a voltage divider with the input resistance of the oscilloscope, allowing to measure the GEM potentials within the dynamic range of the oscilloscope ($\pm 10 \text{ V}$). For a proper signal transmission, the impedance of the HV probes is matched with the input impedance of the oscilloscope by connecting $22 \times 1.3 \text{ pF}$ capacitors in series. The resulting RC constants are $\sim 20 \text{ }\mu\text{s}$ for the probes and $\sim 24 \text{ }\mu\text{s}$ for the oscilloscope. However, the input capacitance is only an approximate value, and parasitic capacitances add to the capacitance of the probes. A photo of the HV probes can be seen in Figure 5.4.

In addition, the HV probes form a voltage divider with the loading and decoupling resistors, which creates a small voltage drop on the GEM electrode. The real voltage U_{real} on a GEM electrode relates to the voltage U_{set} set at the PS as

$$U_{real} = U_{set} \cdot \frac{R_{scope} + R_{probe}}{R_{L,D} + R_{scope} + R_{probe}}, \quad (5.1)$$

where $R_{scope} = 1 \text{ M}\Omega$ is the input resistance of the oscilloscope, $R_{probe} = 345 \text{ M}\Omega$ is the resistance of the HV probes and $R_{L,D}$ refer to the loading or decoupling resistor. Since the decoupling resistors used in our measurements are $50 \text{ k}\Omega$ and $100 \text{ k}\Omega$, the voltage correction on GEM bottom can be neglected. If not otherwise mentioned, ΔU_{GEM} usually means the real, corrected voltage across the GEM.

5.1.2 Counting of discharges

In order to count the number of primary (N_{prim}) and secondary discharges (N_{sec}), a series of NIM modules are employed. Two different methods were used. The first is based on the amplitude of the induced signal in the anode, whereas the second

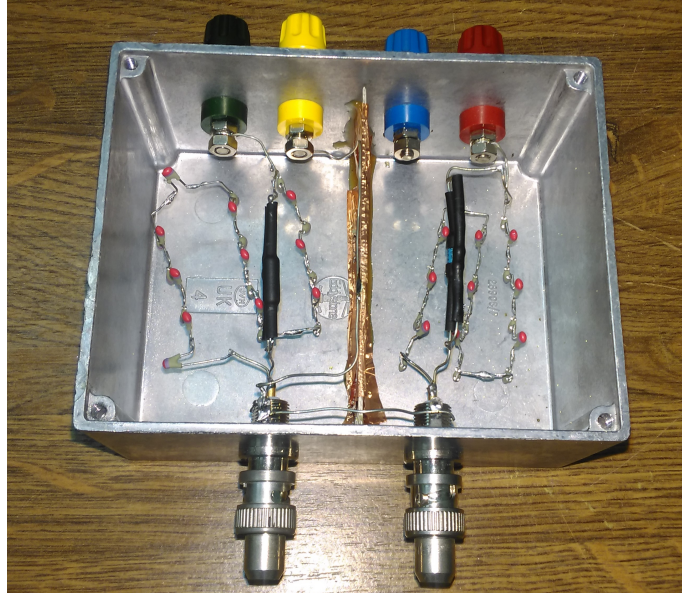


Figure 5.4: Photograph of the high voltage probes. Wires are added to improve the grounding. A Copper foil between the two probes guarantees proper shielding between them.

exploits that secondary discharges only occur up to $100\ \mu\text{s}$ after a primary discharge. The dead time of the counting logics is negligible compared to the low primary discharge rate, which is of the order of $0.1\ \text{s}^{-1}$.

Sometimes after a secondary discharge, it reignites (cf. Sec. 4.3), which causes another potential drop of the GEM potentials before they have fully recovered. This is visible as another signal in the anode. The different counting mechanisms do not accept any new signals for about $100\ \mu\text{s}$ after the secondary discharge, which effectively blocks additional potential drops from the reignition. Therefore N_{sec} corresponds to the number of events that include a secondary discharge, not to the amount of times the GEM potentials drop to the anode potential.

Counting by amplitude discrimination

The first logic employs the fact that in a biasing scheme without decoupling resistor, the secondary discharge induces a much larger signal in the anode than the primary discharge (Fig. 4.6a). A flow chart of the counting scheme and the signal outputs corresponding to each step is shown in Figure 5.5.

The attenuated signal from the anode is split in two by a Fan-in/Fan-out unit (FIFO). They are then fed into separate discriminators. The discriminator to count the primary discharges has a threshold that is lower than the peak height of a primary discharge, but higher than the noise that can be induced by the electronics or external radiation, whereas the threshold for secondary discharges is significantly higher than the maximum amplitude of a primary discharge. When the threshold

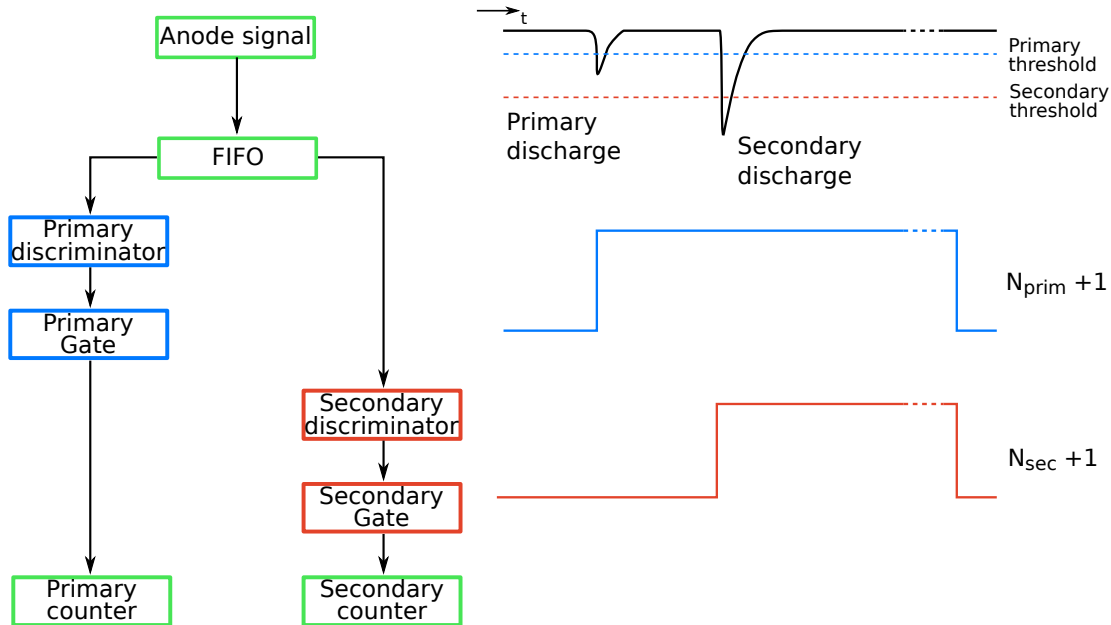


Figure 5.5: Flowchart (left) of the counting logic that distinguishes between primary and secondary discharge by their signal height in the anode. The signal output of the respective stages is sketched on the right. Oscillation in the anode signal during the discharges are not displayed.

of a discriminator is passed, it sets a logic signal, which is then stretched by a gate to about $100\ \mu\text{s}$ and counted by a scaler. This time is significantly longer than the maximum time that was observed between primary and secondary discharge. During this time, no other signal is accepted by the gates. Therefore, double counting of the primary discharge is avoided, since the signal from the secondary discharge, which also passes the primary threshold, does not trigger another response of the gate, and therefore also of the counter. Similarly, the secondary gate blocks signals from reigniting secondary discharges.

Counting by time discrimination

The second counting logic (Fig. 5.6) employs the fact that a secondary discharge only occurs after a primary discharge has already happened. Its advantage is that it is not dependent on the amplitude difference. When a decoupling resistor is used to bias the setup, the signal heights of primary and secondary discharge approach each other, which renders the amplitude discrimination unreliable.

The attenuated anode signal is split by a FIFO module and passed to two discriminators, which now have a similar threshold above the noise level. The output of the discriminators is then stretched by a gate to about $50\text{--}100\ \text{ns}$. This serves as a way to prevent the strong oscillatory noise, which overlays the anode signal during discharges (cf. Fig. 4.6a), to trigger the discriminator again. At the end of

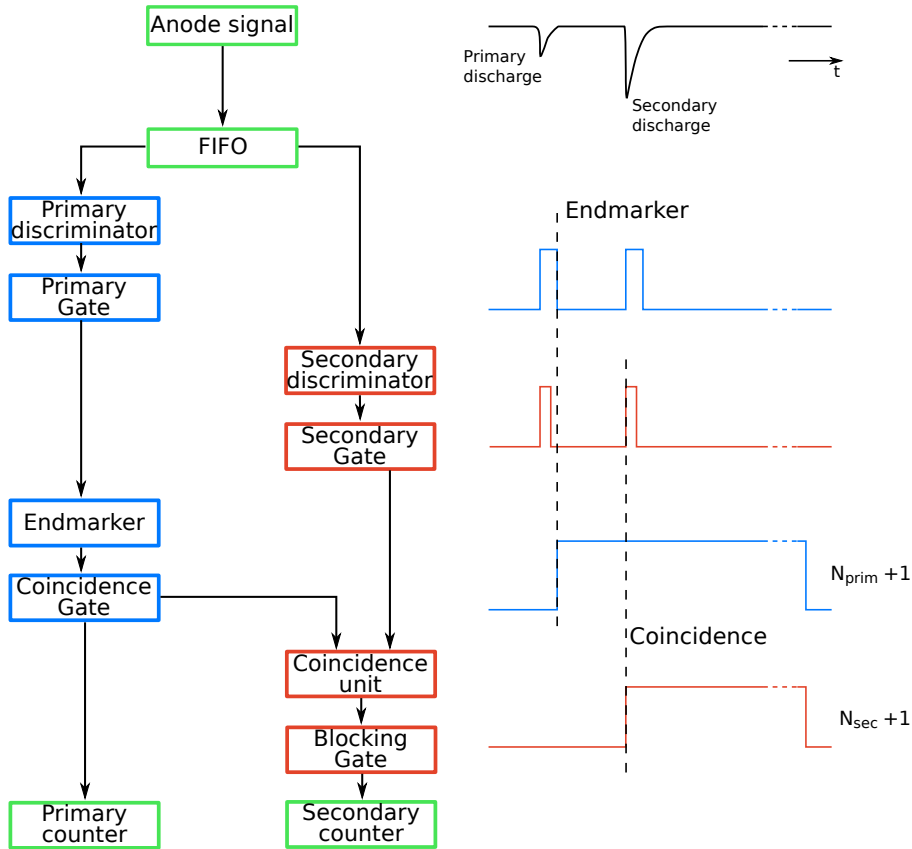


Figure 5.6: Flowchart (left) of the counting logic that distinguishes between primary and secondary discharge by their time difference. The occurrence of a primary discharge is a precondition for the secondary discharge, which is realized by a coincidence unit. The signal output of the respective stages is sketched on the right. Oscillation in the anode signal during the discharges are not displayed.

the signal of the primary discriminator, another logic signal (endmarker) is produced, which is prolonged by the *coincidence gate* to about $100\ \mu\text{s}$ and is used as input for a coincidence unit. This time serves as an acceptance window for secondary discharges, but is also used to count the number of primary discharges. When a secondary discharge occurs in this time frame, it is passed through the secondary discriminator into the coincidence unit, which then produces a logic signal. If the secondary gate would be as long as or even longer than the primary gate, it would immediately trigger the coincidence unit. Therefore, it is chosen to be slightly shorter. The output of the coincidence unit is again stretched to $\sim 100\ \mu\text{s}$ in order to block further signals (reignitions) and to prevent double counting. The signal is also used to count the number of secondary discharges. The width of the primary and secondary gate are chosen such that they cover the whole width of the primary discharge, which prevents that oscillations in the primary discharge signal trigger a second logic signal

that falls into the acceptance window, resulting in a single primary discharge counted as primary and secondary discharge.

5.2 Methods

5.2.1 Inducing discharges

Under normal conditions, discharges in a GEM are extremely rare. As a result, the quantitative measurement of the GEM's behaviour under discharges is not feasible without purposefully inducing discharges. In this study, a combination of high voltage $\Delta U_{GEM} \sim 400$ V across the GEM combined with a highly ionising radon (Rn) source is used to trigger discharges in the GEM.

Before the gas enters the detector, it flows through a container that holds traces of ^{230}Th , which decays via ^{226}Ra to ^{222}Rn . These isotopes have a half-life time of 75 380 yr, 1602 yr and 3.83 d, respectively. Therefore, the most frequent decay in the setup is ^{222}Rn decaying via emission of an alpha particle with an energy of $E_{\alpha\text{Rn}} = 6.4$ MeV. In order to produce one electron-ion pair through ionization in Ar (CO_2), an energy transfer of $W_{\text{Ar}} = 26\text{--}27$ eV ($W_{\text{CO}_2} = 34\text{--}35$ eV) is required [58]. This yields

$$N_{\alpha} = \frac{E_{\alpha\text{Rn}}}{W_{\text{Ar-CO}_2}^{90-10}} = \frac{6.4 \text{ MeV}}{27.3 \text{ eV}} = 234 \cdot 10^3 \quad (5.2)$$

electron-ion pairs on average.

The distribution of the energy loss as a function of the distance travelled in the gas is described by the *Bragg curve*. Most of the energy loss of alpha particles is expected when the particle is close to being stopped. The increase of the energy loss in this regime is also called the *Bragg peak*. A simulation of the Bragg curve for ^{222}Rn decays in various argon and neon based gas mixtures is shown in Fig. 5.7. The maximum distance of an alpha particle in Ar- CO_2 (90-10) is about 5.6 cm, whereas it is almost 8 cm in Ne- CO_2 - N_2 (90-10-5) and has a much wider Bragg peak.

In order to reach the critical charge density in a GEM hole at a gain of about 500, only the area around the Bragg peak can provide enough electrons. Measurements by P. Gasik et al. [44] confirm that the discharge probability rises by several orders of magnitude when the alpha source is placed at a distance to the GEM that corresponds to the Bragg peak.

In this work, radon is added to the gas, so that a uniform distribution of alpha decays with no preferred direction in the detector volume is achieved. Therefore, the whole detector is exposed to the radiation. By having a much larger volume in the drift field compared to the induction field, most alpha decays occur above the GEM, where the electrons from the ionisation are guided towards the GEM top.

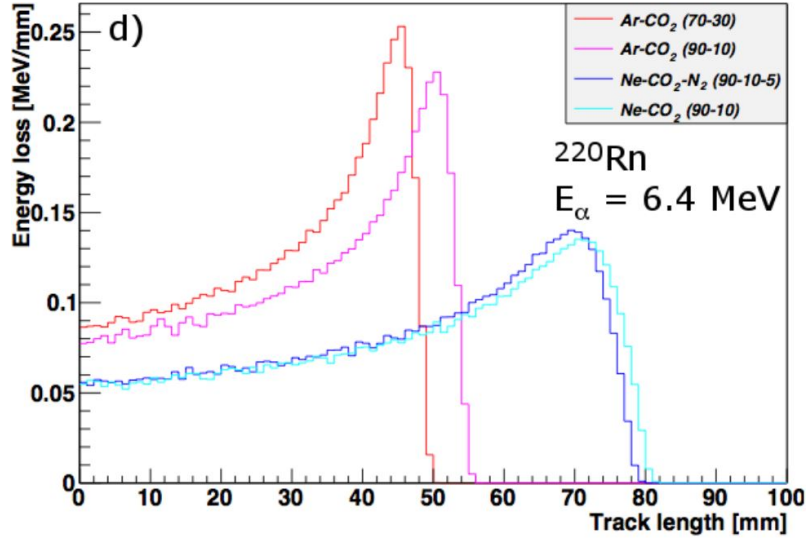


Figure 5.7: Simulation of the energy loss of alpha particles with energy $E_{\alpha\text{Rn}} = 6.4 \text{ MeV}$ as a function of the track length [35]. In argon based gas mixtures, the Bragg peak is more pronounced.

5.2.2 Measurement procedure

This study examines the characteristics of discharges in the detector. In addition to a highly ionizing radiation source (Sec. 5.2.1), a high voltage ΔU_{GEM} across the GEM is needed to produce discharges at a reasonable rate. The value of the potential difference needed to trigger discharges depends primarily on the GEM geometry and the gas mixture. When a new gas mixture is introduced, the detector volume has to be flushed with the gas mixture first. At a gas flow of 10 L/h, less than one hour is needed to exchange the gas in the chamber several times.

Then, ΔU_{GEM} is first set to a safe voltage (200–300 V), which is slowly increased until a value is found where the primary discharge rate is about $0.1\text{--}0.3 \text{ s}^{-1}$. When a satisfactory voltage for one setup is found, measurement series with varying electric fields can be performed where ΔU_{GEM} is kept approximately constant. Sometimes adjustments of a few volts between measurements are necessary to increase or lower the primary discharge rate again, which is influenced by ambient conditions like the atmospheric pressure.

When starting a new measurement, the voltages of both GEM electrodes are ramped up with a constant rate of 20 V s^{-1} . Hence, no voltage difference across the GEM is present during the initial ramping process. This is important since the real voltage across the GEM is different from the set voltage due to the voltage divider, which is formed with the HV probes (Eq. 5.1). Because the voltage drop is dependent on the absolute voltages, ramping the potentials up or down with a large ΔU_{GEM}^{set} can cause unexpected high ΔU_{GEM}^{real} that might lead to damage to the GEM.

The usage of individual channel power supplies does not allow to change all potentials simultaneously during operation. As a consequence, each potential has to

be changed sequentially between two measurements. In order to avoid destructively large ΔU_{GEM} , the order of potential changes has to be chosen such that ΔU_{GEM} decreases during the transition to the next measurement. For example, when increasing the induction field while keeping all other voltage differences constant, the GEM bottom potential is increased first, which decreases ΔU_{GEM} temporarily, then GEM top is increased, then the cathode. When decreasing the induction field, the order is reversed.

If not otherwise mentioned, the measurements are conducted in Ar-CO₂ (90-10) without decoupling resistor and a drift field of $E_{Drift} \approx 400 \text{ V cm}^{-1}$. For every measurement, the voltage settings, room temperature, atmospheric pressure and relative H₂O content in the gas are documented (Appx. B). One of the two counting logics determines how many primary and secondary discharges occurred during the measurement time. In addition, an oscilloscope records and saves the potentials of the GEM and the anode signal during a discharge, so that they can be analysed afterwards. Since the drift velocity and energy loss of charge carriers in a gas depend on the density of the medium, the induction field is normalised by the gas pressure when comparing different measurements.

5.2.3 Conditioning of GEMs

Charges that are produced in an electron avalanche can accumulate in the insulator of a GEM, which leads to a modification of the electric field in the GEM hole [59]. Therefore, the effective gain changes during the charging up of the polyimide layer. Since the measurements in this study put the GEM into extreme conditions close to its breakdown, this uncontrolled variation of the electric field should be avoided in order to prevent damage and to have stable and reliable results. Therefore, every (new) GEM has to be “conditioned” after placing it in the detector. This conditioning procedure is described in the following paragraphs.

Before the GEM is used at voltages where discharges occur, the voltage across the GEM is increased every few minutes in small steps until a ΔU_{GEM} is reached which is 20–30 V lower than the discharge regime. The detector is then operated at this voltage for a few hours, before going to voltages where discharges occur frequently. Then, the induction field is increased every 10 to 15 minutes by about 500 V cm^{-1} until a field similar to that in the desired measurements is reached ($\sim 4500 \text{ V cm}^{-1}$ in Ar-CO₂ (90-10)). After this procedure, the GEM can usually experience discharges without fatal damage.

When a newly produced GEM is introduced to the detector, it is even more important to condition the GEM, since sharp metal edges or defects from the production could enhance the electric field locally. When the voltage is slowly increased, as described above, holes with strong electric fields due to defects can discharge at moderate fields, which melts the defect away. If a high voltage is applied immediately, the electric field created by production inaccuracies might cause strong discharges that destroy the GEM.

5.2.4 Permanent short circuits in GEMs and recovery

In this study, several thousands of discharges⁹ could be recorded with a GEM before it developed a *weak spot*, i.e. a small area that discharges at lower voltages than the rest of the GEM, or a short circuit between the top and bottom side. Sometimes, the GEM can be recovered from these states. For this, the GEM has to be disconnected from the setup and all resistors or connections to ground have to be removed from the GEM. Then, a high voltage, usually 500–600 V in air, is directly applied to the GEM, which might burn away the defect. In general, this can also be done in other gas mixtures, if the voltage is adjusted accordingly. However, this procedure is not always successful, and might lead to a worse performance, for example a higher leakage current of the GEM (cf. Sec. 5.4).

5.3 Definition of measurement variables and uncertainties

In the measurements presented in the following sections, mainly the secondary discharge probability and the time between primary and secondary discharge as a function of the induction field E_{Ind} are investigated quantitatively. These variables and their uncertainties are introduced here. Since properties of the gas, such as the gain or the drift velocity, depend on the (atmospheric) gas pressure, the secondary discharge probability and the time between primary and secondary discharge is presented as a function of E_{Ind}/p .

5.3.1 Secondary discharge probability

The occurrence of a secondary discharge after a primary discharge is a binary event. Therefore, the probability to observe N_{sec} secondary discharges given N_{prim} primary discharges can be described by a binomial distribution

$$p(N_{sec}|N_{prim}, \hat{P}_2) = \frac{N_{prim}!}{N_{sec}!(N_{prim} - N_{sec})!} \hat{P}_2^{N_{sec}} (1 - \hat{P}_2)^{N_{prim} - N_{sec}}, \quad (5.3)$$

where \hat{P}_2 is the true secondary discharge probability. However, \hat{P}_2 is the variable of interest and needs to be experimentally measured.

One can estimate the value of the true secondary discharge probability via the principle of maximum likelihood as

$$P_2 = E(\hat{P}_2) = \frac{N_{sec}}{N_{prim}}, \quad (5.4)$$

which corresponds to the experimentally determined ratio of secondary discharges to primary discharges [60]. The electric field for which $P_2 = 0.5$ is called the (*secondary discharge*) *onset field* E^{On} .

⁹About 50% of the discharge events include a secondary discharge.

The variance of the binomial distribution of Eq. 5.3 is given as

$$V(N_{sec}) = N_{prim} \cdot \hat{P}_2(1 - \hat{P}_2). \quad (5.5)$$

By using the estimator $P_2 = N_{sec}/N_{prim}$, we can obtain the variance V of the measured secondary probability:

$$V(P_2) = \sigma_{P_2}^2 = V\left(\frac{N_{sec}}{N_{prim}}\right) = \frac{V(N_{sec})}{N_{prim}^2} = \frac{P_2(1 - P_2)}{N_{prim}}, \quad (5.6)$$

where σ_{P_2} is the standard deviation of the measured secondary discharge probability.

However, using the estimator of Eq. 5.4 clearly yields unphysical values of σ_{P_2} in the limiting cases $N_{sec} = 0$ or $N_{sec} = N_{prim}$. One could try to infer the true probability \hat{P}_2 , instead of using the estimator P_2 , by using the Bayesian theorem and the measured values for N_{prim} , N_{sec} [61]. This treatment yields corrections to the binomial error propagation especially in the limiting cases of high or low probability, and when only a small number of events are available. It also yields realistic, finite uncertainties in all cases. However, it is quite complicated. At intermediate probabilities, the binomial and Bayesian method give similar results. Considering that more than 100 discharge events are recorded for the majority of the following measurements, and that the region of interest is $0.1 < P_2 < 0.9$ —where the binomial error propagation yields reliable results—equation 5.4 and 5.6 are used for the secondary discharge probability and its standard deviation, respectively.

No systematic uncertainties are assigned to N_{prim} , since the counting works reliably for all primary discharges. Concerning N_{sec} , there is one condition which required a further check in order to ensure the correctness of the counting. At large induction fields, where $P_2 \approx 1$, secondary discharges are observed as fast as ~ 200 ns after the initial discharge. By analysing the waveforms, which were recorded by the oscilloscope, digitally, one can determine the secondary discharge probability with a resolution of a few 10 ns. However, the analysis of thousands of waveforms is computationally demanding and slow. Therefore, the secondary probability measured by employing NIM modules (counter) and by analysing recorded waveforms digitally (waveform) is compared for only one measurement (Fig. 5.8). Note that the number of saved waveforms does not correspond to the number of events counted by the NIM module, since the oscilloscope has a relatively long saving time. The two methods are in good agreement with each other, even at the highest measured induction fields. This implies that even if a few secondary discharges are not detected by the NIM modules, the amount is negligible compared to the statistical uncertainty. Therefore, the counting logic is used for all measurements and no correction for the detection efficiency of N_{sec} is applied.

5.3.2 Time between primary and secondary discharge

In order to determine the time between a primary and the following secondary discharge, the waveforms recorded by the oscilloscope are analysed. A ROOT [62]

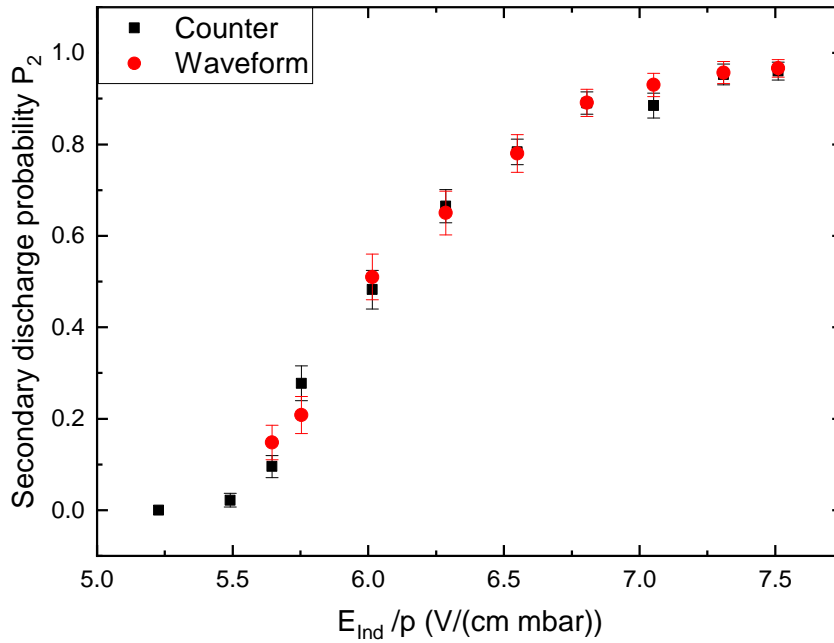


Figure 5.8: Secondary discharge probability P_2 obtained by using the counters presented in Sec. 5.1.2 and by analysing the waveforms recorded by an oscilloscope. The two methods are in good agreement with each other. The measurement was done in Ar-CO₂ (90-10) with an aluminium GEM. Details of the measurement can be found in Sec. 5.6.

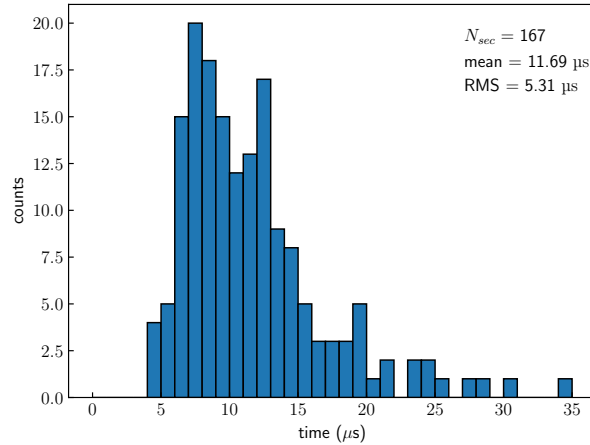


Figure 5.9: Distribution of the time between primary and secondary discharge in Ar-CO₂ (90-10) at $E_{Ind} = 5.25 \text{ kV cm}^{-1}$. No decoupling resistor is used. The distribution shows a pronounced tail towards larger times.

macro reads the GEM top signal and scans the amplitude for rapid changes. As can be seen in Fig. 4.6a, a voltage drop of about 400 V during the primary discharge in the GEM corresponds to about 1 V in the HV probe signal, which is recorded by the oscilloscope. During a secondary discharge, the amplitude of the voltage drop depends on the induction field strength, but is usually larger than 1 V. The time of the first potential drop, which is larger than 0.5 V (in the oscilloscope's units), is saved as the time of the primary discharge t_{prim} . Afterwards, the macro searches for larger potential drops of 1–1.5 V at times $t > t_{prim}$. The amplitude for the voltage drop of the secondary discharge is optimized for each change in the setup to guarantee a correct determination of the time of the secondary discharge t_{sec} .

The times t_{prim}, t_{sec} are saved for every single event. As the distributions of the time between primary and secondary discharge t_2 show a pronounced tail towards larger times (e.g. Fig. 5.9), the mean value of the time differences does not perform well as an estimator of the most probable time. Furthermore, the large times of the tail of the distribution lead to an overestimation of the uncertainty when using common estimators, such as the root mean square (RMS), which is defined here as

$$\sigma(t_2) = \sqrt{\frac{1}{N_{sec}} \sum_{i=1}^{N_{sec}} (\langle t_2 \rangle - t_{2,i})^2}, \quad (5.7)$$

with $t_{2,i}$ being the time difference of single events and $\langle t_2 \rangle$ being the average time.

For the study of the origin of secondary discharges, the minimum and maximum times of the secondary discharge or the shape of the distribution might yield important information on the production process. In order to easily compare different distributions, the time between primary and secondary discharge is presented as a

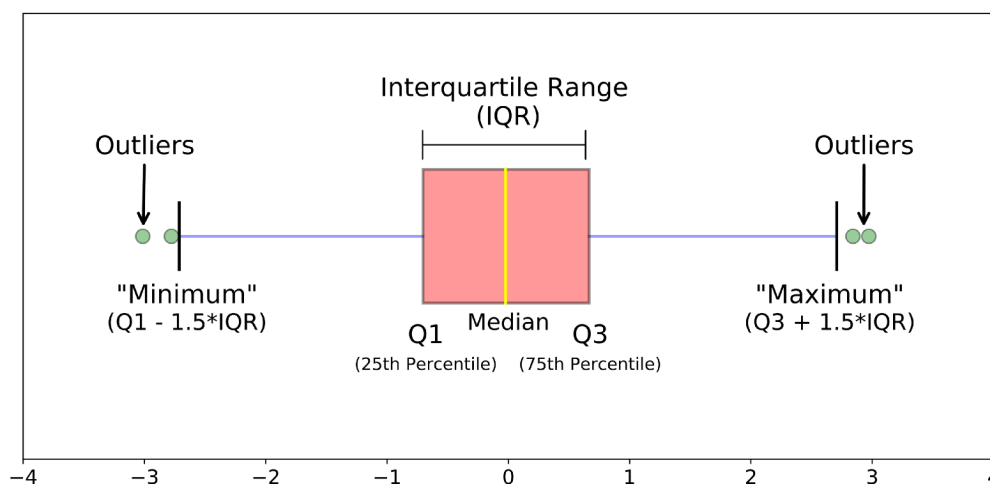


Figure 5.10: Example of a box plot. The median is represented by a yellow line. A box marks the $\pm 25\%$ of data below and above the median. From the end of the box, whiskers (blue lines) extend to the lowest (highest) value, which is still in the range defined by $Q1 - 1.5 \cdot IQR$ ($Q3 + 1.5 \cdot IQR$). Data below (above) the minimum (maximum) are treated as outliers and plotted as points. The figure was taken from [63].

box plot. Figure 5.10 shows an example of a box plot. It is a tool to display the distribution of a data set based on five numbers:

- Median: the middle value of a dataset, which is sorted from lowest to highest number. It is represented by a line.
- First quartile ($Q1$): The middle value between the smallest data point and the median. It represents the 25th percentile.
- Third quartile ($Q3$): The middle value between the the median and largest data point. It represents the 75th percentile.
- Minimum: The minimum value of the distribution is chosen as $Q1 - 1.5 \cdot (Q3 - Q1)$.
- Maximum: The maximum value of the distribution is chosen as $Q3 + 1.5 \cdot (Q3 - Q1)$.

A box from the first to the third quartile, the so-called *interquartile range* (IQR), represents the 25% of data below and above the median. Two "whiskers" extend from $Q1$ ($Q3$) to the lowest (highest) value which is still in the range between $Q1$ and the minimum ($Q3$ and the maximum). Points outside of this range are treated as outliers and are displayed by points.

The advantage of box plots is that minimum and maximum values can be identified easily, while also getting an impression of the skewness, or asymmetry, of the



Figure 5.11: A dark, burnt spot that developed on a GEM during the recording of discharges in Ar-CO₂ (70-30). The area started to discharge rapidly at a potential difference across the GEM that was lower by about 30 V than usual. By using the method presented in Sec. 5.2.4, the GEM could be recovered. Afterwards, no (frequent) discharges occurred around the burnt area.

distribution. When operating or designing a detector, the minimum and maximum time can also be of interest. Furthermore, in the case of distributions with a heavy tail, the median gives a better estimate of the most probable value than the mean. Complementary to the box plots, all time distributions are also shown as histograms in Appendix C.

5.4 Exchanging and recovering GEMs

In [47], it has been observed that replacing a GEM with another GEM of the same type at the same position can lead to a difference of the secondary discharge onset field of almost 15%. Throughout the measurements presented in this thesis, two different standard GEMs have been employed, of which one had to be taken out and inserted again, and one had to be recovered from a damaged area (Fig. 5.11). This gives the opportunity to compare the effect these procedures have on the setup. With the limited number of GEMs and replacements, only a qualitative statement can be made. Figure 5.12 shows a comparison of the secondary discharge probability for different GEM configurations. The curves have been recorded in the following order:

1. **GEM A:** Used for the measurement with different drift fields (Sec. 5.5). The GEM was taken out and replaced with an aluminium GEM afterwards.
2. **GEM A, reinserted:** After finishing all measurements with the aluminium GEM, GEM A was placed in the detector again. A measurement in Ar-CO₂ (90-10) was conducted, but unfortunately the GEM broke down afterwards.

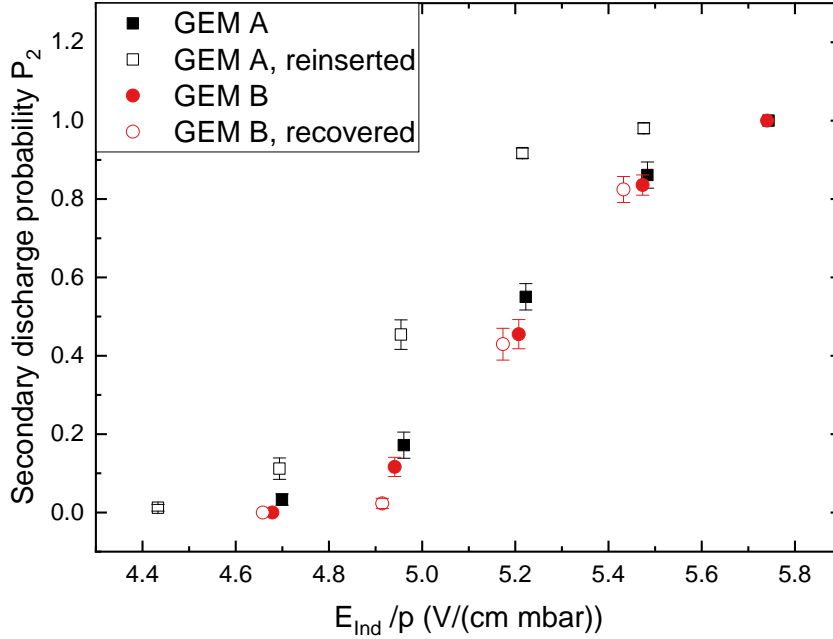


Figure 5.12: Secondary discharge probability P_2 as a function of E_{Ind}/p for different copper GEMs in Ar-CO₂ (90-10) with $R_D = 0$. GEM A has been used for the measurement of Sec. 5.5 (black square markers) and was then taken out of the detector. After reinserting it into the detector a few weeks later (hollow square markers), a shift of the onset by about 5% was seen. This is likely due to mechanical changes in the setup. GEM B (red circular markers) was used for the measurements in Section 5.9 and had to be recovered from damage at a later time (hollow circular markers). No significant shift of the onset is caused by the recovery method.

3. **GEM B:** A new GEM was placed in the detector.
4. **GEM B, recovered:** During a measurement in Ar-CO₂ (70-30), a burnt *weak spot* developed on the GEM, which caused discharges at ΔU_{GEM} in this area (Fig. 5.11). The GEM could be successfully recovered with the method mentioned in Sec. 5.2.4.

Differences of the secondary discharge onset field of about 5% are found for the same GEM before taking it out of the detector and after inserting it again (GEM A). This is likely explained by mechanical differences in the setup. If the position of a GEM is changed by only 200 μm , then E_{Ind} changes by 10%. Mechanical inaccuracies of this scale can be introduced during the assembly by uneven frames, differently tightened screws, etc. However, these mechanical changes are not accounted for in the calculation of E_{Ind} .

Recovering the GEM does not seem to have a significant influence on the secondary discharge probability. Nonetheless, an increase of the leakage current between the GEM electrodes from $\leq 1 \mu\text{A}$ to the order of $20 \mu\text{A}$ at $\Delta U_{GEM} = 400 \text{ V}$ in air was found.

5.5 Drift field dependence

Although charge carriers from the primary discharge crossing the gas gap can be excluded as sole reason of the secondary discharge, ions might play a significant role in its development. If the ions drift through the GEM hole, despite the absence of a (strong) electric field in the hole after the initial discharge, a fraction of them will hit the copper surface on the top side, where they will extract electrons from the material. These electrons may drift back through the hole and seed the secondary discharge. They might also explain the current through the gas gap.

To test this hypothesis, secondary discharges in the induction gap are investigated at different drift fields between 442 V cm^{-1} and -290 V cm^{-1} . Decreasing the drift field increases the collection efficiency of ions at the top electrode, which would lead to a stronger ion bombardment. Hence, more electrons would be created. Furthermore, electrons extracted from the top electrode in a reversed drift field drift towards the cathode instead of the GEM hole. If the mechanism described above is significant for the creation of a secondary discharge, a change of P_2 or of the time between primary and secondary discharge is expected for different drift fields.

5.5.1 Measuring with reversed drift field

When the drift field is decreased, the charge carriers in the detector volume are slower. Therefore, they are subject to stronger diffusion, which dilutes the ionisation electron clusters, therefore decreasing the likelihood of reaching the critical charge density for a primary discharge in a GEM hole. This results in a strong drop of the discharge rate with decreasing drift field. If the drift field is reversed, electrons drift towards the cathode instead of the GEM. Thus, only alpha particles that are stopped in the close vicinity of a GEM hole can lead to a discharge. At $E_{Drift} = -290 \text{ V cm}^{-1}$, on average only one primary discharge occurred every 23 minutes. It was not feasible to record data with high statistics for many induction field values. Therefore, only one point around $P_2 \sim 50\%$ and at low P_2 was recorded. The long measurement time (39 h) also meant that the measurement is subject to large atmospheric pressure fluctuations. Hence, the measurement was split into many measurement intervals of one to two hours, until a sufficient amount of statistics was reached. The number of primary and secondary discharges, the atmospheric pressure and other parameters were documented for every interval. A weighted mean of the atmospheric pressure is used to represent the data:

$$\bar{p} = \frac{\sum_{i=1}^m t_i \cdot p_i}{\sum_{i=1}^m t_i}, \quad (5.8)$$

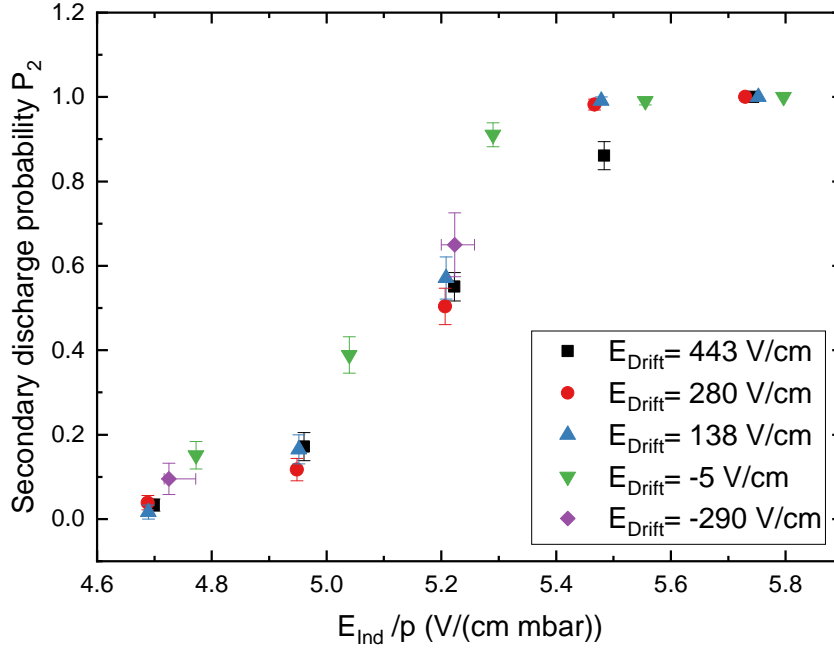


Figure 5.13: Secondary discharge probability P_2 as a function of E_{Ind}/p for different drift fields. Due to the small discharge rate with the inverted field $E_{Drift} = -290 \text{ V cm}^{-1}$, horizontal error bars are added to account for the atmospheric pressure fluctuations during the measurement time. A weighted mean is used to determine the position of the marker.

where $i \in \{1, \dots, m\}$ is the number of a measurement interval of duration t_i and p_i is the arithmetic mean of the pressure before and after each measurement interval. In addition, an uncertainty of E_{Ind}/\bar{p} for the inverted field is added, which corresponds to the maximum and minimum pressures that were recorded during the whole measurement time.

5.5.2 Results

No significant dependence of the secondary discharge probability in the induction gap on the drift field is observed (Fig. 5.13). A small shift at almost zero drift field ($E_{Drift} = -5 \text{ V/cm}$) is visible, which might indicate a slightly different behaviour of secondary discharges when no field is present above the GEM.

Unfortunately, only limited statistics ($N_{sec} \leq 50$) were obtained for the time measurements shown in Figure 5.14. For the collected data, no significant difference of t_2 for various drift fields can be seen.

Given that the variations of the drift field should lead to drastic changes in the ion collection at the GEM top electrode after a primary discharge, but no significant changes are visible in the secondary discharge probability or the time between primary

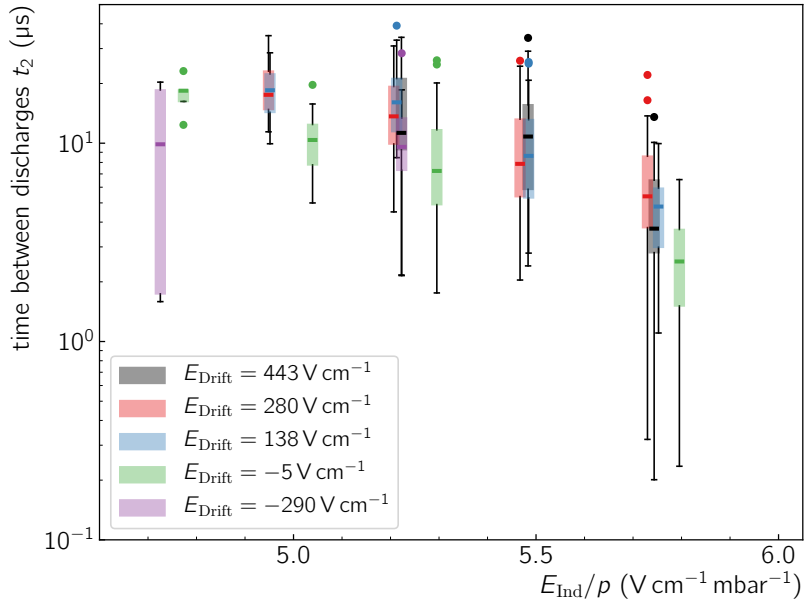


Figure 5.14: Average time between primary and secondary discharge as a function of E_{Ind} for different drift fields. The points correspond to those of Figure 5.13.

and secondary discharge, it can be concluded that the ion extraction from a GEM hole has no significant influence on the development of a secondary discharge in the induction gap. Hence, it is unlikely that ion bombardment of the top electrode causes secondary discharges.

5.6 Influence of the GEM material

After the primary discharge, an electric current through the induction gap is observed over several microseconds [48], while a glow on the GEM bottom electrode is present [51]. Furthermore, a long lasting glow after the secondary discharge can be observed on the electrode which serves as the cathode in the induction gap, i.e. if the electric field is inverted, a glow on the readout plane can be seen. Therefore an emission of electrons from the cathode material might feed the secondary discharges.

Relevant sources of electrons include thermionic emission from the GEM bottom electrode, which is already heated up by the primary discharge, and ion bombardment of the GEM material. In section 5.5, it was already found that ion bombardment of the GEM top electrode does not play a relevant role. However, a fraction of ions might hit the bottom electrode or insulating material, which in turn facilitates the heating of the GEM and can extract more electrons.

The amount of emitted electrons is related to the work function, which describes

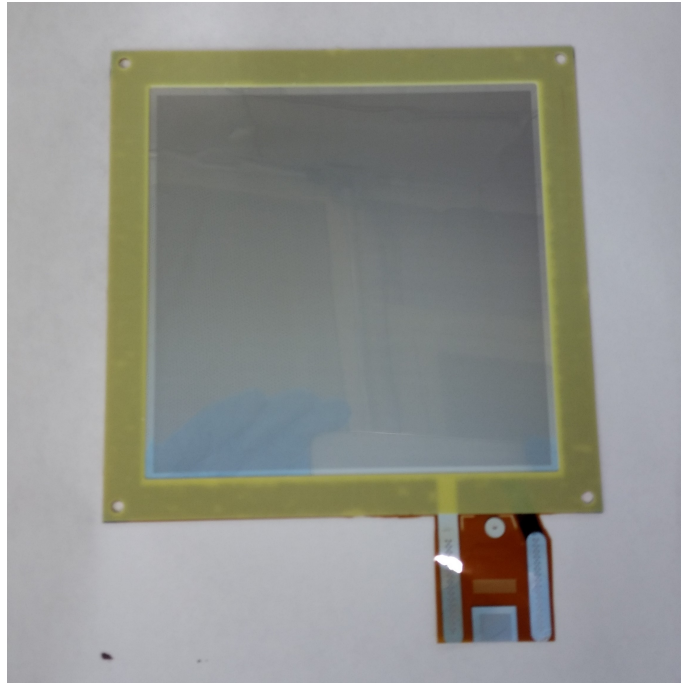


Figure 5.15: Photo of the $10 \times 10 \text{ cm}^2$ aluminium GEM used for the measurements. The active area of the GEM looks darker than the edges due to the dense hole pattern. This GEM was custom-made by the EP-DT-DD Micro-Pattern Technologies service at CERN [64].

how much work is needed to remove an electron from a material. This work can be done by the absorption of photons, particle collisions or heating of the material. The work function is specific to the material. Therefore, if electron emission from the GEM electrodes is relevant, secondary discharges should behave differently for various metal coatings of GEMs.

In order to test the dependence of secondary discharges on the GEM electrode material, measurements are performed with a GEM with aluminium coating, which was produced with the single-mask technique by the EP-DT-DD Micro-Pattern Technologies service at CERN [64]. A photo of the $10 \times 10 \text{ cm}^2$ large GEM can be seen in Fig. 5.15. Aluminium has a lower work function than copper, and consequently is more prone to electron emission. For example, the work functions of copper and aluminium at room temperature are about 4.5–5.1 eV and 4–4.2 eV, respectively [65]. Since the work function is temperature dependent, and more than 1000 K are reached during a primary discharge, these numbers cannot be directly used to compare the copper and aluminium GEMs. What can be said is that less work is required to remove electrons from aluminium than from copper, therefore lower energetic ions can aid the process of secondary discharge. Hence, if the hypothesis described above is the main reason for secondaries, they are expected to occur at lower electric fields.

Unfortunately, the hole geometry of the aluminium GEM, which was produced

with a single-mask procedure, differs from the geometry of the double-mask copper GEM (cf. Sec. 3.2.1). The influence of the single-mask etching on the development of secondary discharges has not been studied yet and is therefore unknown. It cannot be excluded that the asymmetric hole shape of the aluminium GEM affects the electric field around the GEM hole enough to change parameters that influence the build-up of the secondary discharge. This could have an effect on the secondary discharge probability or the time between discharges. Dedicated studies with GEMs from the same material are needed to quantify the differences between single- and double-mask GEMs.

5.6.1 Results

Discharges were recorded with the aluminium GEM in Ar-CO₂ (90-10) and $E_{Drift} \approx 425 \text{ V cm}^{-1}$ for various induction fields. The secondary discharge probability and time between primary and secondary discharge is analysed and compared to the copper GEM.

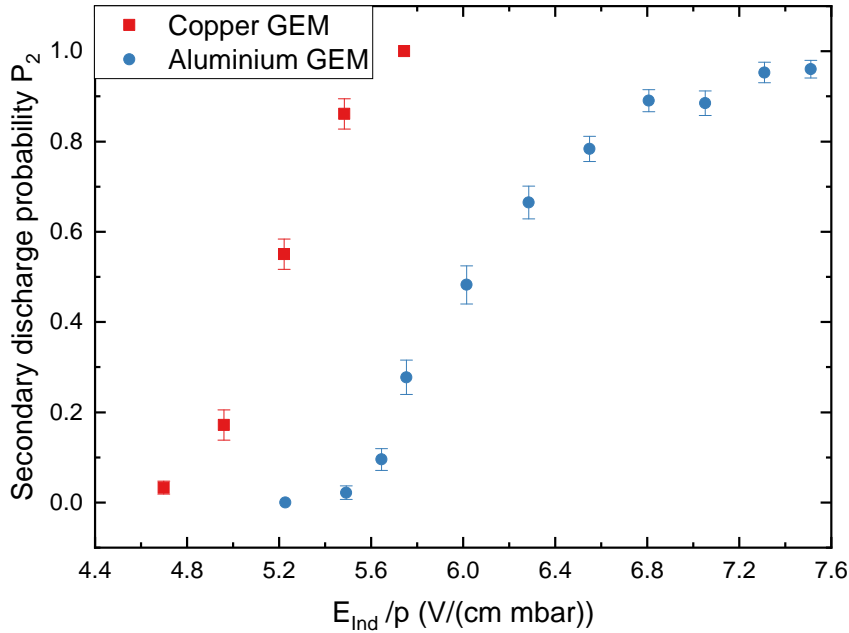


Figure 5.16: Comparison of the secondary discharge probability P_2 in Ar-CO₂ (90-10) between a copper and aluminium GEM as a function of the pressure-normalized induction field E_{Ind}/p . A difference of $\sim 15\%$ in the onset field is visible, which is consistent with the uncertainties introduced by mechanical changes in the setup. The copper GEM was produced with the double-mask technique, whereas the single-mask technique was used for the aluminium GEM. It is unclear what influence the different hole geometry has on the secondary discharge development.

Figure 5.16 shows a comparison of P_2 between the aluminium and the copper GEM. In the case of aluminium, the onset field shifts to a higher induction field $E_{Ind,Al}^{On} = (6.05 \pm 0.05) \text{ V cm}^{-1} \text{ mbar}^{-1}$, compared to $E_{Ind,Cu}^{On} = (5.20 \pm 0.05) \text{ V cm}^{-1} \text{ mbar}^{-1}$ for copper. This corresponds to a difference of about 15% towards higher fields, which is in contrast to the expected behaviour at lower work functions. Furthermore, the rise of P_2 is slower with the aluminium GEM, especially at high probabilities (see also Fig. A.1).

However, this comparison suffers from a few systematic uncertainties that are not reflected by the uncertainties shown in the figure. As mentioned in Sec. 4.3, replacing GEMs introduces mechanical changes in the setup, such as a difference in the length of the induction gap, local changes of the distance due to bending of the GEM (frame) or maybe also fluctuations of production parameters, for example the (average) hole diameter, of the GEM foils. The difference in the onset field, using two GEMs of the same type at the same position, can be up to 12–15% [47].

In addition, the aluminium GEM is produced with the single-mask technique, whereas the copper GEM is of the double-mask type (cf. Sec. 3.2.1). Since no dedicated studies of differences of (secondary) discharges between the two production types have been performed yet, and the shift of the probability curve is of the same order as the shift by simply exchanging GEMs, no conclusive statement about the secondary discharge probability with aluminium GEMs compared to copper GEMs can be made.

Analysing the time between primary and secondary discharge, one finds that the aluminium GEM follows the trend of the copper GEM (Fig. 5.17). The results point towards a time evolution that is independent of the GEM material. In order to confirm this hypothesis, possible differences resulting from the slightly different hole geometry of the two GEMs have to be assessed.

In order to gain confidence in the results of these measurements, it is necessary to investigate the influence of the hole geometry on P_2 and t_2 . Moreover, the precision of the position of a GEM in the detector has to be improved, so that uncertainties due to mechanical differences between measurement of several GEMs are reduced.

5.7 Influence of the direction of the induction field

The role of charge carriers in the creation of secondary discharges can be investigated by reversing the field direction in the discharging gap. In addition to changing the drift direction of electrons and ions, the field close to the GEM hole is varied, which can affect the charge collection at the GEM electrodes. A change of the secondary discharge observables might indicate which kind of particles or mechanisms are more important for its creation. Figure 5.18 shows a secondary discharge with reversed induction field. The voltage across the GEM is not reversed.

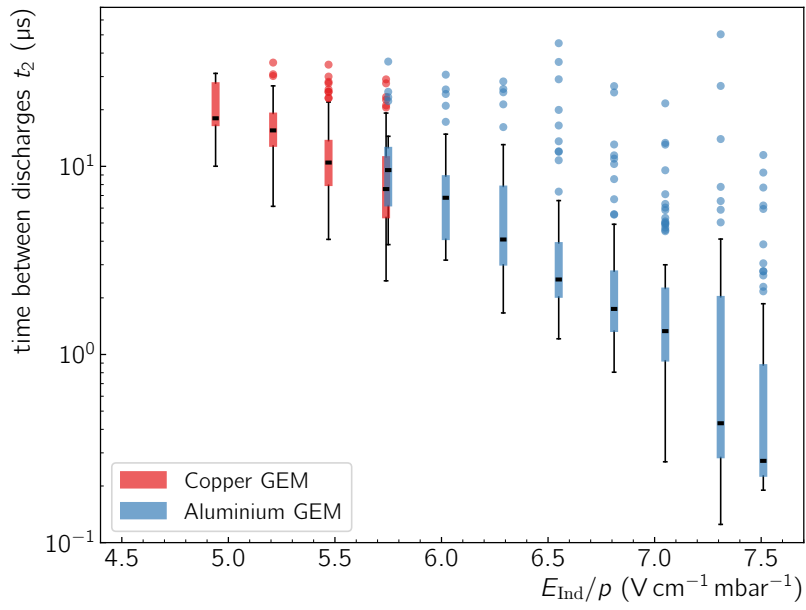


Figure 5.17: Comparison of the time t_2 between primary and secondary discharge in Ar-CO₂ (90-10) between a copper and aluminium GEM as a function of the pressure-normalized induction field E_{Ind}/p . The copper GEM was produced with the double-mask technique, whereas the single-mask technique was used for the aluminium GEM. The aluminium GEM follows the time development of the copper GEM within their uncertainties.

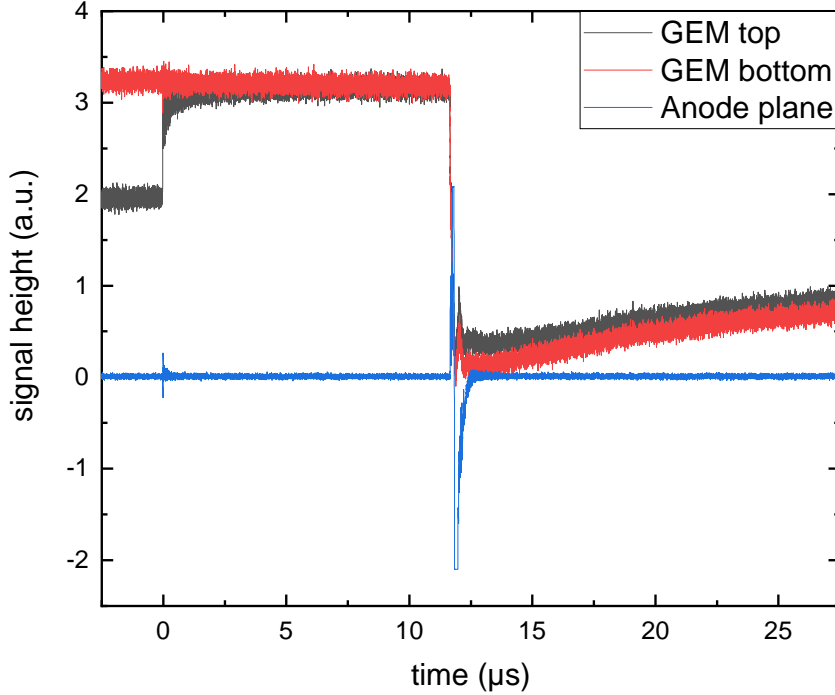


Figure 5.18: Event display of a secondary discharge with a reversed induction field $E_{Ind} = -5.5 \text{ kV cm}^{-1}$ in Ar-CO₂ (90-10) with the aluminium GEM. The anode signal shows saturation at $\pm 2 \text{ V}$ because of the oscilloscope's settings.

5.7.1 Secondary discharge probability and time measurement

As can be seen in Figure 5.19, secondary discharges in the reversed induction field occur at similar electric field strengths as in the normal case, indicating that the evolution of secondary discharges depends, to first order, only on the electric field strength in the discharging gap. This indicates that the crossing of the gas gap by charge carriers, which are created at the time of the primary discharge, are not solely responsible for the secondary discharge.

A remarkable difference can be seen in the shape of the curve. While the inverted field shows a slower increase of P_2 in general, especially the region of low probability shows an earlier, but flatter rise. This could point to favourable conditions for creating secondary discharges, which allows to start the process at slightly lower fields than in the normal case.

No significant difference of t_2 between normal and reversed induction fields can be observed for the aluminium GEM. However, the inverted E_{Ind} copper measurement seems to show a stronger drop of times with increasing induction field. Especially the minimum times in the reversed field are significantly lower. This might be a result of the deterioration of the copper GEM. The measurement with the reversed

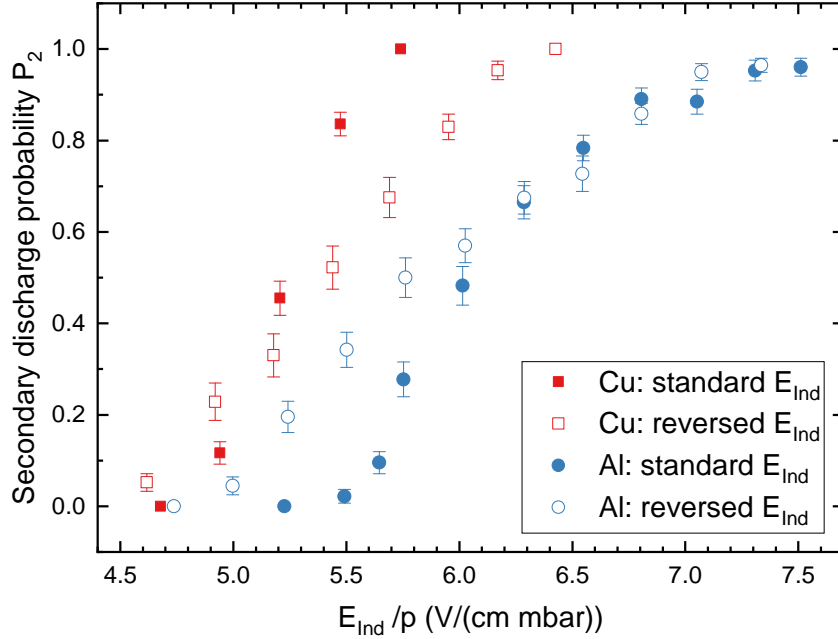


Figure 5.19: Secondary discharge probability P_2 in Ar-CO₂ (90-10) for normal and reversed direction of the induction field. The measurement was done with a copper GEM (Cu) and an aluminium GEM (Al).

induction field with the copper GEM has been carried out after those of Section 5.9, whereas the normal field direction was recorded before the gas mixture was changed. Therefore, the GEM has suffered from several thousands of discharges in the time in between. In contrast to that, the reversed induction field scan with the aluminium GEM has been recorded directly after the normal induction field.

Apart from a few very fast secondary discharges in the reversed induction field with the copper GEM, the times with the different configurations are compatible with each other. This invariance of the time under the field direction is another indication that the initially produced charges do not evolve into the secondary discharge, but rather set up an environment where effects in the gas or the GEM material lead to the full breakdown of the gap.

5.7.2 Inspecting the charge flow with antennas

In order to investigate how the currents behave when different field directions are used, PCB antennas (Fig. 5.21) are connected to the detector instead of high voltage probes. A schematic view of the setup is presented in Figure 5.22. An electrical path parallel to the GEM HV supply paths or the path from the anode to ground picks up current changes, which can be recorded by the oscilloscope. For this setup, the input resistance of the oscilloscope is changed to 50 M Ω , since the antenna signals are small compared to the HV probe signals. However, the impedance of the setup

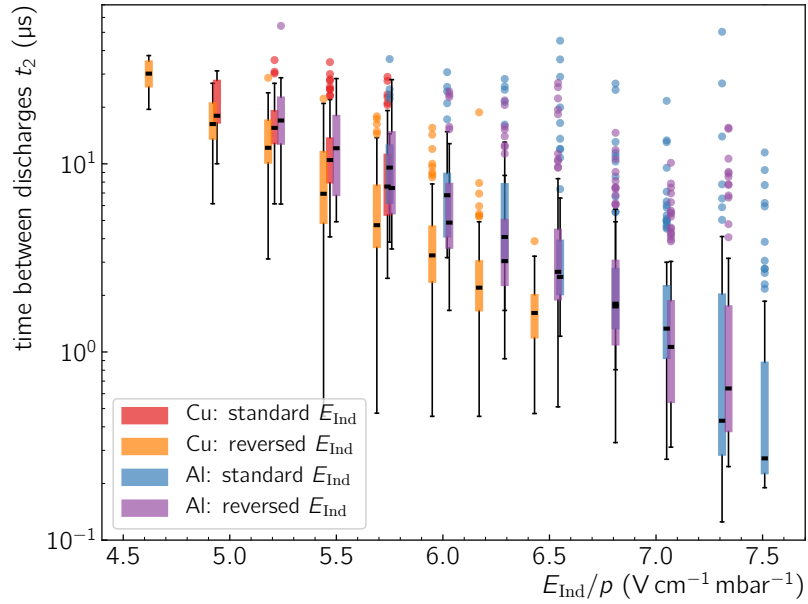


Figure 5.20: Comparison of the time t_2 between primary and secondary discharge in Ar-CO₂ (90-10) for normal and reversed direction of the induction field. Between the two measurements with the copper GEM, discharges were recorded for all the gas mixtures of section 5.9. The significantly lower minimum times in the reversed field case might be a result of the deterioration of the GEM.

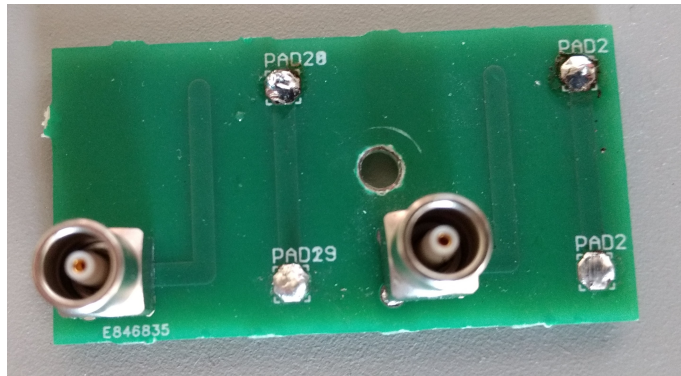


Figure 5.21: Photo of two PCB antennas, which are used to measure the AC currents in the GEM HV supply line and the anode to ground path. The supply path is connected at the metallic contacts labelled *PAD*. The strip parallel to it picks up current changes, which can be recorded by an oscilloscope.

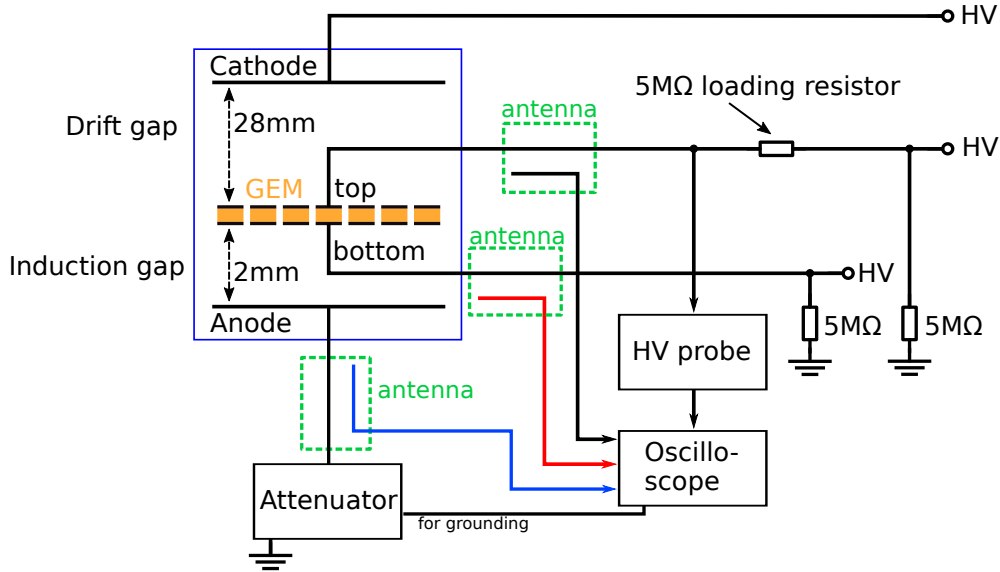


Figure 5.22: Schematic view of the setup employing antennas instead of high voltage probes, in order to directly investigate the AC current of the respective HV supply path. The colours correspond to the ones used in the plots of this section. A photo of the employed antennas can be seen in Fig. 5.21.

is not matched with the oscilloscope, which causes oscillations in the signal for several microseconds. Furthermore, the sensitivity of the antennas is only sufficient to observe high currents during discharges. Therefore, only qualitative observations can be made, especially about the initial direction of charge flow. In addition to the antennas, one HV probe is connected to the GEM top side, so that the trigger can discriminate between primary and secondary discharges.

By comparing the recorded signals for different field directions, one might be able to identify if there are differences in the secondary discharge process. Furthermore, one can investigate if the occasional reignition of a secondary discharge (cf. Sec. 4.3) shows the same behaviour as the normal one.

The following waveforms are all recorded with the aluminium GEM in Ar-CO₂ (90-10) at $|E_{Ind}| = 5.5 \text{ kV cm}^{-1}$, $E_{Drift} = 400 \text{ V cm}^{-1}$ and no decoupling resistor. Since the signal of each discharge type for a specific voltage setting is always similar, an average of 20 waveforms is taken in order to reduce noise. The bandwidth of the oscilloscope is limited to 20 MHz in order to improve the readability of the signal. Figures with a bandwidth of 200 MHz can be found in the appendix A.2.

Primary discharge

Figure 5.23 shows a comparison of the antenna signals during a primary discharge. The initial peak represents the current flow. A rise indicates an increasing output

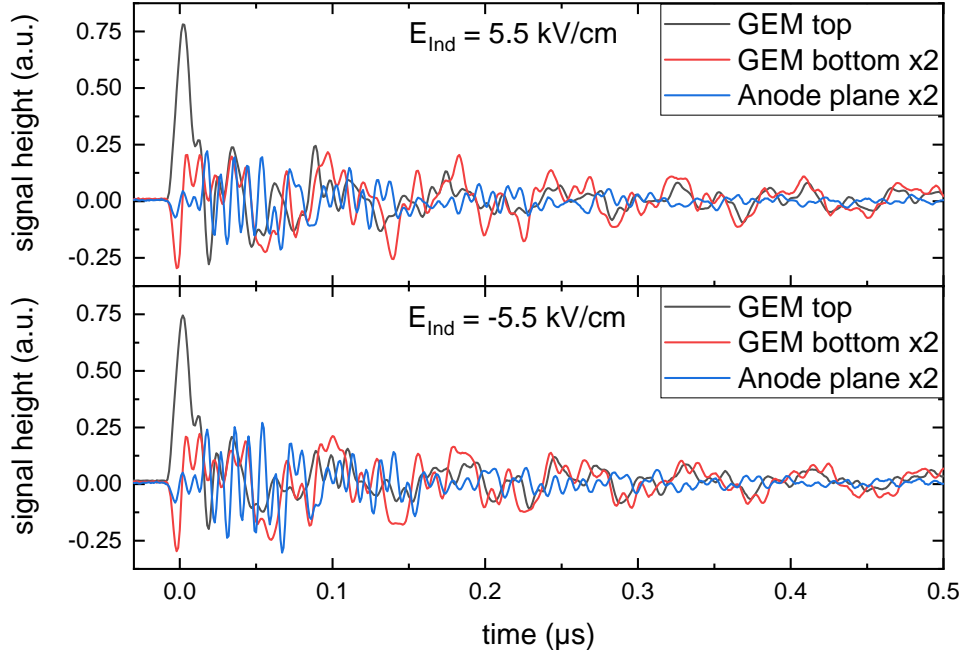


Figure 5.23: Average of 20 signals recorded by antennas during a primary discharge at normal (top) and reversed induction field (bottom) with $|E_{Ind}| = 5.5 \text{ kV cm}^{-1}$. The bandwidth is limited to 20 MHz.

current of the power supply, which counteracts the change of the GEM potential towards more positive values, and vice versa. As expected, the signals look alike in both cases, since the formation of the primary discharge does not depend on E_{Ind} . The GEM top potential shows a drop in both cases, with only a small current being induced in GEM bottom and the anode.

After the initial peak, fast oscillations are visible that decay on a time scale of $1 \mu\text{s}$, a time which is significantly lower than the average time between primary and secondary discharge. Therefore, they are most likely due to the reflections in the cables and are not the result of a current through the induction gap, which might build up the secondary discharge.

Secondary discharge

As can be seen in Figure 5.24, the secondary discharge signal shows the same features in the reversed induction field as in the normal case, but reversed in polarity: Both GEM potentials drop towards the anode potential, either from a negative (normal field) or positive potential (reversed field). In addition, a signal in the anode can be seen. Since the secondary discharge connects the GEM bottom electrode with the anode, the initial peak in the anode signal points in the opposite direction as the GEM potentials. The signal of the inverted field case is flipped vertically compared to the normal field, since the GEM bottom potentials are of opposite polarity. In

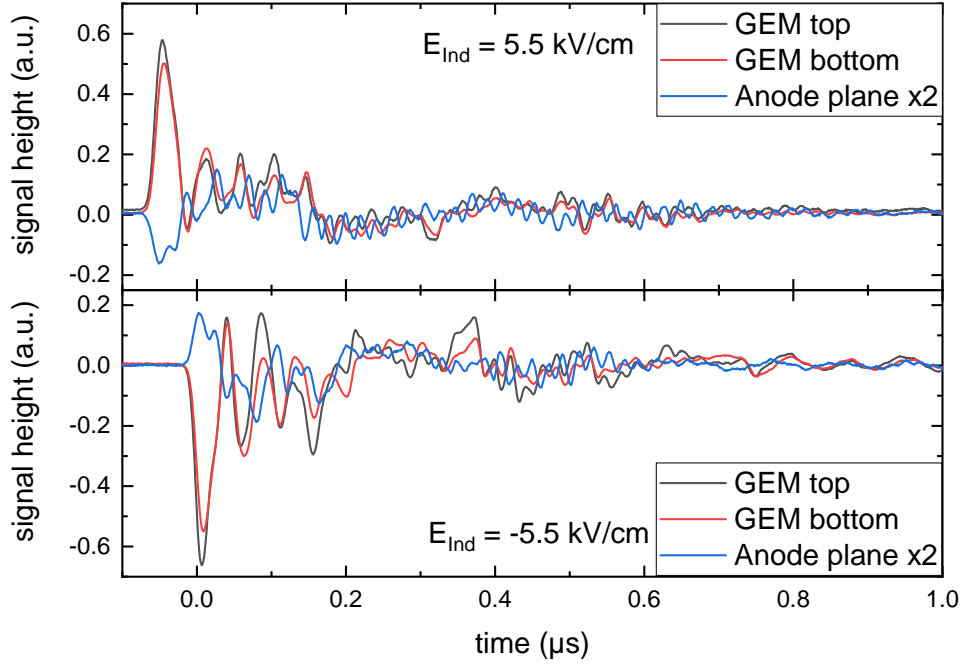


Figure 5.24: Average of 20 signals recorded by antennas during a secondary discharge at normal (top) and reversed induction field (bottom) with $|E_{Ind}| = 5.5 \text{ kV cm}^{-1}$. The bandwidth is limited to 20 MHz.

both cases, a weak oscillation with a period of about $0.4 \mu\text{s}$ can be seen. Due to different trigger settings, the signal of the reversed field case in Fig. 5.24 starts at a later time.

The similarity of the signals supports the idea that a process of the same nature is responsible for the secondary discharge in both field directions.

Reignition of secondary discharges

In some cases, another potential drop shortly after the secondary discharge can be observed before the GEM potentials reach their nominal voltages again (cf. Sec. 4.3). For such cases, it is not possible to average several signals, since it is not possible to trigger on the third potential drop in our setup. An event with such a third potential drop is shown in Figure 5.25. A close-up comparison of the antenna signals of the secondary discharge ($t = 0 \mu\text{s}$) and the third potential drop ($t \sim 52 \mu\text{s}$) shows that the signals display the same behaviour, but with different amplitudes (Fig. 5.26). This can be explained by the smaller potential drop at the third discharge. Therefore, the third discharge seems to correspond to a *reignition* of the secondary discharge. Indeed, measurements with a high-speed camera confirm that in some cases the secondary discharge lights up again at the same position, which is accompanied by a voltage drop [51].

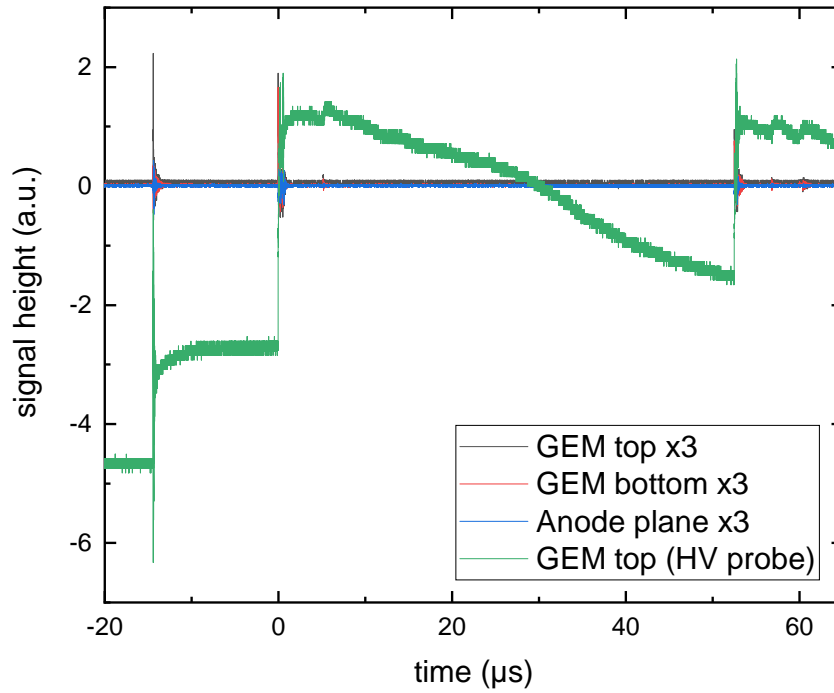


Figure 5.25: Signal of an event with a third potential drop ($t \sim 52 \mu\text{s}$) after the secondary discharge ($t \approx 0 \mu\text{s}$). The GEM top potential recorded by the HV probe passes the zero level due to the usage of a bad LEMO cable, which introduced a scaling factor. The waveform was recorded at $E_{Ind} = 5.5 \text{ kV cm}^{-1}$ without a decoupling resistor.

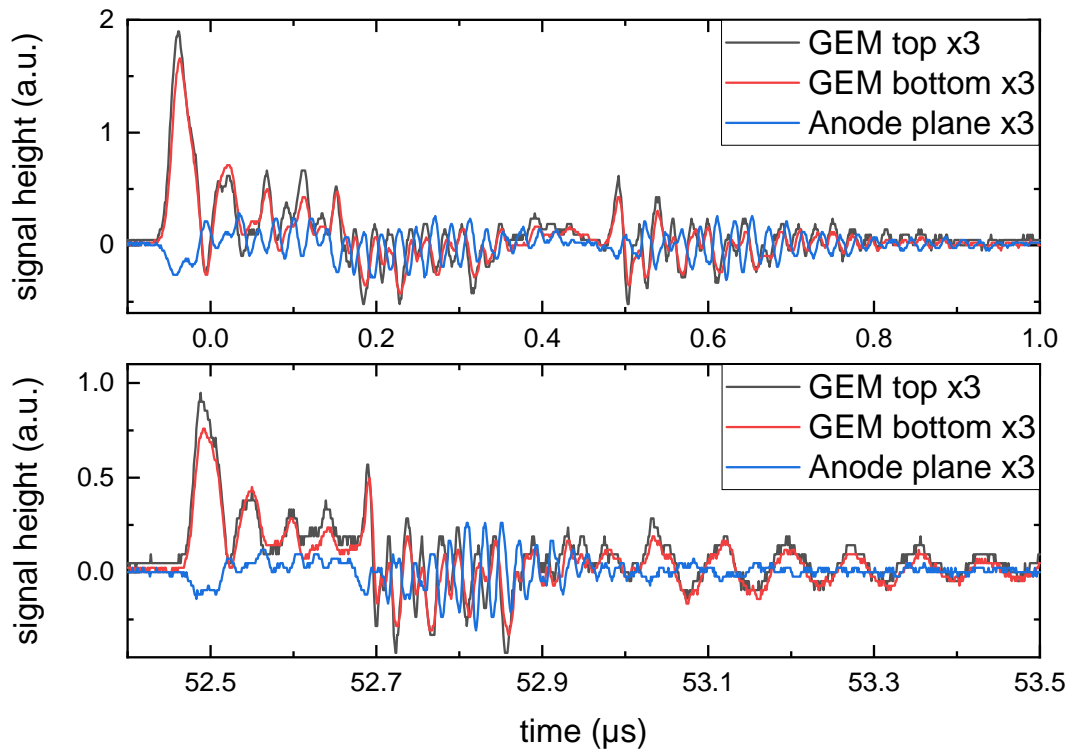


Figure 5.26: Comparison of the antenna signals during the secondary discharge (top) and the third potential drop (bottom) of Fig. 5.25. The y -axes have different scales in order to improve the visibility of the signal. The bandwidth is limited to 20 MHz.

Reignition of secondary discharges with an aluminium GEM

During the measurements with the aluminium GEM, it was frequently observed that the secondary discharge reignited many times in the first $\sim 100 \mu\text{s}$ after the initial secondary discharge (Fig. 5.27). The effect is more pronounced than with copper, where the secondary discharge reignited less often (cf. Fig. 4.7). This could be explained by the fact that aluminium is more prone to electron emission than copper. However, it has also to be considered that the induction fields of the aluminium measurements are significantly stronger (see Fig. 5.16). Therefore, it might also be an effect of the strength of the electric field, and not necessarily of the material. Dedicated measurements are needed to quantify the effect. In the scope of this thesis, priority was given to the investigation of the initial conditions needed to produce a secondary discharge. Hence, no quantitative analysis of the reignition phenomenon was conducted.

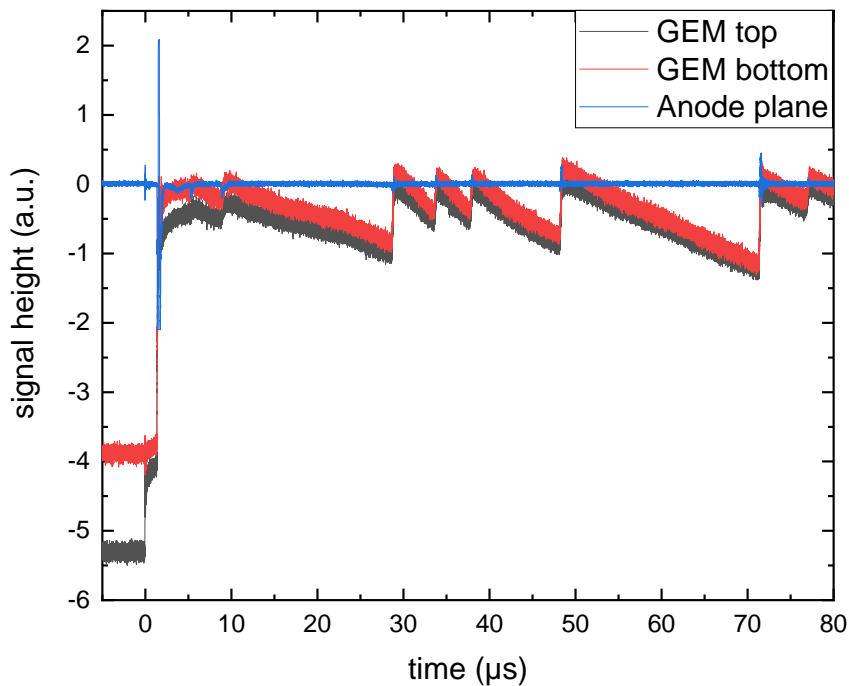


Figure 5.27: Display of the GEM potentials and anode signal measured with the HV probes. The signal was recorded with the aluminium GEM at $E_{Ind} = 6.5 \text{ kV cm}^{-1}$. The secondary discharge reignites frequently ($t > 5 \mu\text{s}$).

5.8 Mitigation of secondary discharges using decoupling resistors

The addition of a resistor in the HV supply path to GEM bottom electrode *decouples* the foil from capacitances introduced by the powering scheme, therefore it is also called decoupling resistor. Moreover, the charging of the GEM, which acts as a capacitor, is slowed down by the resistor.

In previous studies [36, 47], it has been found that the introduction of decoupling resistors has a mitigating effect on secondary discharges, i.e. the onset of P_2 happens at higher induction fields. In that work, a double-GEM setup has been used. Unfortunately, with only two HV probes being available, not all GEM potentials could be monitored. As a consequence, the evolution of the electric field in the discharging gap is not clear. Nevertheless, a different evolution of the GEM potentials after the primary discharge than without decoupling resistors could be identified. Thus, the electric field is temporarily altered. It was hypothesized that this change is responsible for the mitigating effect of decoupling resistors

In this section, decoupling resistors of $R_D = 50\text{ k}\Omega, 100\text{ k}\Omega$ are employed to investigate their mitigating effect on secondary discharges in the induction gap. The GEM potentials and the time between primary and secondary discharge are carefully monitored in order to provide a deeper understanding of the discharge mitigation. For all measurements, the aluminium GEM is used in Ar-CO₂ (90-10). Otherwise the setup is kept unchanged except for the decoupling resistors. Hence, no mechanical uncertainties are introduced between the different measurement series.

5.8.1 General observations

Introducing a decoupling resistor to the biasing scheme leads to a different evolution of the GEM potentials after the primary and secondary discharge. Figure 5.28 shows the time evolution of the GEM potentials in the event of a secondary discharge.

When a primary discharge occurs, the GEM top potential drops to the bottom potential as in the $R_D = 0$ case. However, both potentials continue to drop together for a few microseconds. With a $50\text{ k}\Omega$ resistor, it takes about $4\text{ }\mu\text{s}$ until the GEM potentials start to approach the nominal value again, and about $10\text{--}20\text{ }\mu\text{s}$ until they reach the nominal bottom potential. This voltage drop is a strong indicator of an electric current through the induction gap.

When the secondary discharge occurs ($t \sim 13\text{ }\mu\text{s}$ in Fig. 5.28), the potentials do not fully drop to the anode potential and start oscillating for several $100\text{ }\mu\text{s}$. The frequency of the oscillation seems to be constant over the observed time window, but vary in amplitude. Unfortunately, the given resolution and level of noise do not allow to perform a Fourier analysis on the waveforms. As soon as the oscillations stop, the GEM potentials start to recover (Fig. 5.29). However, they seem to temporarily reach even higher (negative) potentials ($t \sim 10\text{ ms}$). At this time, the extreme conditions created by a primary discharge have already subsided. Since no significant voltage

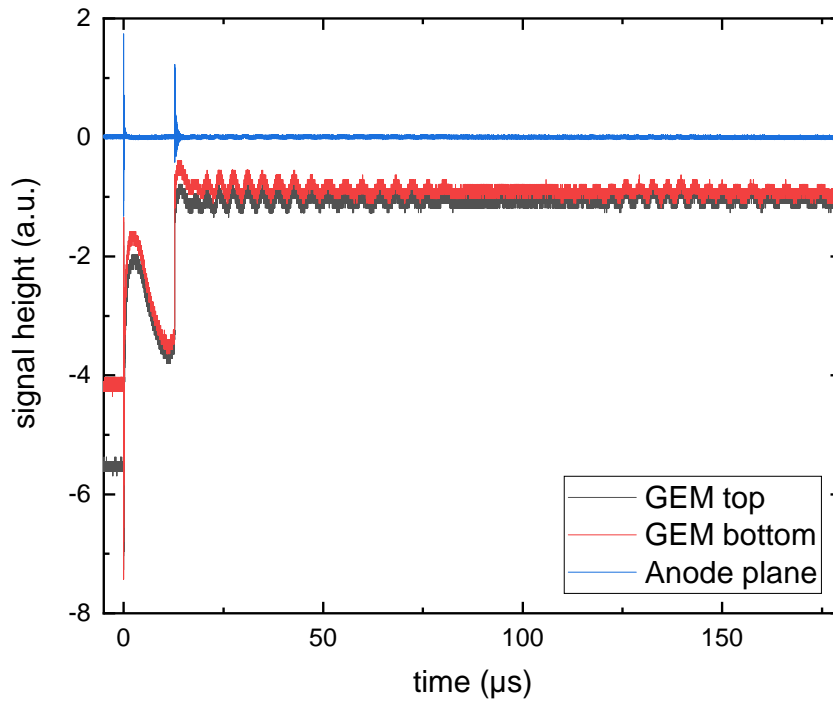


Figure 5.28: Display of a primary ($t = 0$ s) and secondary discharge ($t \sim 13 \mu\text{s}$) when the setup is biased with a $50 \text{ k}\Omega$ decoupling resistor. An electric field of $E_{Ind} = 7.5 \text{ kV cm}^{-1}$ is applied. In contrast to the $R_D = 0$ case (cf. Fig. 4.6a), both GEM potentials drop even further after the primary discharge. At $t \sim 4 \mu\text{s}$, the potentials start to approach the nominal GEM bottom potential again. During the secondary discharge, the GEM potentials do not fully reach the anode potential. Afterwards, long lasting oscillations can be seen.

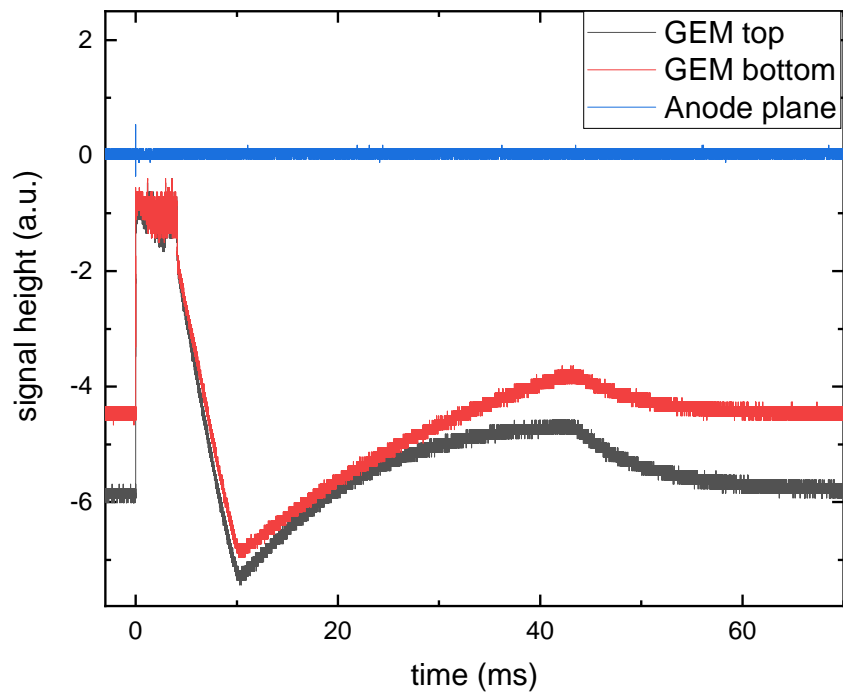


Figure 5.29: High voltage probe signals of a GEM after a secondary discharge. The GEM is biased with $R_D = 50 \text{ k}\Omega$. After the secondary discharge, the GEM potentials oscillate for around 5 ms before they start to recover.

across the GEM is present, no new primary discharges, and thus also no secondary discharges, can be triggered. Eventually, the two GEM potentials separate again and reach their nominal potentials around $t \sim 70$ ms.

5.8.2 Effect of the decoupling resistor on the secondary discharge probability

As presented in Figure 5.30, the onset field of secondary discharges increases with the decoupling resistance R_D . A linear increase of E_{Ind}^{On} is observed (Fig. 5.31), where the value of the onset field is determined by interpolation of the curves of Fig. 5.30 to the value where $P_2 = 0.5$. An uncertainty of $0.05 \text{ V cm}^{-1} \text{ mbar}^{-1}$ is assigned for this method. A linear fit to $E_{Ind}^{On}(R_D)$ yields a slope of $(20.0 \pm 0.1) \text{ V cm}^{-1} \text{ mbar}^{-1} \Omega^{-1}$.

In order to understand the mitigation process, the time between primary and secondary discharge and its relation to the GEM potentials are investigated in the following sections.

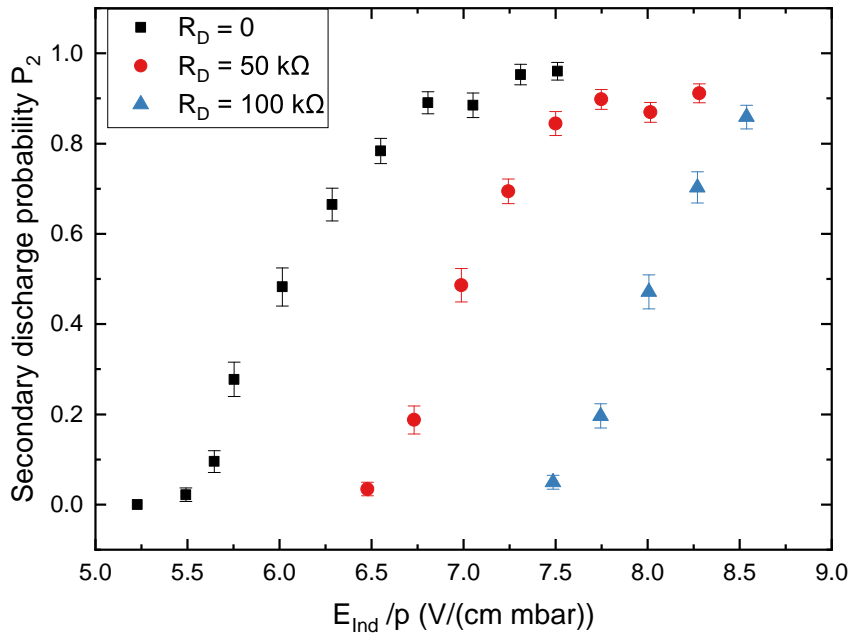


Figure 5.30: Secondary discharge probability P_2 as a function of E_{Ind}/p for different decoupling resistors R_D . The onset field increases by about $1 \text{ kV cm}^{-1} \text{ mbar}^{-1}$ per $50 \text{ k}\Omega$ decoupling resistance.

5.8.3 Determining the time between primary and secondary discharges

In order to reach a secondary discharge probability of around 100% when using decoupling resistors, it is necessary to go to high electric fields of the order of

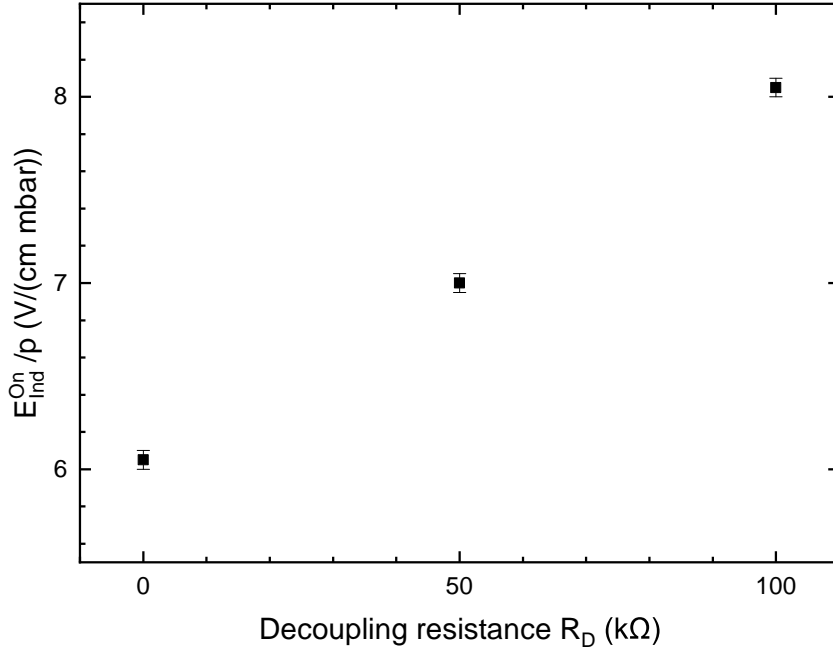


Figure 5.31: Secondary discharge onset field E_{Ind}^{On} extracted from Fig. 5.30 as a function of R_D . A linear fit to E_{Ind}^{On} yields a slope of $(20.0 \pm 0.1) \text{ V cm}^{-1} \text{ mbar}^{-1} \Omega^{-1}$.

8 kV cm^{-1} . As was already observed without decoupling resistor (for example Fig. 5.17), secondary discharges in high electric fields can occur already a few 100 ns after the primary one. In the specific case of $R_D > 0$, the voltage drop after a primary discharge creates a challenging environment for numerical analyses. Figure 5.32 shows a secondary discharge that occurs after only $\sim 170 \text{ ns}$. The oscillations at $t \approx 0 \text{ s}$, combined with the significantly smaller voltage drop of the secondary discharge than without decoupling resistor, lead to an unreliable detection of the secondary discharge with the method used before (cf. Sec. 5.3.2).

The characteristic features of an event with a secondary discharge are the two steep voltage drops of the GEM top potential, of which the first is always at $t = 0 \text{ s}$. That means that if one can reliably detect the position of the potential drop of the secondary discharge, even if the jump is relatively small, one can determine the time of the secondary discharge. For this, a script was developed using Python 2.7 [66]. The idea of finding the secondary discharge is based on taking the derivative of the GEM top potential: The jump of the signal leads to a large peak in the derivative of the signal, which can be detected by a peak finder. However, the large oscillations at small times result in similar peaks in the derivative. Simply using a peak finder would lead to an increasing number of misidentified secondary discharges as the times become shorter. To work around this problem, a low-pass frequency filter is applied to the GEM top signal in order to remove the fast oscillations. This process

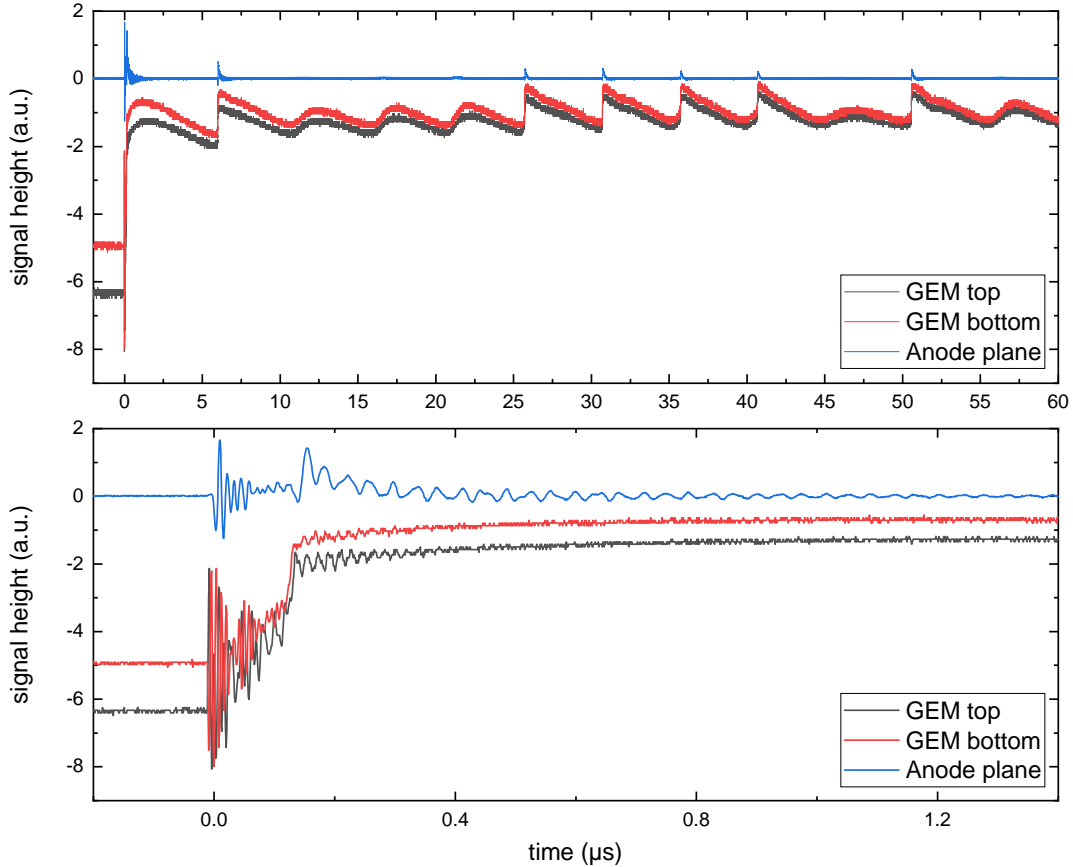


Figure 5.32: A fast secondary discharge ($t \approx 0.17 \mu\text{s}$) at $E_{Ind} = 8 \text{ kV cm}^{-1}$ with $R_D = 100 \text{ k}\Omega$. During the oscillations after the secondary discharge, further discharges between the GEM and anode can be observed. The lower figure shows the same event but displays a shorter time window.

is shown in Figure 5.33. The single analysis steps are described in what follows:

- a) The GEM top potential is imported.
- b) A *real Fast Fourier Transformation* (rFFT) is applied to the data.
- c) For all frequencies above 45 MHz, the amplitude is set to 0. This corresponds to a rectangular cut in the frequency space.
- d) An inverse rFFT is applied to retrieve the smoothed GEM top potential.
- e) The derivative of the smoothed GEM top potential is taken and another smoothing is applied. This is necessary because of the rectangular cut in frequency space. Since the function of c) corresponds to the rFFT of a) convoluted with a step function, the back-transformation results in a convolution

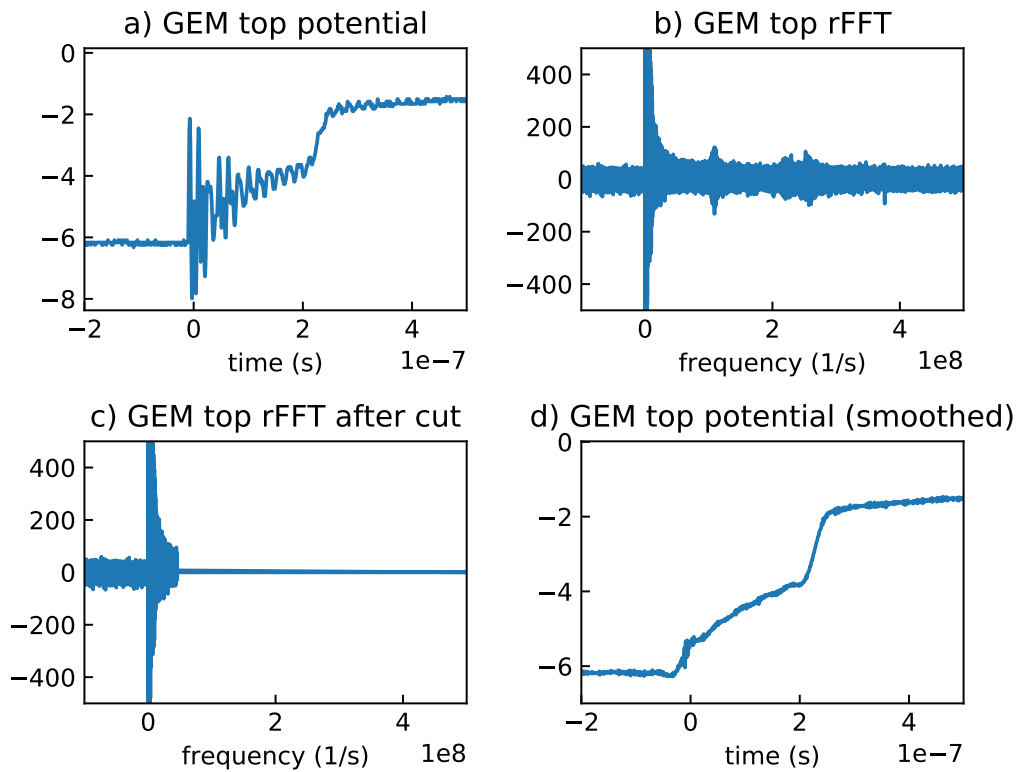


Figure 5.33: Display of the steps of applying a low-pass filter to the GEM top potential. By applying a real fast fourier transformation (rFFT), all frequencies above 45 MHz are removed. The lettering corresponds to the one used in the text. A different than in Figure 5.32 is used.

of the signal with $\sin(t)/t$. Except for the beginning and the end of the data, these oscillations are relatively small. Nonetheless, the peak finder sometimes detects additional peaks from the noise.

- f) A peak finder searches for peaks with $t > 0$.
- g) To avoid associating the wrong peak to the secondary discharge, the peak with the highest amplitude is chosen. The time stamp of this peak corresponds to the time of the discharge.
- h) An output file is created which displays the (smoothed) GEM top potential, its derivative and the position of the secondary discharge. The event is classified as either a primary discharge only or as initial and secondary discharge. One example of the output can be seen in Figure 5.34. Other scenarios are displayed in the appendix A.3.
- i) The script loops through all files of one HV setting and determines the time

difference for all events with secondary discharge. All output displays are saved in a single PDF file, which allows to quickly verify all events by eye. In addition, the file name is printed, so that events which are misidentified can be inspected and used to improve the script. After optimising the free parameters of the script, all waveforms were treated correctly.

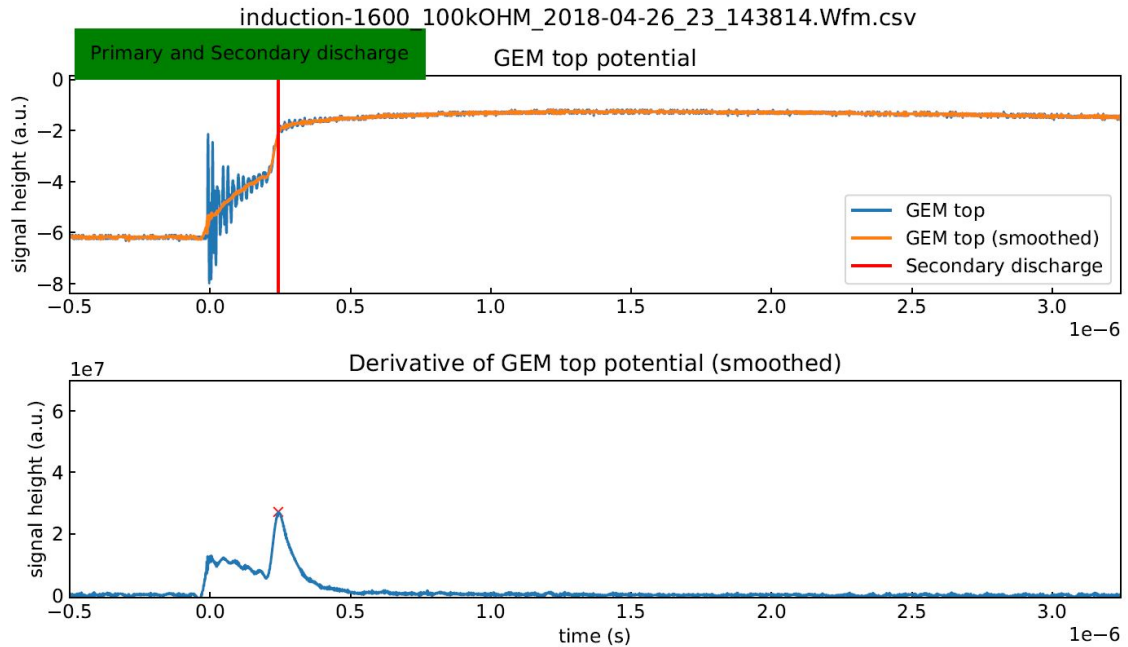


Figure 5.34: Example of the output of the analysis script described in the text. A peak finder identifies the position of the secondary discharge in the derivative of the GEM top potential (orange cross in the bottom figure). The corresponding time is marked in the GEM top potential. A box in the top left corner displays if a secondary discharge was found or not.

As can be seen in Fig. 5.34, this analysis methods detects the end of the potential drop—where the numerical derivative of GEM top is at a maximum—as the time of the secondary discharge. However, the duration of the potential drop of the secondary discharge, and therefore the systematic uncertainty of its detection, is of the order of ~ 50 ns, which is significantly smaller than the fluctuations of t_2 . Therefore, systematic uncertainties are neglected.

The time between primary and secondary discharge for different decoupling resistors is presented in Figure 5.35. With increasing resistance, the secondary discharge needs a longer time to develop. The minimum time for secondary discharges at $E_{Ind}/p < 8 \text{ V cm}^{-1} \text{ mbar}$ seems to be around $7 \mu\text{s}$ ($11 \mu\text{s}$) for $R_D = 50 \text{ k}\Omega$ ($R_D = 100 \text{ k}\Omega$). However, at larger fields, secondary discharges start to appear at 100–500 ns. No discharges are observed between these fast secondaries and the “minimum” mentioned before. With increasing electric field, the amount of fast secondary discharges increases. This leads to a misleading representation of the last point of

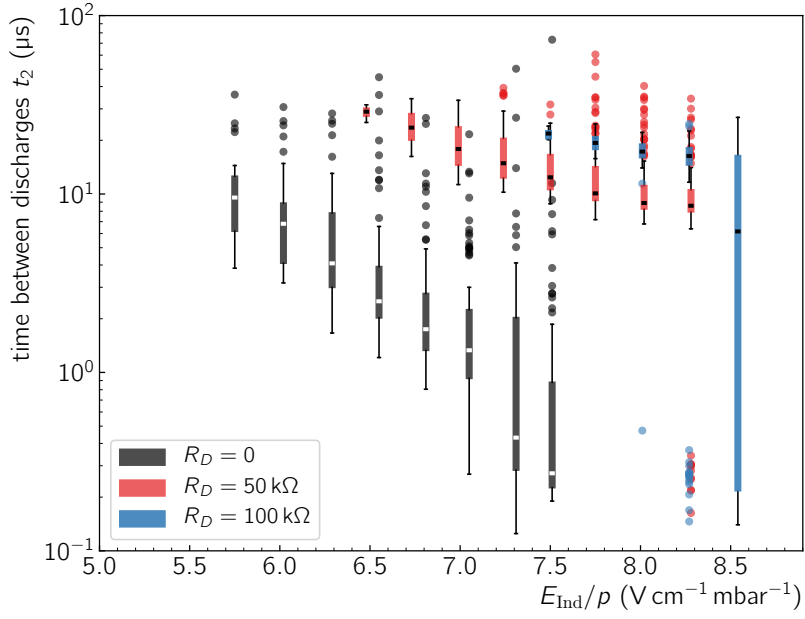


Figure 5.35: Time between primary and secondary discharge as a function of E_{Ind}/p for different decoupling resistors.

$R_D = 100\text{ k}\Omega$ in 5.35, since about half of the recorded data is at low times. As a result, the box around the median bridges the gap between small and large times. The time distributions are also presented as histograms in Figure 5.36, where only times for the four highest induction fields ($7.5\text{ kV cm}^{-1} \leq E_{Ind} \leq 8.25\text{ kV cm}^{-1}$) with decoupling resistances of $50\text{ k}\Omega$ and $100\text{ k}\Omega$ are plotted. All time distributions of this measurement can be found in Appendix C.4.

5.8.4 Potential evolution after the primary discharge as driving factor of secondary discharge mitigation

As shown in the previous section, the time between primary and secondary discharge decreases for increasing electric fields. However, the times seem to level off at a minimum time, which is around $7\text{ }\mu\text{s}$ ($11\text{ }\mu\text{s}$) for $R_D = 50\text{ k}\Omega$ ($R_D = 100\text{ k}\Omega$). When the field is increased enough, secondary discharges start to appear at $t < 500\text{ ns}$, but nothing is observed in between.

The suppression of secondary discharges in this time window originates from the evolution of the GEM bottom potential, which defines the strength of E_{Ind} . As can be seen in Fig. 5.37, the GEM bottom potential drops after the primary discharge and reaches its maximum (minimal voltage across the induction gap) after a few microseconds. The strength of the potential drop and the time it takes to recover from it are dependent on R_D . A higher resistance induces a stronger potential drop

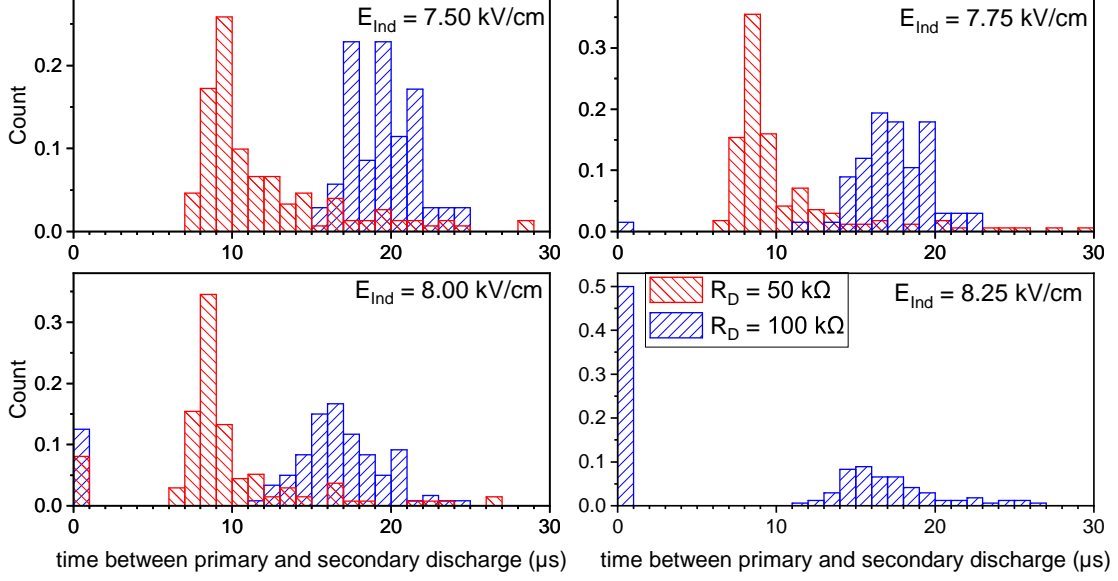


Figure 5.36: Normalized distributions of the time between primary and secondary discharge for $R_D = 50 \text{ k}\Omega$ (red) and $R_D = 100 \text{ k}\Omega$ (blue) at different induction fields. No measurement with $R_D = 50 \text{ k}\Omega$ was recorded at $E_{Ind} = 8.25 \text{ kV cm}^{-1}$.

and slows the recharging of the GEM down. This potential drop seems to have a mitigating effect on the secondary discharge. Due to the temporary reduction of the induction field, the secondary discharge cannot develop. Only when E_{Ind} starts to increase again are the conditions sufficient to cause a full breakdown of the gap. As a consequence, secondary discharges are observed only after the maximum of the voltage drop. In addition, this observation confirms again that the electric field strength in the gap is the driving factor for the occurrence of secondary discharges.

When the electric field is increased to about 8 kV cm^{-1} , secondary discharges start to appear before the voltage drop reaches its maximum. There, the electric field is still strong enough to trigger the discharge. Figure 5.38 shows the same situation as Fig. 5.37, but for smaller times and with a finer resolution. Although the GEM bottom potential starts to decrease immediately, there is still enough time with high E_{Ind} for a secondary discharge to evolve.

The fact that secondary discharges only occur before or after the potential drop on GEM bottom leads to the conclusion that the time evolution of the electric field after a primary discharge is responsible for the mitigation of secondary discharges via decoupling resistors. A higher electric field is needed to compensate the voltage drop induced by the decoupling resistor, which effectively shifts the onset of secondary discharges to higher applied electric fields.

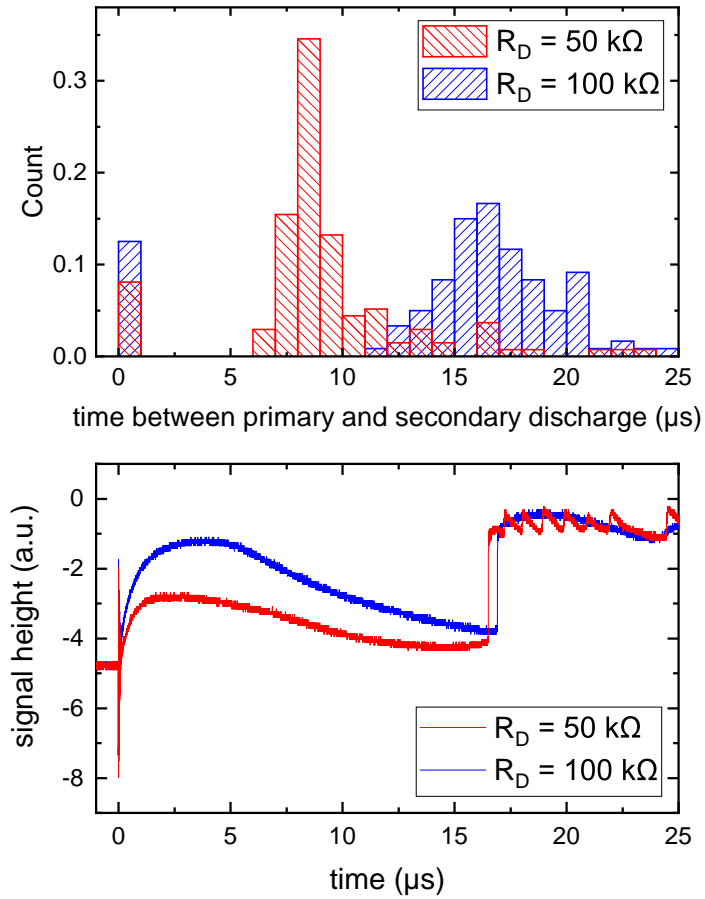


Figure 5.37: Comparison of the GEM bottom potential, which defines E_{Ind} , and the normalized distributions of the time difference between primary and secondary discharge at an applied induction field of $E_{Ind} = 8 \text{ kV cm}^{-1}$. No secondary discharges occur around the maximum of the potential drop.

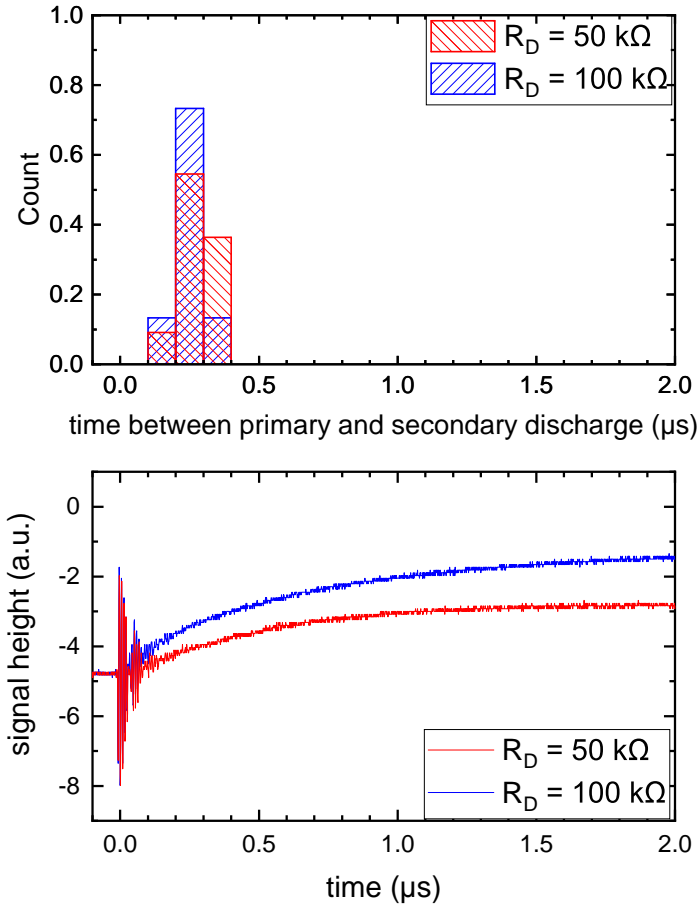


Figure 5.38: Comparison of the GEM bottom potential, which defines E_{Ind} , and the normalized distributions of the time difference between primary and secondary discharge at an applied induction field of $E_{Ind} = 8 \text{ kV cm}^{-1}$. The same data as in Fig. 5.37 is displayed, but with a finer time resolution. For up to 400 ns after the primary discharge, the electric field is still high enough to sometimes trigger secondary discharges.

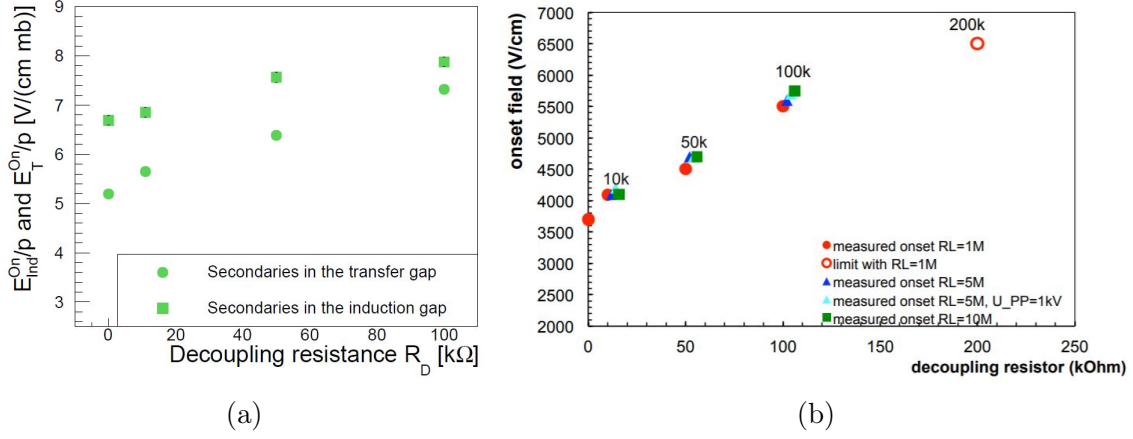


Figure 5.39: (a) E_{Ind}^{On}/p and the onset field in the transfer gap E_T^{On}/p as a function of R_D , where E_T^{On} is defined as the value of $E_T + \Delta U_{GEM2}/d_t$, where $P_2 = 0.5$ [36]. The measurement has been conducted in Ar-CO₂ (90-10). (b) Onset field E_{Ind}^{On} for different decoupling resistors in Ne-CO₂-N₂ (90-10-5). A cascaded power supply is used to bias the detector [54].

5.8.5 Comparison to previous measurements

In [36, 47], the mitigating effect of decoupling resistors was investigated in a two-GEM setup. The shift to higher fields was found to differ in strength for the induction and transfer field (Fig. 5.39a). The authors found a slope of $(12 \pm 1) \text{ V cm}^{-1} \text{ mbar}^{-1} \Omega^{-1}$ and $(20 \pm 1) \text{ V cm}^{-1} \text{ mbar}^{-1} \Omega^{-1}$, respectively.

Unfortunately, only one HV probe per GEM could be used, which makes the interpretation of the evolution of the transfer field difficult. While the decoupling resistors change the potentials significantly, the behaviour seems to be slightly different than what is shown in Fig. 5.28. In addition, the effect of primary discharge propagation from GEM2 to GEM1 was only found at a later time. It is likely that secondary discharges with and without primary discharge in GEM1 have been mixed. Since secondary discharges in the latter case appear at higher electric fields [48], it seems reasonable that the mitigating effect is stronger in the transfer gap.

The significant difference to the measurement in the induction gap of this work might be explained by a slightly different biasing scheme. Employing $R_{top} = 10 \text{ M}\Omega$ might lead to a different voltage drop with respect to our case, and therefore a different mitigation effect. Pre-amplification of charges in GEM1, as well as capacitive coupling, might also play a significant role.

In [54], the effect of decoupling resistors in a single-GEM detector with a cascaded power supply and a Ne-CO₂-N₂ (90-10-5) gas mixture was investigated (Fig. 5.39b). A similar effect as in Sec. 5.8.2 was found. However, the use of a cascaded PS instead of an independent channel power supply might lead to a different potential evolution after a discharge. In addition, the electron and ion drift velocity in the neon-based gas mixture differs. Hence, the two measurements cannot be easily compared.

Ultimately, it seems that the effectiveness of decoupling resistors to mitigate secondary discharges is highly dependent on the specific setup and has to be optimised for each application.

5.9 Employing different gas mixtures

So far, it has been found that secondary discharges start to occur after a certain electric field strength is surpassed and that the time of the secondary discharge relative to the initial discharge decreases (exponentially) with increasing electric field (e.g. Fig. 5.19 and 5.20). This happens at values where no electron amplification is present [28]. In addition, an electric current flowing through the gas gap can be observed (Sec. 5.8.1), as well as a glow of the cathode and gas [51]. Measurements with reversed induction field or with decoupling resistors show that the strength of the electric field after the primary discharge is the driving factor for the occurrence of secondary discharges. The GEM electrode material or the ion extraction do not seem to play a significant role.

These features point to a mechanism that is dependent on the gas parameters. As part of a larger investigation, the dependence of the secondary discharge probability and of the time difference on the gas mixture were measured in the scope of this thesis (Sec. 5.9.1). In [48], the properties in the gas are further investigated. The onset field for different gas mixtures, which is determined in this thesis, is used there to compare the electron energy distribution and the ion velocity between the different gases at their respective E_{Ind}^{On} . In the same work, the current through the induction gap in the time between primary and secondary discharge is measured, and shows a correlation to the previously mentioned parameters. Based on these findings, a mechanism for the secondary discharge is proposed. Section 5.9.2 gives an overview of the subsequent measurements of [48]. In the same work, a mechanism for the secondary discharge is proposed, which will be presented and discussed in Section 5.9.3.

5.9.1 Secondary discharge probability and time difference

Secondary discharges are measured with a copper GEM in Ar-CO₂ with varying CO₂ content between 10% and 30% at 10 L/h gas flow and in Ne-CO₂-N₂ (90-10-5) at 10.5 L/h. No decoupling resistor at GEM bottom is present. The hardware configuration during all measurements is the same, therefore the onset fields or the times between primary and secondary discharge are comparable with each other.

The secondary discharge probability is displayed in Figure 5.40. With rising CO₂ content, the secondary discharge onset field moves to higher induction fields. For every 5% of CO₂, E_{Ind}^{On} shifts by 0.4–0.6 V cm⁻¹ mbar⁻¹. The shape of all curves is the same (see also Fig. A.2). For Ne-CO₂-N₂ (90-10-5), the onset is lower by about 1 V cm⁻¹ mbar⁻¹ than for Ar-CO₂ (90-10). Unfortunately, not enough neon was available to record a full curve or to gather a high number of events.

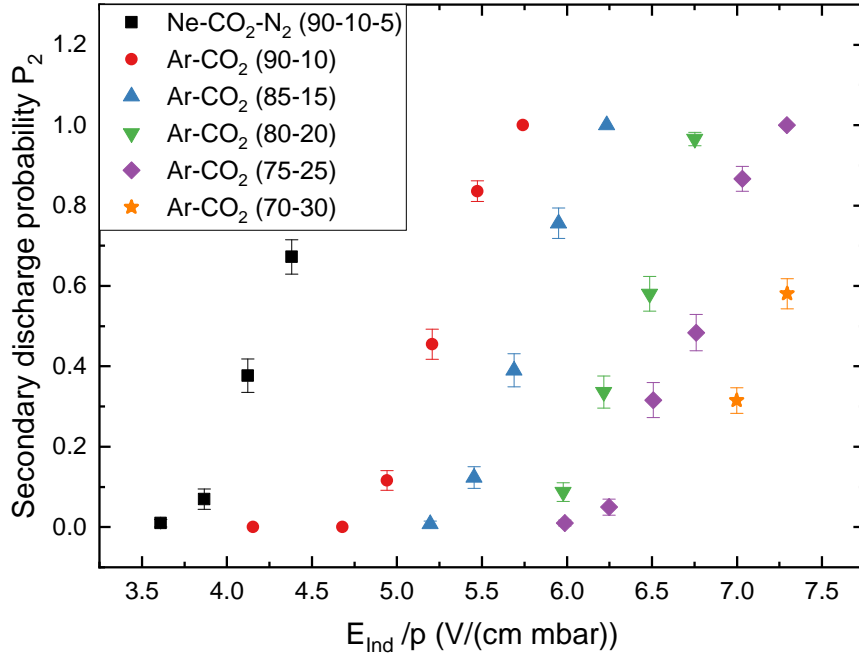


Figure 5.40: Secondary discharge probability P_2 as a function of E_{Ind}/p for different gas mixtures. The setup is biased without a decoupling resistor.

For all argon-based gas mixtures, the (distributions of the) time between primary and secondary discharge relative to their onset field is comparable (Fig. 5.41). Histograms of the time distributions can also be found in C.5. At the induction field where secondary discharges start to appear, they take about $20 \mu\text{s}$ on average to occur. With increasing field, the times decrease with the same dependency on E_{Ind} . For Ne-CO₂-N₂ (90-10-5), only a small number of waveforms could be recorded to analyse t_2 . While a different time distribution, with a pronounced peak at significantly smaller times, can be seen in neon with respect to argon, more statistics are needed for a quantitative comparison. In previous studies [36], the average time in Ne-CO₂-N₂ (90-10-5) in the transfer field was found to be smaller than $10 \mu\text{s}$, whereas it was about $20 \mu\text{s}$ for Ar-CO₂ (90-10).

5.9.2 Further investigations

Following the previously obtained knowledge on secondary discharges, an investigation on the influence of the gas properties has been started. The onset field for secondary discharges in different gas mixtures has been determined in the scope of this thesis (Sec. 5.9.1). Based on the obtained values for E_{Ind}^{On} , further measurements have been conducted in [48]. For completeness, these measurements will be presented here and discussed in Section 5.9.3.

During electron amplification in the GEM, and a subsequent primary discharge,

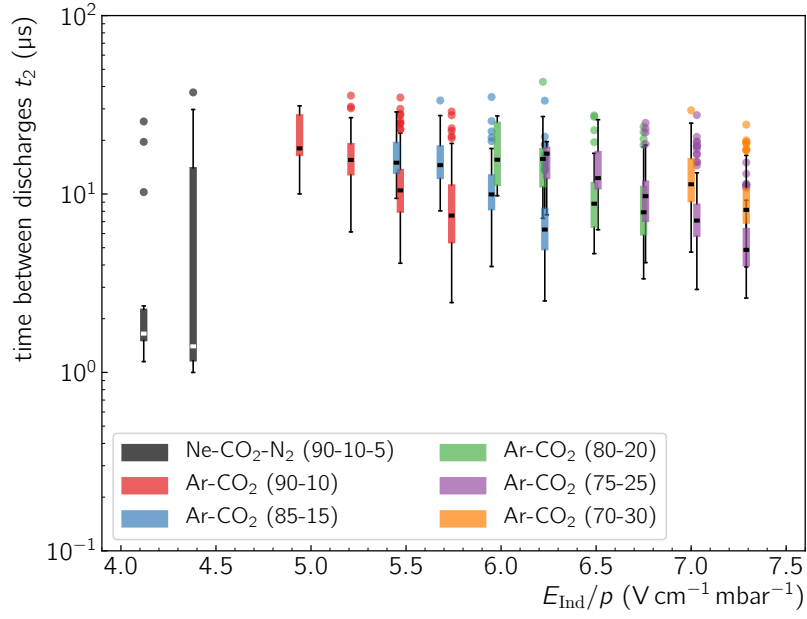


Figure 5.41: Time between primary and secondary discharge t_2 as a function of E_{Ind}/p for different gas mixtures. Only a small number of waveforms was recorded for Ne-CO₂-N₂ (90-10-5).

a large amount of electrons is created, which then drift through the induction gap. Although the electric fields at E_{Ind}^{On} are not strong enough to initiate gas amplification for the bulk of the electrons, a fraction of them might carry enough energy to ionize or excite the gas. Simulations using Magboltz [67] are performed to obtain the electron energy distributions in a homogeneous electric field of strength E_{Ind}^{On} for the different gas mixtures (Fig. 5.42). The first and second excited states of Ar (CO₂) are at 11.3 eV and 11.6 eV (7.9 eV and 10.5 eV), and the ionization potentials of Ar and CO₂ are at 11.8 eV and 13.7 eV, respectively. According to the simulations, a significant fraction of electrons carry enough energy to excite and ionise the gas.

However, the simulations only give the relative amount of electrons that can excite or ionize the gas. An additional measurement is needed to obtain an absolute number of electrons produced during the primary discharge. Hence, additional measurements are carried out, where the setup, which is described in Sec. 5.1, is used, except that the anode plane is read out by a standard oscilloscope probe instead. Waveforms are recorded for several Ar-CO₂ gas mixtures at different values of the electric field, where $P_2 > 0$. Figure 5.43 displays an exemplary waveform. The current $I(t)$ in the readout circuit is related to the derivative of the voltage $V(t)$. By defining an effective charge, which is obtained by integrating $I(t)$ until the time where the initial current decreases down to $1/e$ of its original value, one is able to compare the

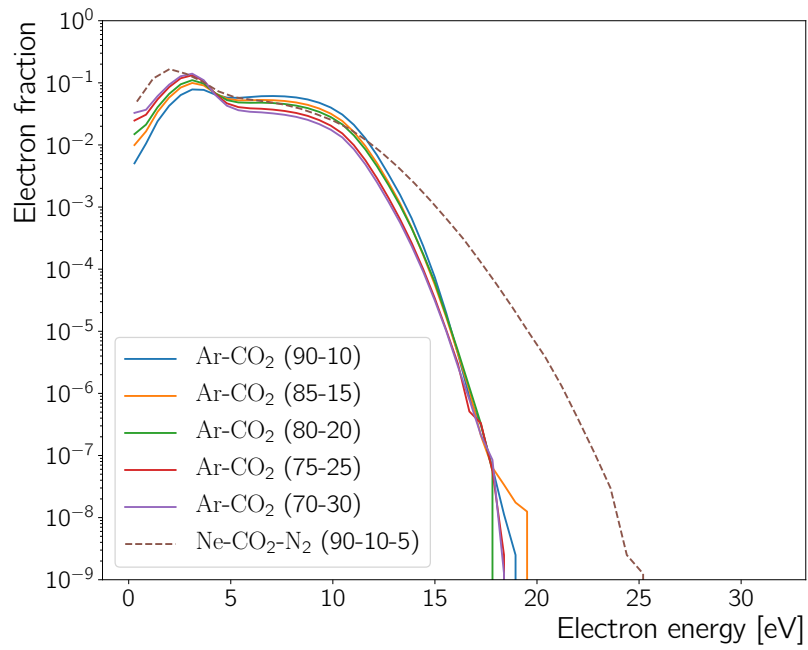


Figure 5.42: Magboltz simulation of the normalized distribution of the energy of electrons in a homogeneous electric field at E_{Ind}^{On} for different gas mixtures. A pressure of 953.3 mbar and a temperature of 23 °C is used [48].

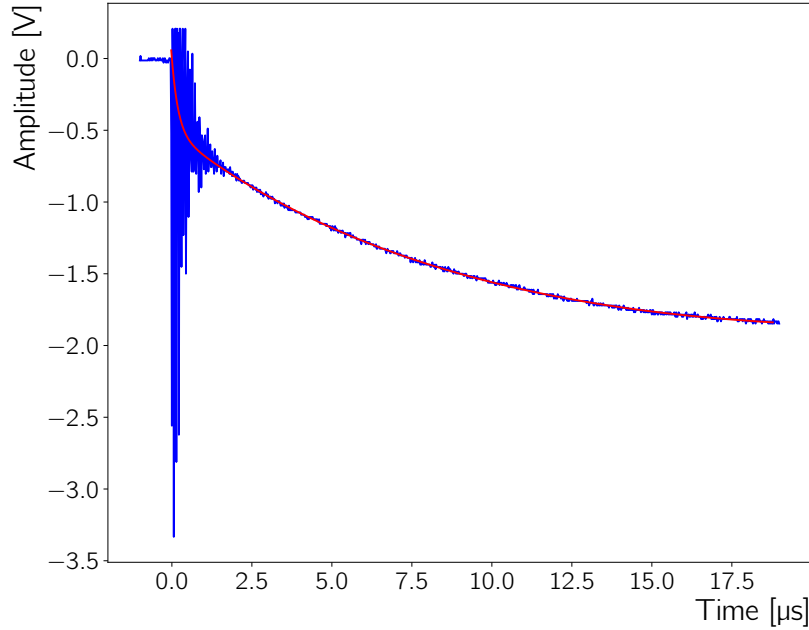


Figure 5.43: Measurement of the anode potential after a primary discharge ($t = 0 \mu\text{s}$) using a commercial oscilloscope probe (blue), and a fit to the measurement (red) [48].

different measurements with each other¹⁰. The obtained effective charge is shown in Figure 5.44a. In order to provide better comparability, the effective charge is shown as a function of P_2 instead of the E_{Ind} . With increasing CO_2 fraction, slightly less electrons are available (shortly) after the primary discharge. Nonetheless, the total number of electrons stays at the same order of magnitude. Combining the measurements of the effective charge and the simulations of the electron energy distribution, one can obtain an effective number of electrons above certain electron energies ε at the onset field (Fig. 5.44b). This measurement shows that a certain amount of charge is created during the primary discharge in a given gas mixture, with the amount being slightly dependent on the exact gas composition.

The drift velocity of ions in the gas mixtures investigated here, calculated from the ion mobilities in [68], is shown in Fig. 5.45. With rising CO_2 content, the ion drift velocity increases. As a consequence, the ions in the gas carry more energy.

¹⁰An integration of the full current is not possible, since secondary discharges can occur before the current dies off.

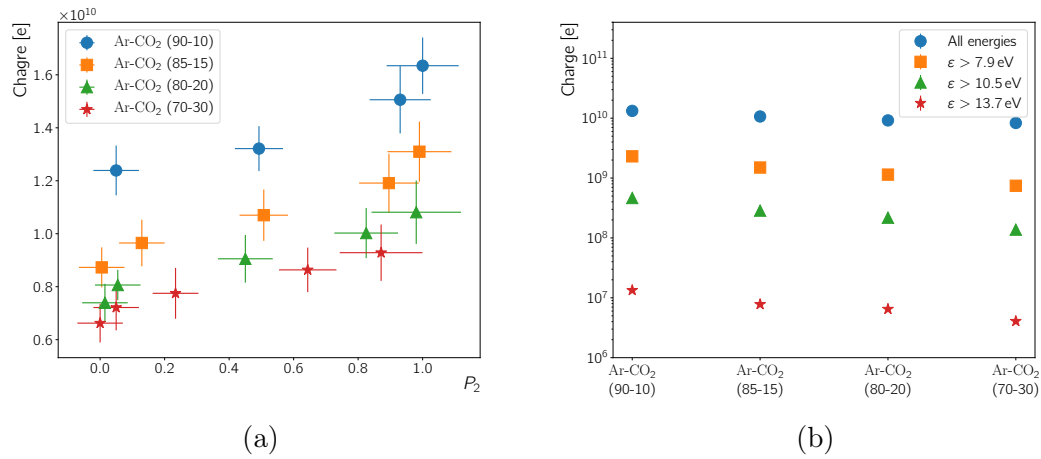


Figure 5.44: (a) Measurement of the effective charge collected in the anode after the primary discharge in different Ar-CO₂ gas mixtures. The charge is plotted as a function of P_2 in order to provide better comparability of the measurements. (b) Effective number of electrons above different energy levels produced after the primary discharge at the onset field of different gases. Both figures were taken from [48].

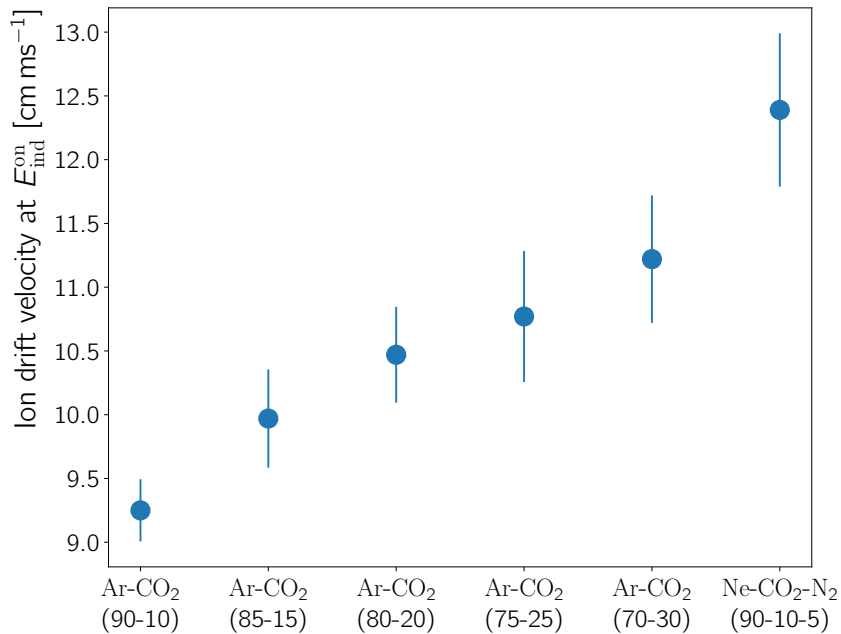


Figure 5.45: Calculated ion drift velocity at the secondary discharge onset field for different gas mixtures [48].

5.9.3 Possible mechanism to explain secondary discharges and discussion

The fact that less charge is available after a primary discharge in gases with higher CO_2 concentration, while ions carry more energy, points to a heating of the electrode, which serves as a cathode in the discharging gap, as a possible reason for the secondary discharge to develop. The mechanism proposed in [48] is first discussed for the standard direction of the electric field, where electrons drift from the GEM bottom electrode (which, in this case, serves as the cathode in the induction field) towards the readout anode: During the primary discharge, the GEM is object to a certain heat load created by the spark, while a large amount of electron-ion pairs is created. The electrons drift into the gas volume, where a fraction of them excite and ionize the gas. De-excitation of atoms or molecules releases (infra-red) radiation, which impinges on the heated GEM bottom electrode. Due to the already high temperatures, enough energy is transferred to release more electrons from the cathode. Additionally, a part of the ions, which were created during the primary discharge, bombard the GEM bottom electrode, due to electrostatic repulsion. As a consequence, the ions eject more electrons from the material, while simultaneously heating the material. A next “wave” of electrons is created, which can again ionize and excite the gas. Eventually, a self-sustained process is started. The environment created during a primary discharge seems to give origin to the secondary discharge. The previous measurements suggest that a characteristic number of 10^{10} electrons after the primary discharge is necessary, while also a certain electric field strength needs to be present.

As was shown in Sec. 5.7, when the electric field is reversed, secondary discharges appear at similar field strengths as with the standard direction. However, the rise of P_2 is slower. In this case, the ion cloud of the primary discharge drifts towards the readout (anode) plane, which now acts as the cathode, while electrons drift towards GEM bottom. Before, it was concluded that, since the time until a secondary discharge occurs decreases faster with increasing electric field than the average ion drift velocity increases, ions crossing the gap cannot be the sole reason for the secondary discharge. However, the sheer amount of ions after the primary discharge might create a sufficient electrostatic repulsion to give some ions a significant boost in velocity towards the readout plane. The fastest of these ions could be fast enough to impinge on the anode material, which heats it up, and initiates the secondary discharge mechanism as it is described above. In addition, photons from the primary discharge are absorbed by the anode material (underneath the GEM hole that discharged) immediately after the primary discharge. The material heats up, and might also release a substantial amount of electrons from the material, which can then start the process. Moreover, electrons drift towards the GEM bottom electrode. When they approach the ion cloud, they will be accelerated towards the it, which might lead to excitation and ionisation processes close to the space charge.

Electrons from both sources, (thermionic) emission from the readout material and acceleration towards the ion cloud, could contribute to the development of

the breakdown of the gap. The slightly different (initiation of the) mechanism could explain the different dependency of the secondary discharge probability on the strength of the induction field (cf. Fig. 5.19) in the standard and reversed direction. Photographs of secondary discharges in the reversed induction field, which show that after the discharge, a long-lasting glow of the readout electrode (cathode) is present [51], further support the idea that the heating of the cathode is involved in creating the secondary discharge.

However, further studies are needed in order to investigate the compatibility of the previously proposed mechanism with the reversed electric field. In Section 5.7, secondary discharges in the reversed field were found to occur as fast as ~ 200 ns after the primary discharge. It is unclear whether the ions are fast enough to initiate the “heating of the cathode.” One possibility to understand the secondary discharge in the reversed field better is to simulate the movement of the ion cloud, which is created in the primary discharge, through the gap. Comparing the arrival time of the (fastest) ions on the anode plane with the measured times between primary and secondary discharge could provide further insights on the topic. Measurements of the current at the anode plane could function as a cross-check of the simulations and might yield new information. One could also identify current spikes, which could favour one of the mentioned sources of electron emission. For example, electron emission from the readout due to photons would correspond to a current spike at $t \sim 0$ s, whereas the majority of ions would only arrive after a few microseconds.

6 Summary

In this thesis, a detector with a single $10 \times 10 \text{ cm}^2$ GEM has been used to study secondary discharges in the induction gap between the GEM and the readout anode. Either a GEM with copper electrodes, produced with the double-mask technique, or a single-mask GEM with aluminium electrodes has been employed. Discharges have been voluntarily induced using alpha particles and a high voltage across the GEM. The potentials of the GEM top and bottom electrodes have been monitored with high voltage probes, allowing to examine the potential evolution of the GEM electrodes during discharges. The secondary discharge probability P_2 and the time t_2 between primary and secondary discharge have been measured for different biasing schemes and gas mixtures. A summary of the electric onset fields E_{Ind}^{On} for secondary discharges in the induction gap, defined as the field where $P_2 = 0.5$, is given in Table 6.1. The table also outlines which measurements have been used in which section of this work.

GEM	Gas mixture	E_{Ind}^{On}/p ($\text{V cm}^{-1} \text{ mbar}^{-1}$)	Used in Sec.	Comments
Cu (GEM A)	Ar-CO ₂ (90-10)	5.18 ± 0.05	5.5; 5.6	for all E_{Drift}
Al	Ar-CO ₂ (90-10)	6.05 ± 0.05	5.6; 5.7; 5.8	standard E_{Ind}
		5.75 ± 0.05	5.7	reversed E_{Ind}
		7.00 ± 0.05	5.8	$R_D = 50 \text{ k}\Omega$
		8.05 ± 0.05	5.8	$R_D = 100 \text{ k}\Omega$
Cu (GEM B)	Ar-CO ₂ (90-10)	5.20 ± 0.05	5.7; 5.9	standard E_{Ind}
		5.40 ± 0.05	5.7	reversed E_{Ind}
	Ar-CO ₂ (85-15)	5.75 ± 0.05	5.9	
	Ar-CO ₂ (80-20)	6.35 ± 0.05	5.9	
	Ar-CO ₂ (75-25)	6.75 ± 0.05	5.9	
	Ar-CO ₂ (70-30)	7.25 ± 0.05	5.9	
	Ne-CO ₂ -N ₂ (90-10-5)	4.20 ± 0.05	5.9	

Table 6.1: Summary of the measurements conducted in this thesis. Two different copper GEMs (Cu) and an aluminium GEM (Al) have been used. The onset field E_{Ind}^{On}/p has been extracted by interpolation of the data points.

Varying the drift field between the cathode and the GEM between -290 V cm^{-1} and 443 V cm^{-1} has no influence on the secondary discharge probability in the induction gap or on t_2 . Since such a variation in the drift field affects the ion extraction

efficiency from the GEM holes, it can be concluded that the ion extraction does not play a significant role in the creation of secondary discharges in the induction field.

Using a GEM with aluminium electrodes yields a 15% higher onset field for secondary discharges with respect to the copper GEM. This difference, however, is within the order of mechanical inaccuracies and could be further aggravated by the different etching techniques, with which the GEMs have been produced. The times between primary and secondary discharge are compatible with each other, indicating that t_2 does not depend on the electrode material.

Secondary discharges are also observed when reversing the induction field. Neither the onset field nor the time between primary and secondary discharge change strongly, although P_2 shows a slower rise in a reversed field when increasing $|E_{Ind}|$. Hence, the strength of the induction field drives the occurrence of secondary discharges.

The use of decoupling resistors in the GEM bottom supply path leads to a shift of the onset field to higher values by $(20.0 \pm 0.1) \text{ V cm}^{-1} \text{ mbar}^{-1} \Omega^{-1}$ in our setup. A drop of the GEM potentials, which lasts about 10 μs , after the primary discharge was found to explain the mitigating effect of decoupling resistors.

Measurements with Ar-CO₂ mixtures of different concentrations show an increase of the onset field with increasing fraction of the quencher. The time between primary and secondary discharge, with respect to the onset fields, is compatible for all gas mixtures. In Ne-CO₂-N₂ (90-10-5), the baseline gas mixture of the ALICE TPC for Run 3, secondary discharges appear at induction fields that are about 20% lower than in Ar-CO₂ (90-10), while also occurring sooner after the primary discharge. Based on these measurements, additional simulations and measurements have been conducted and described in [48]. There, a mechanism for the secondary discharge, based on the heating of the GEM during the primary discharge, is proposed: A fraction of the electrons created during the primary discharge is able to ionise and excite the gas. Due to the heat load on the GEM, ion bombardment and infra-red radiation lead to thermionic emission of further electrons from the GEM electrodes. If enough charges are available after the primary discharge in a sufficiently strong electric field, a self-sustained current is created which eventually leads to the secondary discharge. Further studies are needed to verify the compatibility of this mechanism with the evolution of secondary discharges against the direction of the electric field.

Appendices

A Supplementary plots

A.1 Normalized secondary discharge probability

The section shows the secondary discharge probability P_2 as a function of $(E_{Ind} - E_{Ind}^{On})/p$, so that differences in the slope can be compared more easily.

A.1.1 Influence of different GEM materials

Figure A.1 shows P_2 as a function of the normalized induction field for the copper and aluminium GEM. The slope of the latter is significantly smaller at high probabilities. The measurement is presented in Sec. 5.6.

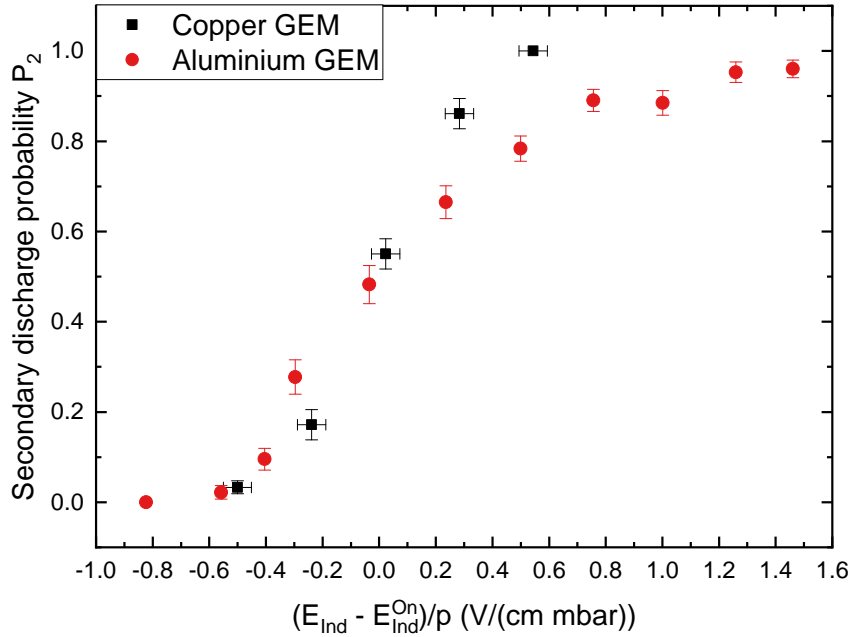


Figure A.1: Comparison of the secondary discharge probability P_2 in Ar-CO₂ (90-10) between a copper and aluminium GEM. The curves are normalized by their onset field E_{Ind}^{On} . The aluminium GEM shows a significantly different shape of the curve for higher P_2 .

A.1.2 Employing different gas mixtures

Figure A.2 shows P_2 as a function of the normalized induction field for different gas mixtures. No difference between them can be seen. The measurement is presented in Sec. 5.9.

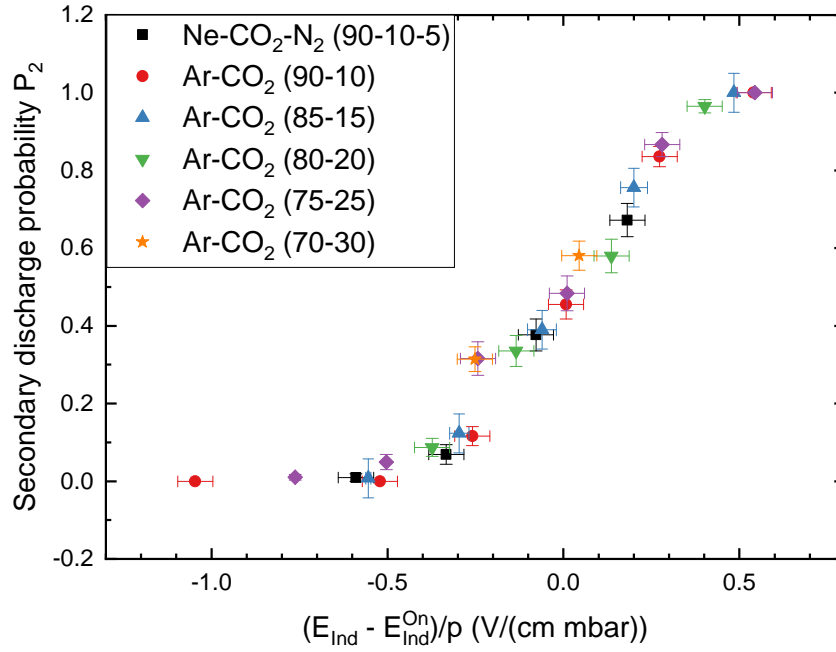


Figure A.2: Secondary discharge probability P_2 as a function of the induction field, which is normalized by the onset field for different gas mixtures. No difference between them can be seen.

A.2 Antenna signals with 200 MHz bandwidth

In this section, the signals of antennas during primary (Fig. A.3) and secondary discharges (Fig. A.4) with standard and reversed direction of the induction field are presented. An average of 20 signals is taken. In contrast to Sec. 5.7.2, a recording bandwidth of 200 MHz is used.

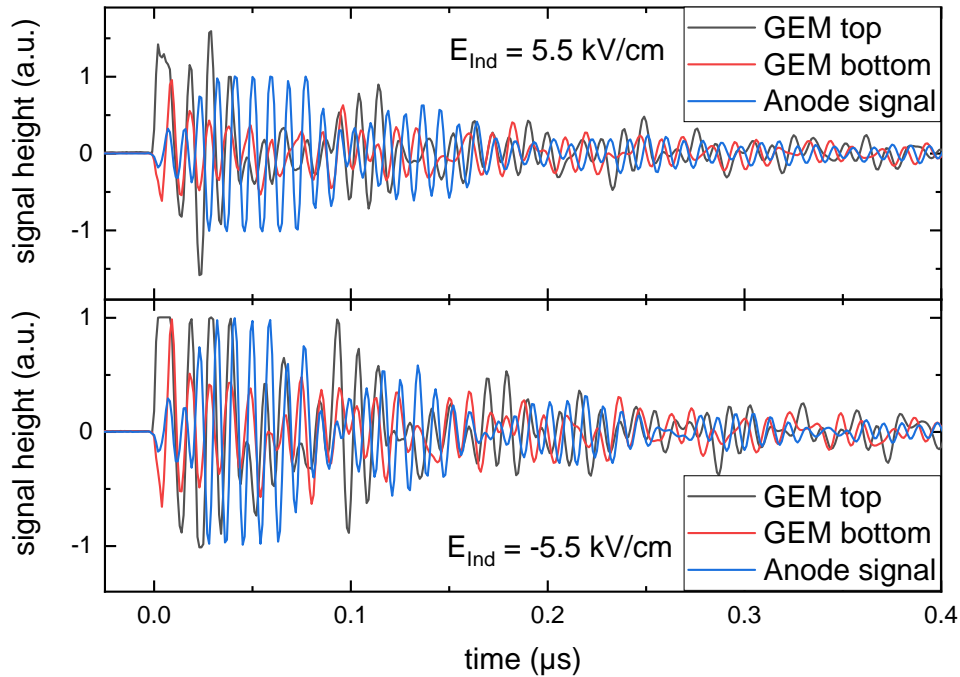


Figure A.3: Average of 20 signals recorded by antennas during a primary discharge at normal (top) and reversed induction field (bottom). The bandwidth is limited to 200 MHz.

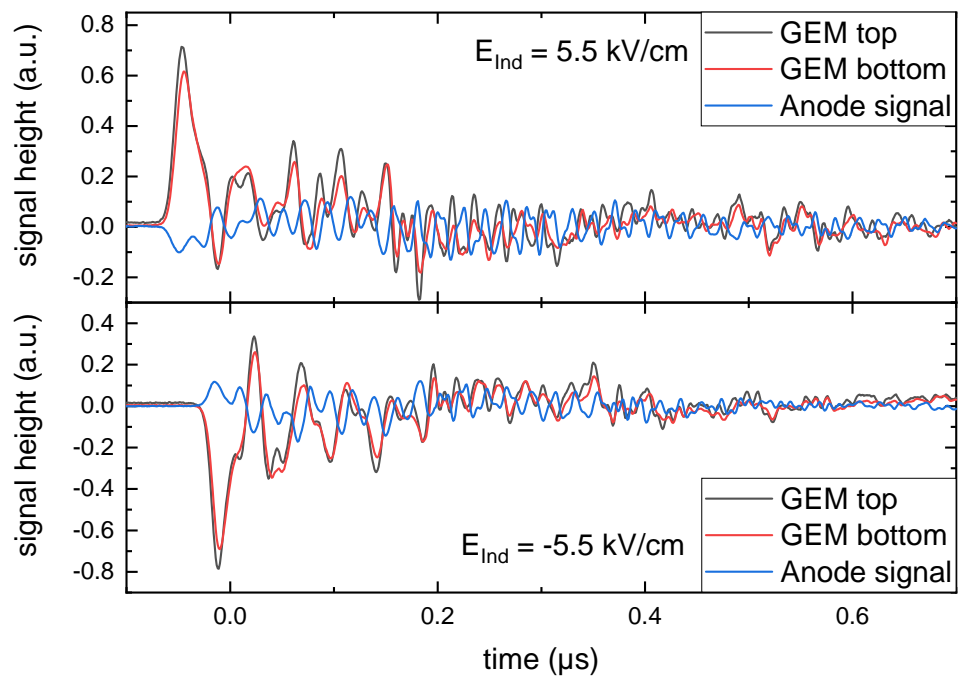


Figure A.4: Average of 20 signals recorded by antennas during a secondary discharge at normal (top) and reversed induction field (bottom). The bandwidth is limited to 200 MHz.

A.3 Time analysis software output

This section displays the time analysis used for the measurements with decoupling resistors (Sec. 5.8). Three different cases are shown when the GEM is biased with $R_D = 100\text{ k}\Omega$:

- A fast secondary discharge occurring before the potential drop, which is induced after a primary discharge (Fig. A.5).
- A slow secondary discharge occurring after the potential drop, which is induced after a primary discharge (Fig. A.6).
- Only a primary discharge occurs (Fig. A.7).

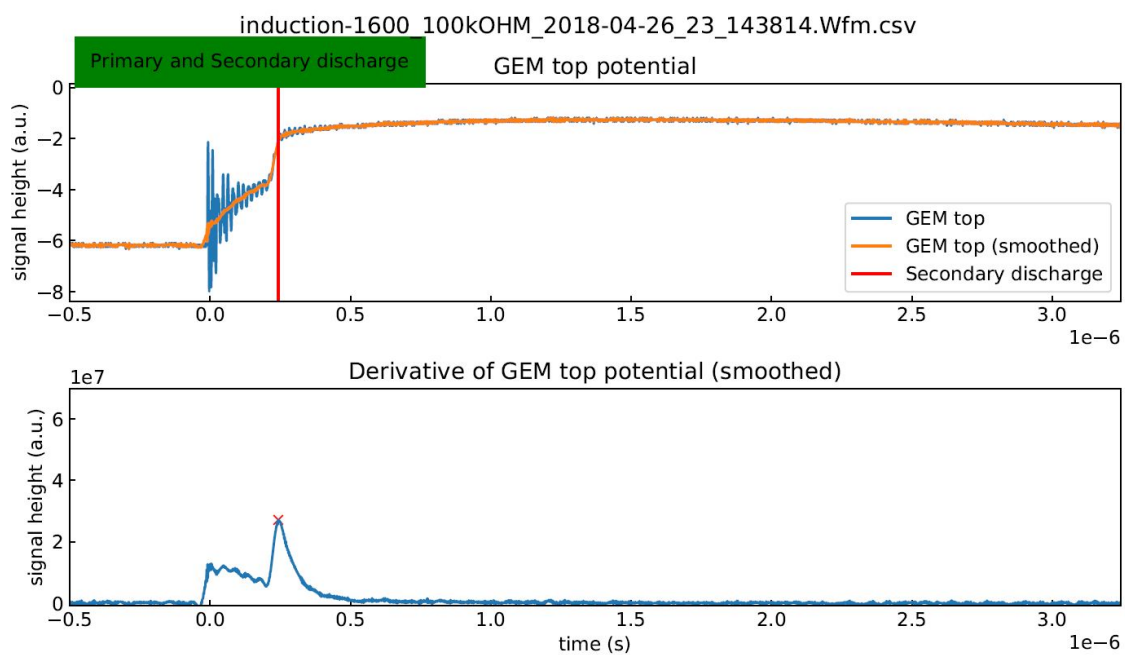


Figure A.5: Example of the output of the time analysis script, which is described in Sec. 5.8.3, for a fast secondary discharge.

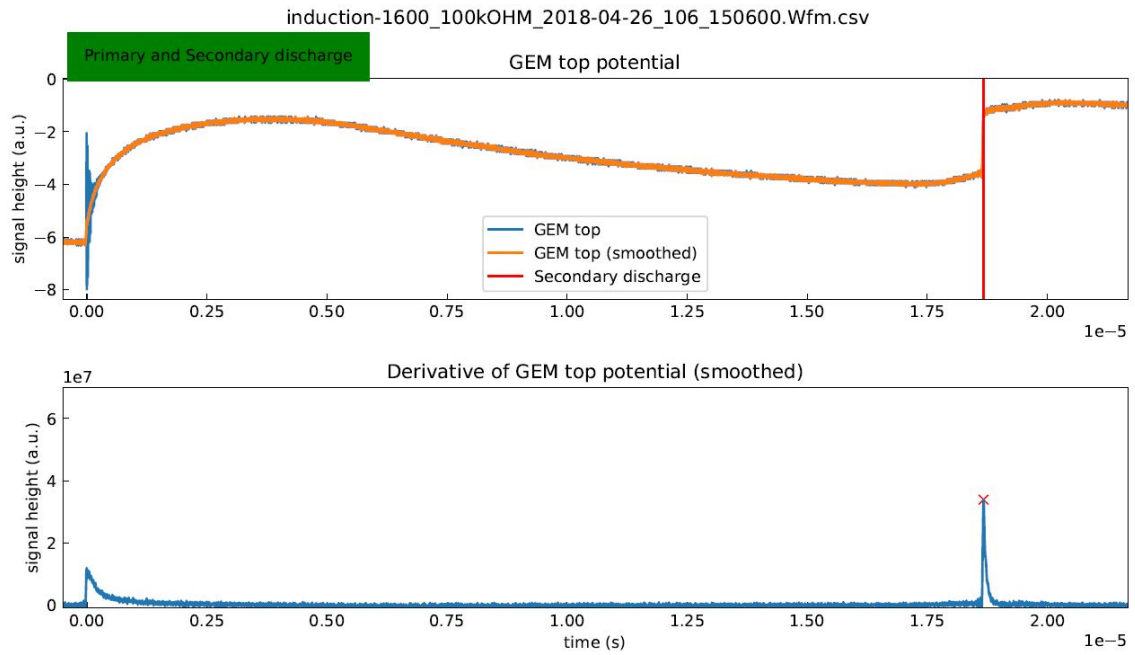


Figure A.6: Example of the output of the time analysis script, which is described in Sec. 5.8.3, for a slow secondary discharge.

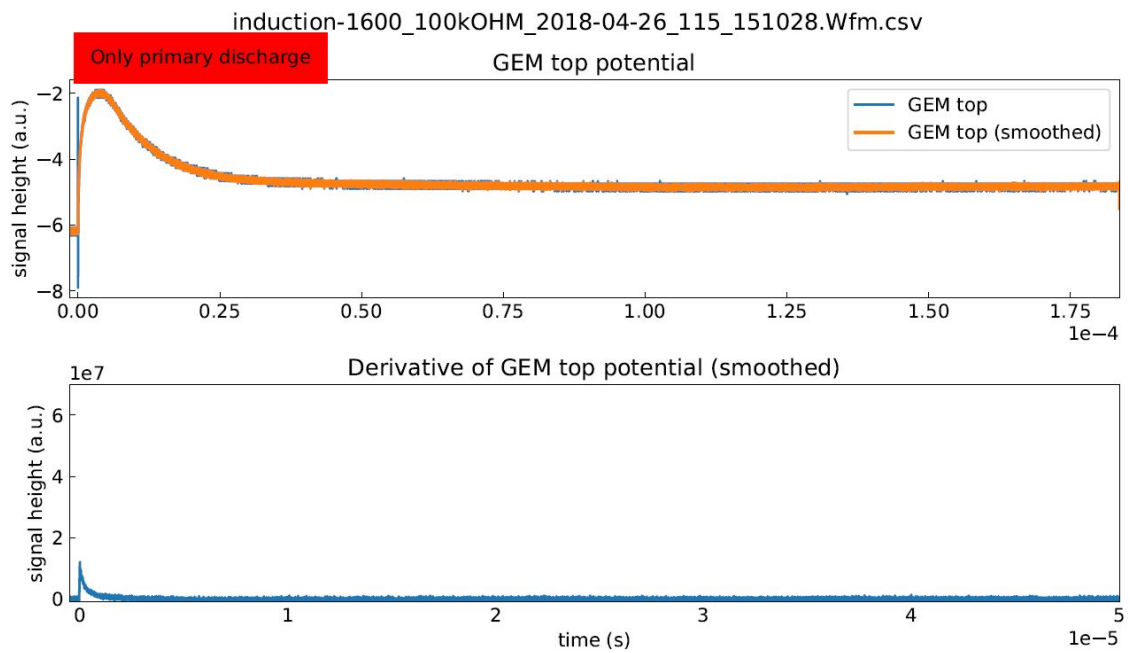


Figure A.7: Example of the output of the time analysis script, which is described in Sec. 5.8.3, for a primary discharge without a secondary discharge.

B High voltage settings and measurement data

In this chapter, the high voltage settings, environmental parameters and number of discharges for every measurement of Ch. 5 are listed.

B.1 Drift field dependence

The measurements of this section correspond to the ones presented in Sec. 5.5 and have been conducted with GEM A. For some measurements, no temperature measurement was available.

ΔU_{real} (V)	E_{Drift} (V/cm)	E_{Ind} (V/cm)	N_{prim}	N_{sec}	p (mbar)	T (°C)	H ₂ O (ppmV)	t (min)
416	442	4500	152	5	957.6	n.A.	813	20
417	442	4750	128	22	957.5	n.A.	854	20
419	445	5000	218	120	957.4	n.A.	845	20
414	443	5250	108	93	957.4	n.A.	848	20
414	442	5500	94	94	957.6	n.A.	847	20

Table B.1: $E_{Drift} \approx 443 \text{ V cm}^{-1}$.

ΔU_{real} (V)	E_{Drift} (V/cm)	E_{Ind} (V/cm)	N_{prim}	N_{sec}	p (mbar)	T (°C)	H ₂ O (ppmV)	t (min)
419	281	4500	129	5	959.8	n.A.	1014	25
419	280	4750	145	17	959.9	n.A.	1025	30
419	281	5000	135	68	960.3	n.A.	1800	40
418	279	5250	111	109	960.3	n.A.	1800	30
417	281	5500	134	134	959.9	n.A.	1033	40

Table B.2: $E_{Drift} \approx 280 \text{ V cm}^{-1}$.

ΔU_{real} (V)	E_{Drift} (V/cm)	E_{Ind} (V/cm)	N_{prim}	N_{sec}	p (mbar)	T (°C)	H ₂ O (ppmV)	t (min)
420	137	4500	60	1	959.6	n.A.	1003	40
420	138	4750	115	19	959.3	n.A.	988	90
419	138	5000	98	56	959.2	n.A.	756	97
418	139	5250	110	109	957.2	21	758	100
418	138	5500	87	87	956.1	22	753	80

Table B.3: $E_{Drift} \approx 138 \text{ V cm}^{-1}$.

ΔU_{real} (V)	E_{Drift} (V/cm)	E_{Ind} (V/cm)	N_{prim}	N_{sec}	p (mbar)	T (°C)	H ₂ O (ppmV)	t (min)
420	-5	4500	120	18	942.8	24	1085	150
420	-5	4750	212	88	942.6	24	1117	300
419	-5	5000	101	92	944.2	24	1220	350
418	-5	5250	106	105	944.9	23	1291	365
417	-4	5500	33	33	949.0	22	736	300

Table B.4: $E_{Drift} \approx -5 \text{ V cm}^{-1}$.

ΔU_{real} (V)	E_{Drift} (V/cm)	E_{Ind} (V/cm)	N_{prim}	N_{sec}	p (mbar)	T (°C)	H ₂ O (ppmV)	t (min)
420	-297	4500	63	6	951.4	24	1032	1110
419	-290	5000	39	26	955.7	24	1058	1230

Table B.5: $E_{Drift} \approx -290 \text{ V cm}^{-1}$.

B.2 Influence of the GEM material

The measurements of this section correspond to the ones presented in Sec. 5.7. For the secondary discharge probability recorded with the copper GEM, the measurement of the drift field dependence with $E_{Drift} \approx 415 \text{ V cm}^{-1}$ (Tab. B.1) was used.

ΔU_{real} (V)	E_{Drift} (V/cm)	E_{Ind} (V/cm)	N_{prim}	N_{sec}	p (mbar)	T (°C)	H ₂ O (ppmV)	t (min)
435	434	5450	137	14	965.3	23	1014	25
427	437	5500	147	38	956.0	23	1025	30
427	437	5750	141	68	955.9	23	1800	40
426	437	6000	170	113	954.6	23	1399	60
427	437	6250	217	170	954.4	24	1424	90
427	437	6500	164	146	955.0	23	1463	80
427	437	6750	139	123	957.3	23	1369	60
426	437	7000	85	81	957.7	23	1369	45
426	437	7250	100	96	965.3	22	1453	45

Table B.6: Induction field scan with the aluminium GEM.

B.3 Influence of the direction of the induction field

The measurements of this section correspond to the ones presented in Sec. 5.7. For the standard induction field direction, the aluminium GEM measurement of Sec. B.2 is used, while the settings for the reversed field are presented here. The copper GEM B is used. Its settings for the standard field direction are documented in Tab. B.11.

ΔU_{real} (V)	E_{Drift} (V/cm)	E_{Ind} (V/cm)	N_{prim}	N_{sec}	p (mbar)	T (°C)	H ₂ O (ppmV)	t (min)
437	426	-4500	110	0	949.8	23	2008	60
437	426	-4750	112	5	950.3	23	2015	60
436	426	-5000	133	26	953.9	24	1563	60
436	426	-5250	152	52	954.1	24	1563	60
437	426	-5500	132	66	954.5	24	1649	45
438	426	-5750	179	102	954.3	24	1291	65
438	426	-6000	172	116	954.3	24	1633	65
438	426	-6250	132	96	955.0	24	1608	60
438	426	-6500	233	200	955.1	24	1542	90
438	426	-6750	139	132	954.6	23	1552	50
438	426	-7000	141	136	954.2	24	1559	60

Table B.7: Reversed induction field scan with the aluminium GEM.

ΔU_{real} (V)	E_{Drift} (V/cm)	E_{Ind} (V/cm)	N_{prim}	N_{sec}	p (mbar)	T (°C)	H ₂ O (ppmV)	t (min)
413	424	4500	134	7	974.5	24	1233	90
411	425	4750	105	24	965.4	23	1326	60
413	424	5000	100	33	965.5	22	1311	80
413	424	5250	113	59	965.1	23	1343	60
413	424	5500	114	77	966.5	22	1204	60
413	424	5750	182	151	966.1	23	1295	90
412	424	6000	107	102	972.4	24	1204	60
411	424	6250	65	65	972.7	24	1204	30

Table B.8: Reversed induction field scan with the copper GEM B.

B.4 Mitigation of secondary discharges using decoupling resistors

The measurements of this section correspond to the ones presented in Sec. 5.8 and are conducted with the aluminium GEM.

ΔU_{real} (V)	E_{Drift} (V/cm)	E_{Ind} (V/cm)	N_{prim}	N_{sec}	p (mbar)	T (°C)	H ₂ O (ppmV)	t (min)
429	436	6250	146	5	965.0	24	1001	60
429	436	6500	160	30	965.6	24	1011	60
430	436	6750	181	88	966.0	24	1010	60
429	436	7000	291	202	966.5	24	1018	120
431	435	7250	186	157	966.7	23	994	60
430	436	7500	186	167	967.9	24	1141	60
431	436	7750	237	206	966.9	24	1142	60
430	436	8000	181	165	966.2	24	1116	45

Table B.9: $R_D = 50 \text{ k}\Omega$.

ΔU_{real} (V)	E_{Drift} (V/cm)	E_{Ind} (V/cm)	N_{prim}	N_{sec}	p (mbar)	T (°C)	H ₂ O (ppmV)	t (min)
432	435	7250	202	10	968.5	23	914	60
430	436	7500	219	43	968.3	24	931	90
431	436	7750	176	83	967.9	23	903	45
430	436	8000	175	123	967.4	24	902	45
430	436	8250	177	152	966.3	24	899	45

Table B.10: $R_D = 100 \text{ k}\Omega$.

B.5 Employing different gas mixtures

The measurements of this section correspond to the ones presented in Sec. 5.9 and are conducted with the copper GEM B.

ΔU_{real} (V)	E_{Drift} (V/cm)	E_{Ind} (V/cm)	N_{prim}	N_{sec}	p (mbar)	T (°C)	H ₂ O (ppmV)	t (min)
410	425	4000	110	0	963.0	24	1008	60
410	425	4500	112	0	961.8	24	1008	60
409	425	4750	133	20	961.3	24	1004	60
406	426	5000	152	81	960.2	24	969	90
405	427	5250	132	173	959.2	24	974	60
405	427	5500	179	147	958.1	24	969	60

Table B.11: Ar-CO₂ (90-10).

ΔU_{real} (V)	E_{Drift} (V/cm)	E_{Ind} (V/cm)	N_{prim}	N_{sec}	p (mbar)	T (°C)	H ₂ O (ppmV)	t (min)
431	418	5000	133	1	962.4	23	4040	60
431	418	5250	146	18	962.6	23	4439	60
430	418	5500	141	55	966.8	23	1262	60
429	418	5750	127	96	966.3	22	1282	80
430	418	6000	159	159	962.4	23	3730	60

Table B.12: Ar-CO₂ (85-15).

ΔU_{real} (V)	E_{Drift} (V/cm)	E_{Ind} (V/cm)	N_{prim}	N_{sec}	p (mbar)	T (°C)	H ₂ O (ppmV)	t (min)
449	429	5750	149	13	962.0	22	1121	75
450	428	6000	140	47	965.3	22	1062	75
450	429	6250	131	76	963.6	22	1055	75
449	429	6500	116	112	962.8	22	1090	75

Table B.13: Ar-CO₂ (80-20).

ΔU_{real} (V)	E_{Drift} (V/cm)	E_{Ind} (V/cm)	N_{prim}	N_{sec}	p (mbar)	T (°C)	H ₂ O (ppmV)	t (min)
473	420	5750	196	2	960.3	23	1359	75
472	421	6000	121	6	960.5	23	1363	120
471	421	6250	114	36	960.5	23	1297	60
471	421	6500	124	60	961.5	23	1321	120
471	421	6750	120	104	960.1	23	1275	80
470	421	7000	72	72	959.7	23	1360	60

Table B.14: Ar-CO₂ (75-25).

ΔU_{real} (V)	E_{Drift} (V/cm)	E_{Ind} (V/cm)	N_{prim}	N_{sec}	p (mbar)	T (°C)	H ₂ O (ppmV)	t (min)
492	439	6750	213	67	964.5	23	1026	120
491	439	7000	174	101	959.6	23	891	120

Table B.15: Ar-CO₂ (70-30).

ΔU_{real} (V)	E_{Drift} (V/cm)	E_{Ind} (V/cm)	N_{prim}	N_{sec}	p (mbar)	T (°C)	H ₂ O (ppmV)	t (min)
465	434	3500	104	1	969.4	23	1210	60
464	434	3750	101	7	969.7	23	1154	60
465	434	4000	138	52	970.5	23	1192	60
463	434	4250	119	80	970.0	24	1181	60

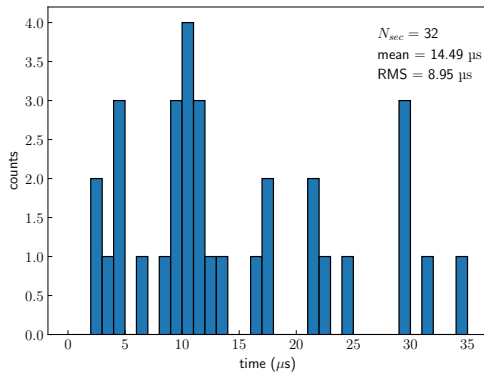
Table B.16: Ne-CO₂-N₂ (90-10-5).

C Time distribution of secondary discharges

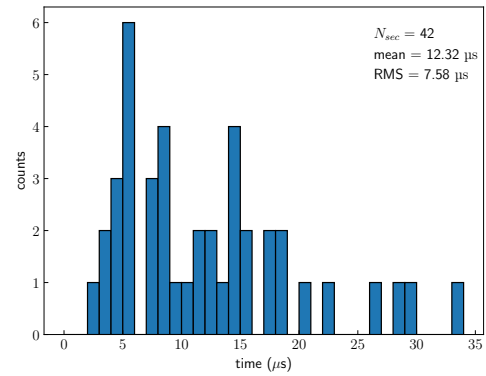
In this chapter, the distributions of the time between primary and secondary discharge for all measurements are displayed in histograms with uniform bin size of 1 μs .

C.1 Drift field dependence

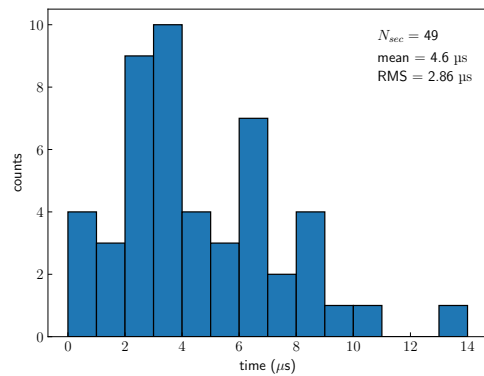
The measurements of this section correspond to the ones presented in Sec. 5.5.



(a) $E_{Ind} = 5 \text{ kV cm}^{-1}$.

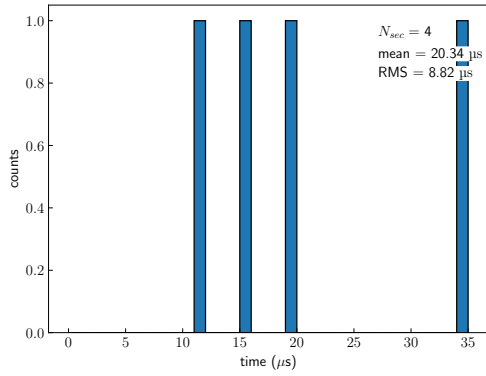


(b) $E_{Ind} = 5.25 \text{ kV cm}^{-1}$.

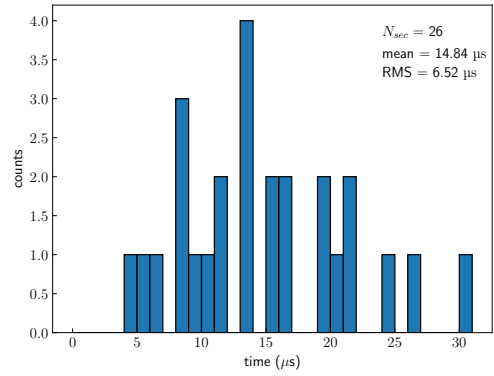


(c) $E_{Ind} = 5.5 \text{ kV cm}^{-1}$.

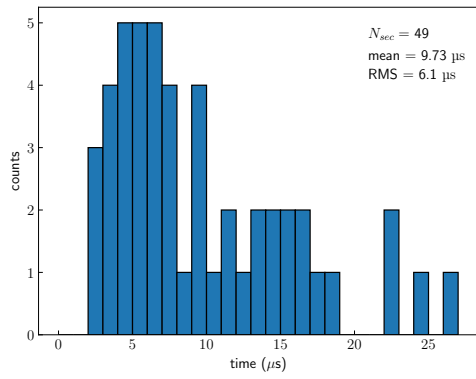
Figure C.1: Distributions of the time between primary and secondary discharge at $E_{Drift} = 443 \text{ V cm}^{-1}$.



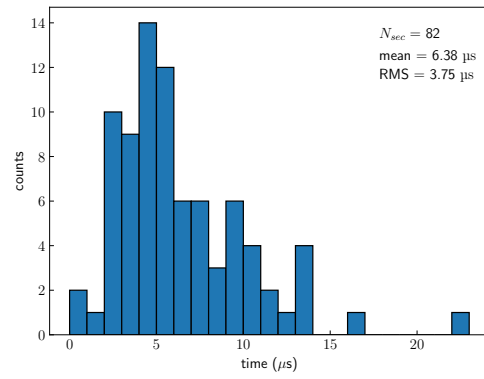
(a) $E_{Ind} = 4.75 \text{ kV cm}^{-1}$.



(b) $E_{Ind} = 5 \text{ kV cm}^{-1}$.

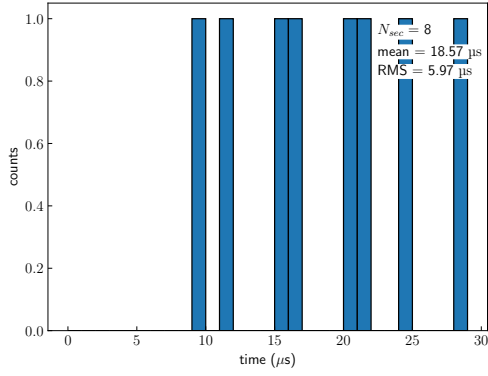


(c) $E_{Ind} = 5.25 \text{ kV cm}^{-1}$.

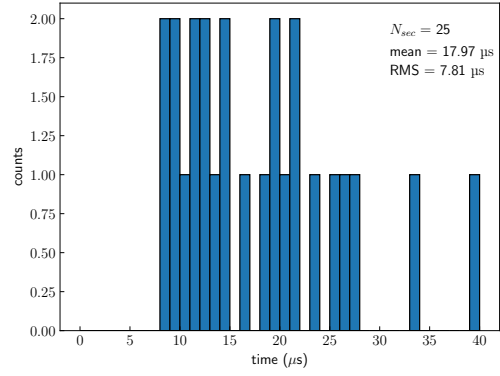


(d) $E_{Ind} = 5.5 \text{ kV cm}^{-1}$.

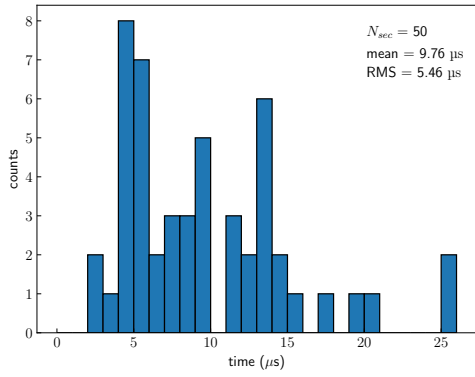
Figure C.2: Distributions of the time between primary and secondary discharge at $E_{Drift} = 280 \text{ V cm}^{-1}$.



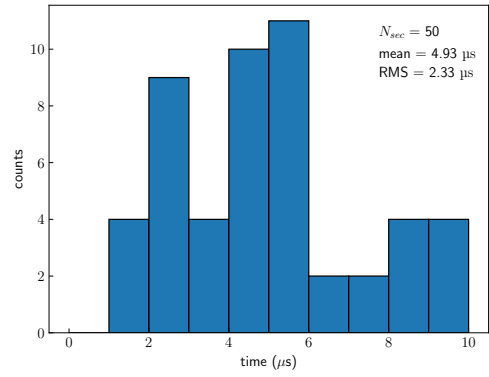
(a) $E_{Ind} = 4.75 \text{ kV cm}^{-1}$.



(b) $E_{Ind} = 5 \text{ kV cm}^{-1}$.

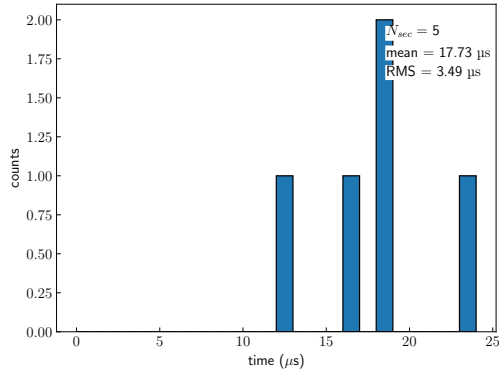


(c) $E_{Ind} = 5.25 \text{ kV cm}^{-1}$.

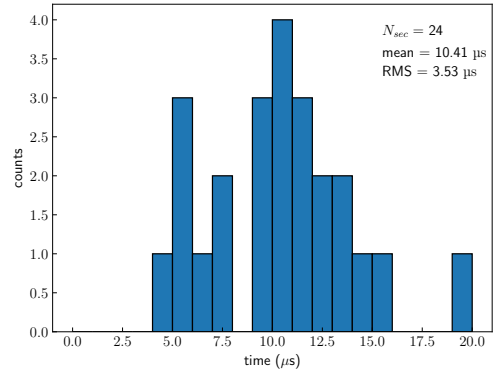


(d) $E_{Ind} = 5.5 \text{ kV cm}^{-1}$.

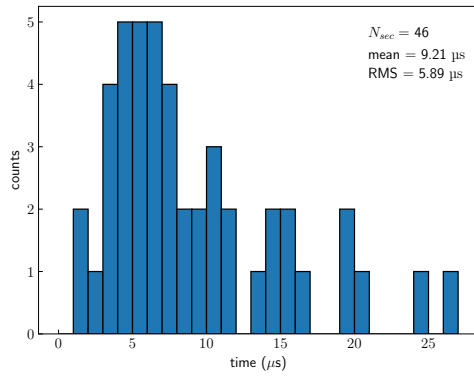
Figure C.3: Distributions of the time between primary and secondary discharge at $E_{Drift} = 138 \text{ V cm}^{-1}$.



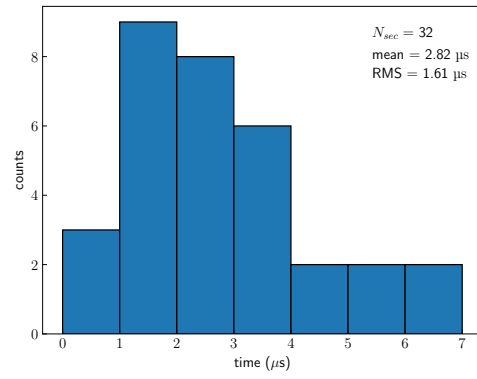
(a) $E_{Ind} = 4.5 \text{ kV cm}^{-1}$.



(b) $E_{Ind} = 4.75 \text{ kV cm}^{-1}$.

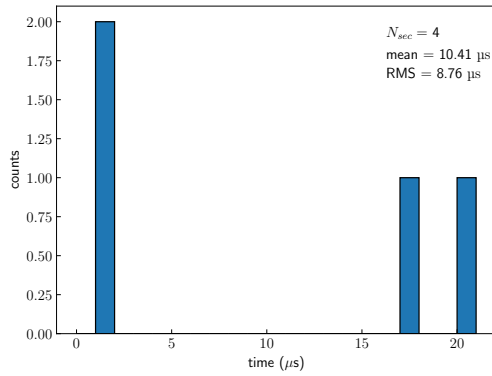


(c) $E_{Ind} = 5 \text{ kV cm}^{-1}$.

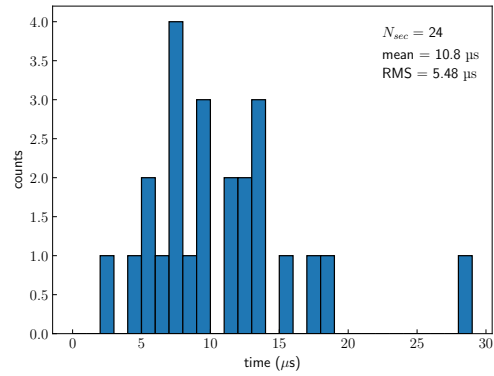


(d) $E_{Ind} = 5.5 \text{ kV cm}^{-1}$.

Figure C.4: Distributions of the time between primary and secondary discharge at $E_{Drift} = -5 \text{ V cm}^{-1}$.



(a) $E_{Ind} = 4.75 \text{ kV cm}^{-1}$.

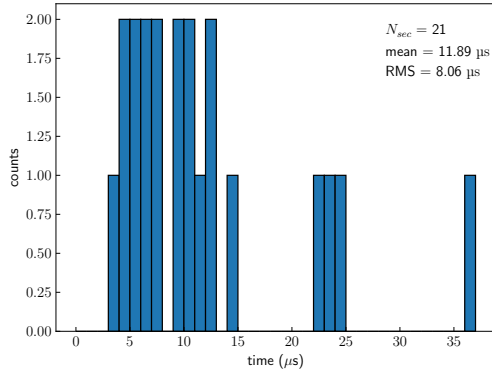


(b) $E_{Ind} = 5 \text{ kV cm}^{-1}$.

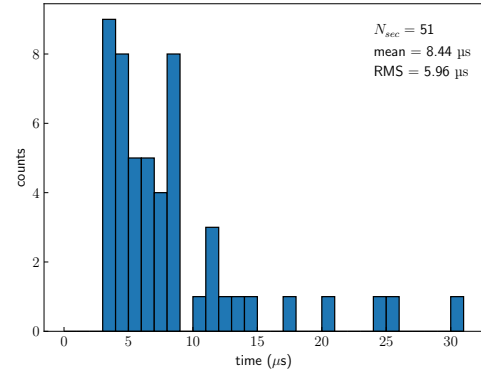
Figure C.5: Distributions of the time between primary and secondary discharge at $E_{Drift} = -290 \text{ V cm}^{-1}$.

C.2 Influence of the GEM material

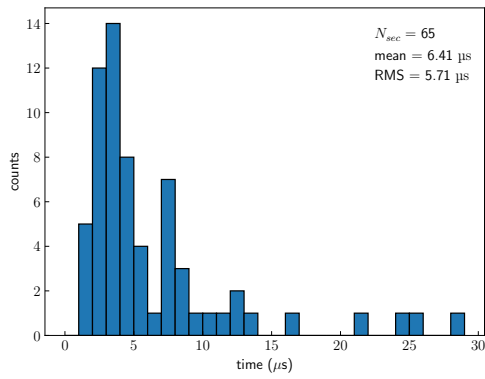
The measurements of this section correspond to the ones with the aluminium GEM in Sec. 5.6. The times with the copper GEM are taken from Fig. C.11.



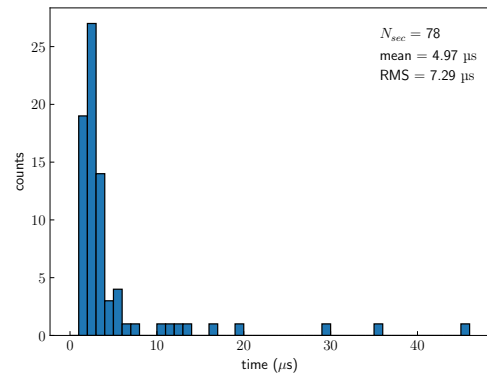
(a) $E_{Ind} = 5.5 \text{ kV cm}^{-1}$.



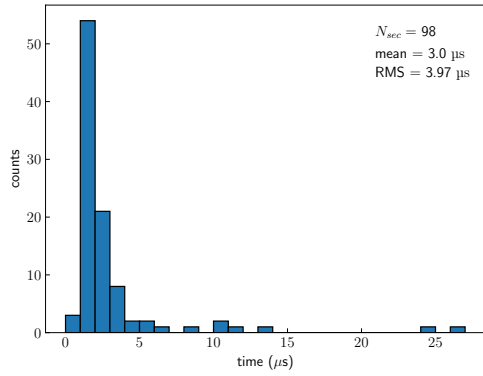
(b) $E_{Ind} = 5.75 \text{ kV cm}^{-1}$.



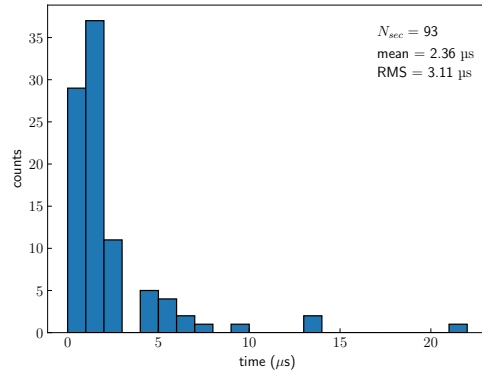
(c) $E_{Ind} = 6 \text{ kV cm}^{-1}$.



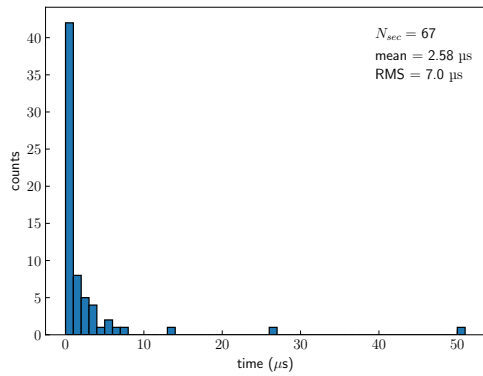
(d) $E_{Ind} = 6.25 \text{ kV cm}^{-1}$.



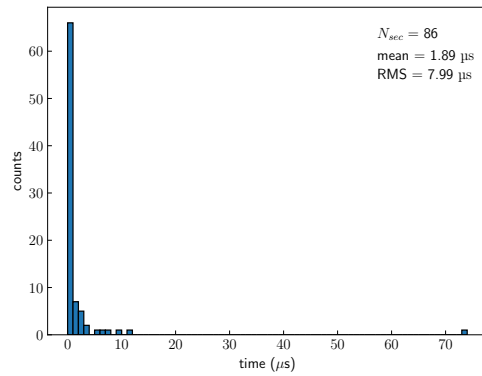
(e) $E_{Ind} = 6.5 \text{ kV cm}^{-1}$.



(f) $E_{Ind} = 6.75 \text{ kV cm}^{-1}$.



(g) $E_{Ind} = 7 \text{ kV cm}^{-1}$.

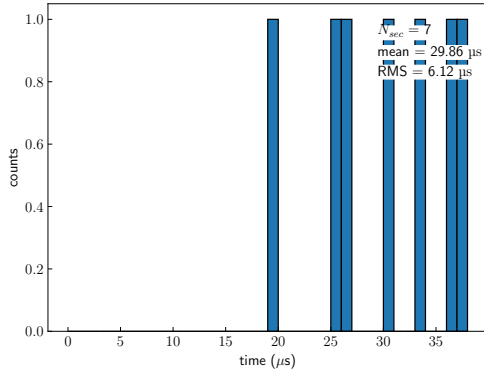


(h) $E_{Ind} = 7.25 \text{ kV cm}^{-1}$.

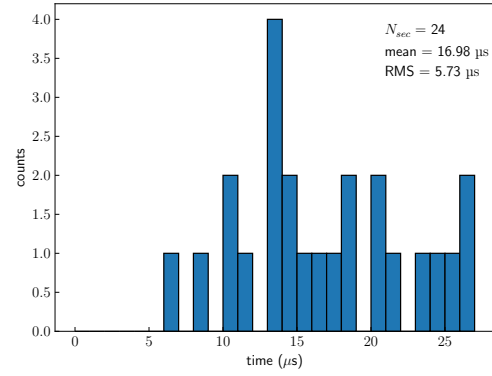
Figure C.6: Distributions of the time between primary and secondary discharge with the aluminium GEM.

C.3 Influence of the direction of the induction field

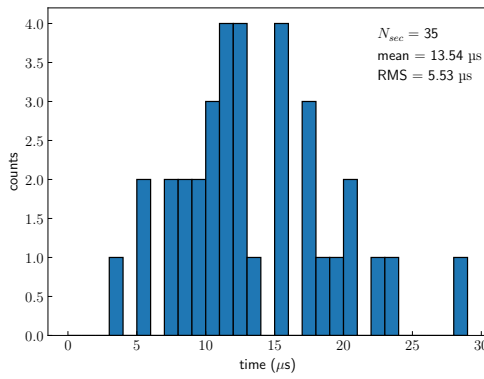
The measurements of this section correspond to the ones presented with reversed induction field in Sec. 5.7. For the standard field direction, see Sec. C.2.



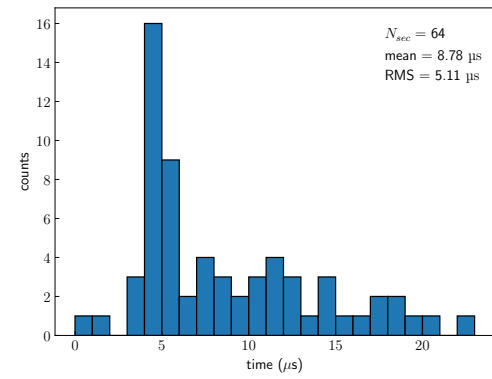
(a) $E_{Ind} = -4.5 \text{ kV cm}^{-1}$.



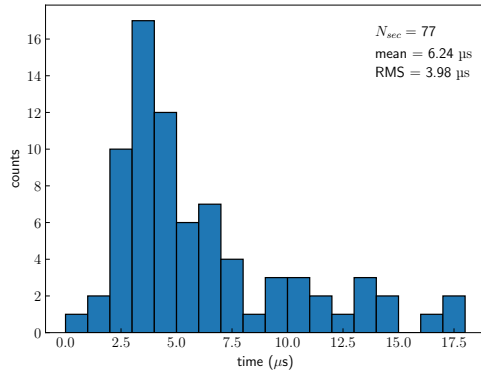
(b) $E_{Ind} = -4.75 \text{ kV cm}^{-1}$.



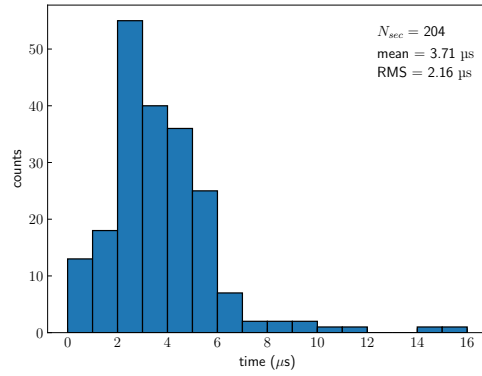
(c) $E_{Ind} = -5 \text{ kV cm}^{-1}$.



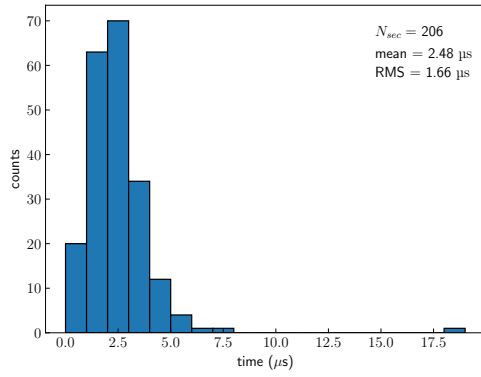
(d) $E_{Ind} = -5.25 \text{ kV cm}^{-1}$.



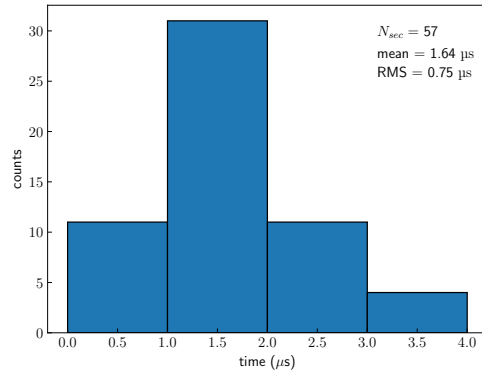
(e) $E_{Ind} = -5.5 \text{ kV cm}^{-1}$.



(f) $E_{Ind} = -5.75 \text{ kV cm}^{-1}$.

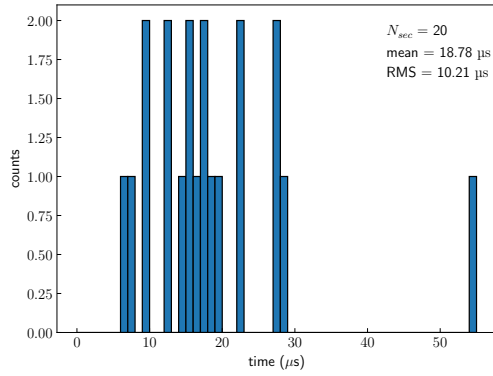


(g) $E_{Ind} = -6 \text{ kV cm}^{-1}$.

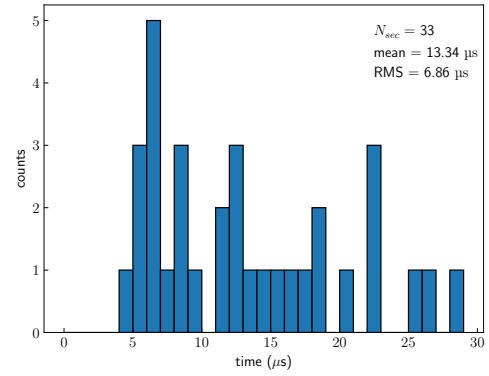


(h) $E_{Ind} = -6.25 \text{ kV cm}^{-1}$.

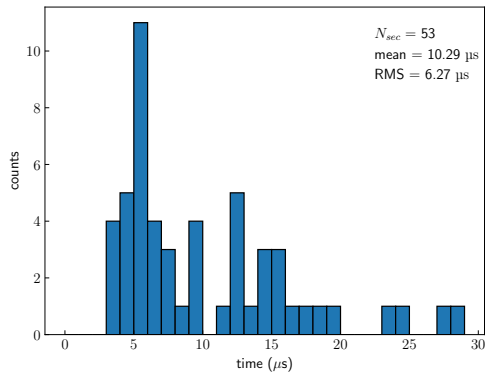
Figure C.7: Distributions of the time between primary and secondary discharge with the copper GEM and reversed induction field.



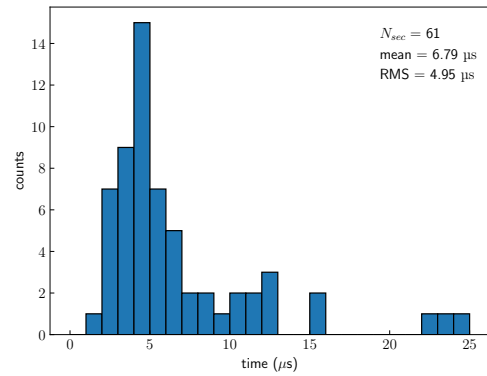
(a) $E_{Ind} = -5 \text{ kV cm}^{-1}$.



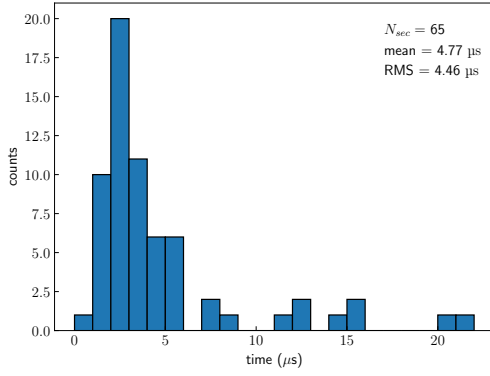
(b) $E_{Ind} = -5.25 \text{ kV cm}^{-1}$.



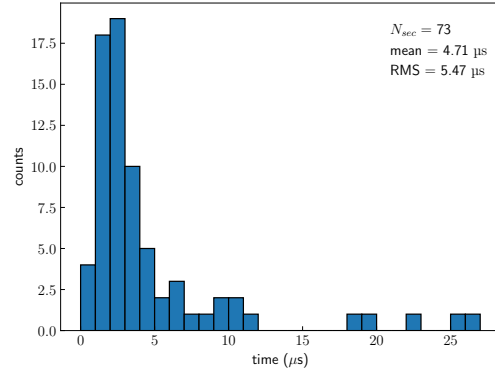
(c) $E_{Ind} = -5.5 \text{ kV cm}^{-1}$.



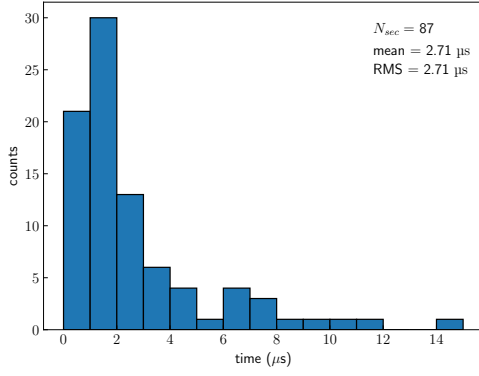
(d) $E_{Ind} = -5.75 \text{ kV cm}^{-1}$.



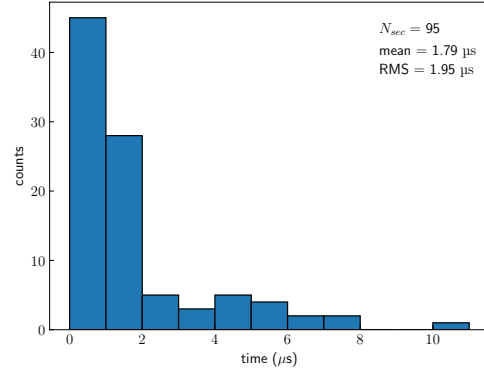
(e) $E_{Ind} = -6 \text{ kV cm}^{-1}$.



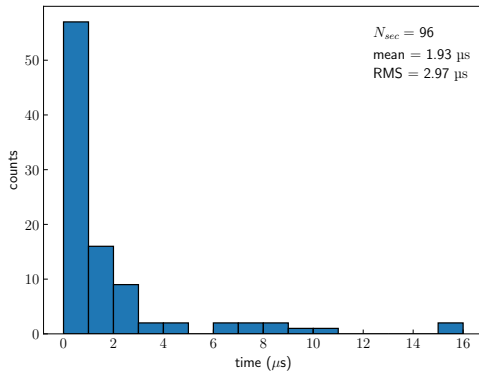
(f) $E_{Ind} = -6.25 \text{ kV cm}^{-1}$.



(g) $E_{Ind} = -6.5 \text{ kV cm}^{-1}$.



(h) $E_{Ind} = -6.75 \text{ kV cm}^{-1}$.

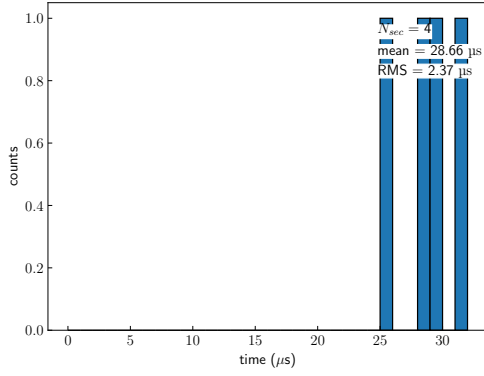


(i) $E_{Ind} = -7 \text{ kV cm}^{-1}$.

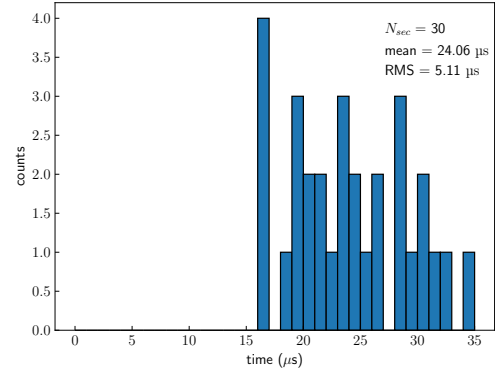
Figure C.8: Distributions of the time between primary and secondary discharge with the aluminium GEM and reversed induction field.

C.4 Mitigation of secondary discharges using decoupling resistors

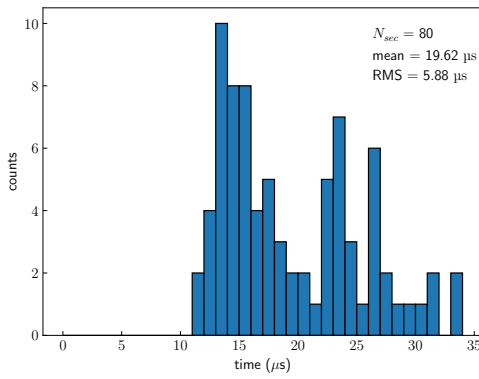
The measurements of this section correspond to the ones presented in Sec. 5.8.



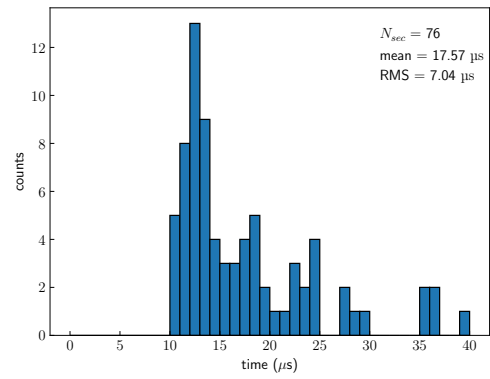
(a) $E_{Ind} = -6.25 \text{ kV cm}^{-1}$.



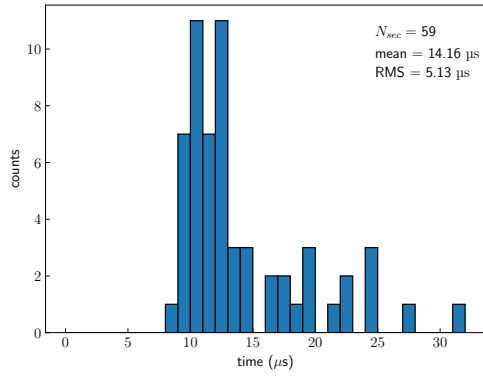
(b) $E_{Ind} = -6.5 \text{ kV cm}^{-1}$.



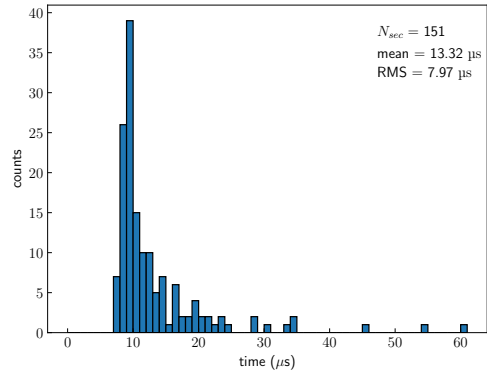
(c) $E_{Ind} = -6.75 \text{ kV cm}^{-1}$.



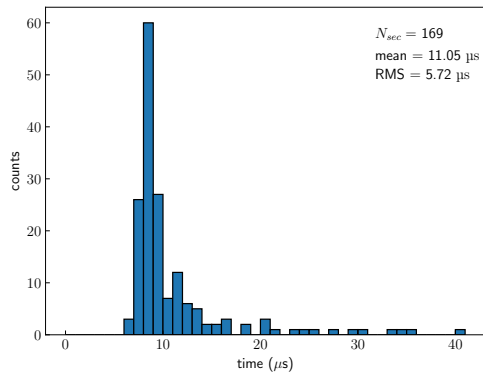
(d) $E_{Ind} = -7 \text{ kV cm}^{-1}$.



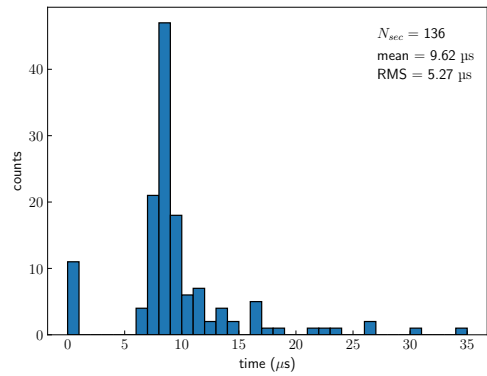
(e) $E_{Ind} = -7.25 \text{ kV cm}^{-1}$.



(f) $E_{Ind} = -7.5 \text{ kV cm}^{-1}$.

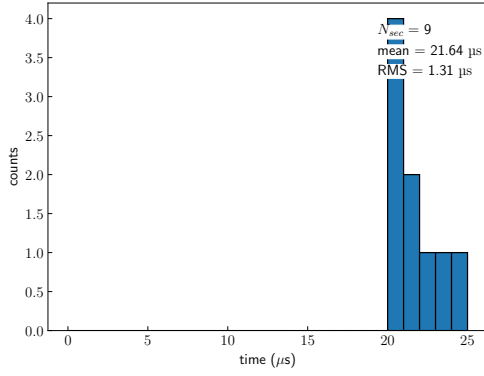


(g) $E_{Ind} = -7.75 \text{ kV cm}^{-1}$.

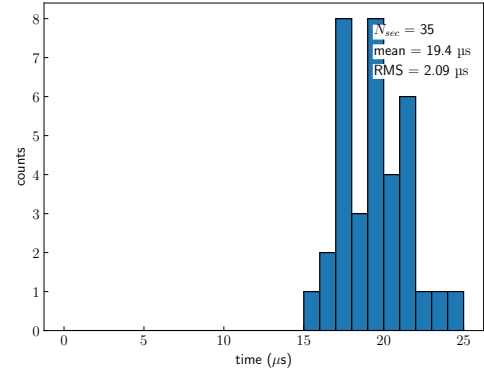


(h) $E_{Ind} = -8 \text{ kV cm}^{-1}$.

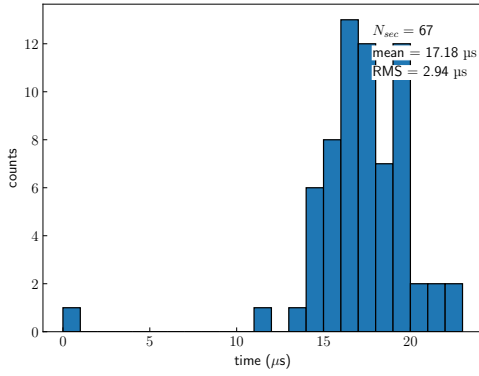
Figure C.9: Distributions of the time between primary and secondary discharge with the aluminium GEM and $R_D = 50 \text{ k}\Omega$.



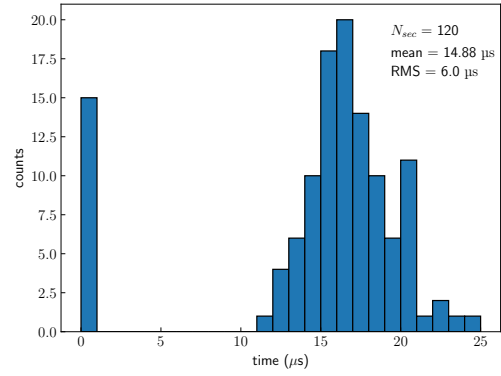
(a) $E_{Ind} = -7.25 \text{ kV cm}^{-1}$.



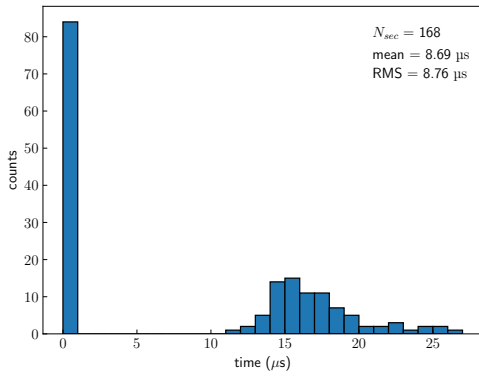
(b) $E_{Ind} = -7.5 \text{ kV cm}^{-1}$.



(c) $E_{Ind} = -7.75 \text{ kV cm}^{-1}$.



(d) $E_{Ind} = -8 \text{ kV cm}^{-1}$.

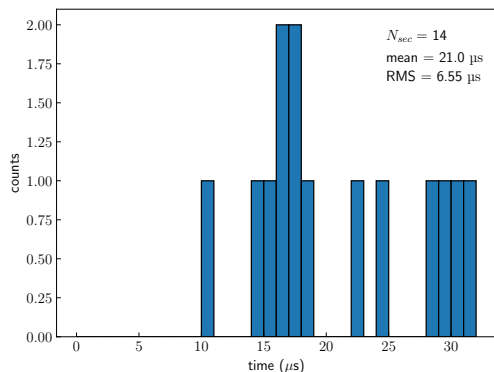


(e) $E_{Ind} = -8.25 \text{ kV cm}^{-1}$.

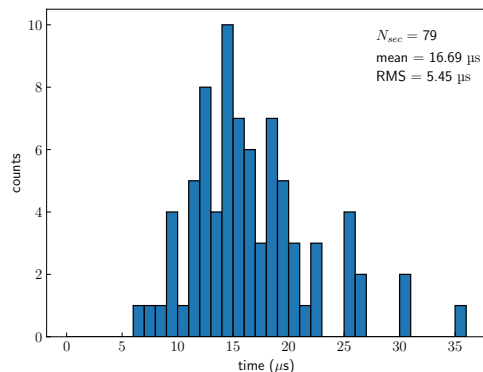
Figure C.10: Distributions of the time between primary and secondary discharge with the aluminium GEM and $R_D = 100 \text{ k}\Omega$.

C.5 Employing different gas mixtures

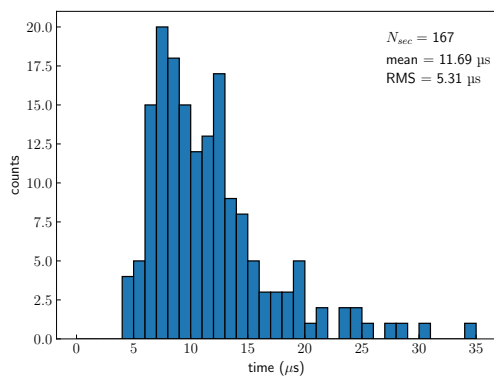
The measurements of this section correspond to the ones presented in Sec. 5.9.



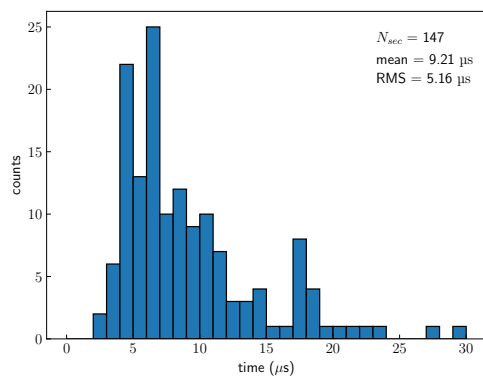
(a) $E_{Ind} = 4.75 \text{ kV cm}^{-1}$.



(b) $E_{Ind} = 5 \text{ kV cm}^{-1}$.

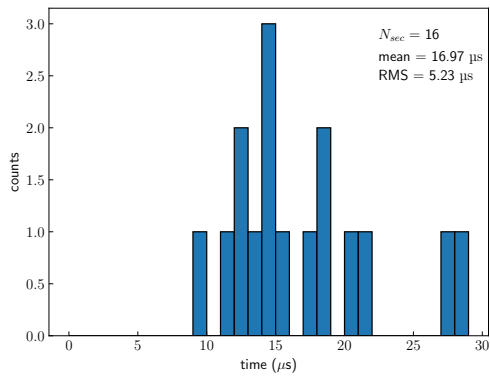


(c) $E_{Ind} = 5.25 \text{ kV cm}^{-1}$.

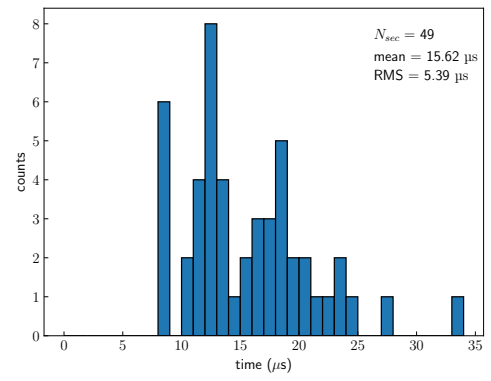


(d) $E_{Ind} = 5.5 \text{ kV cm}^{-1}$.

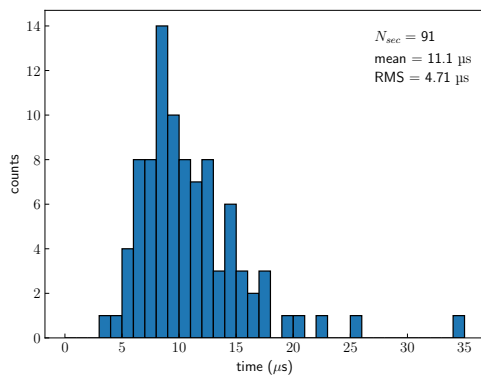
Figure C.11: Distributions of the time between primary and secondary discharge in Ar-CO₂ (90-10).



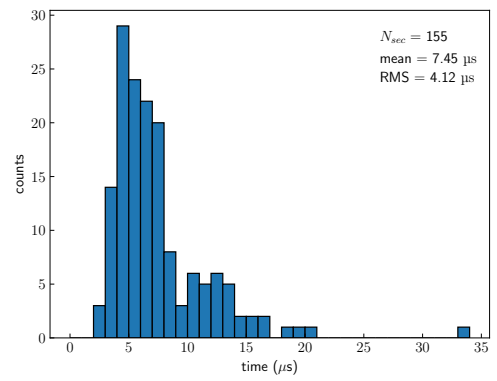
(a) $E_{Ind} = 5.25 \text{ kV cm}^{-1}$.



(b) $E_{Ind} = 5.5 \text{ kV cm}^{-1}$.

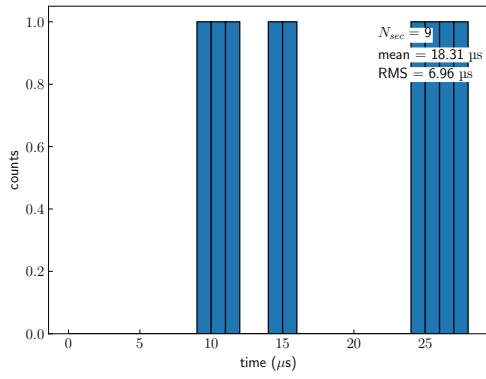


(c) $E_{Ind} = 5.75 \text{ kV cm}^{-1}$.

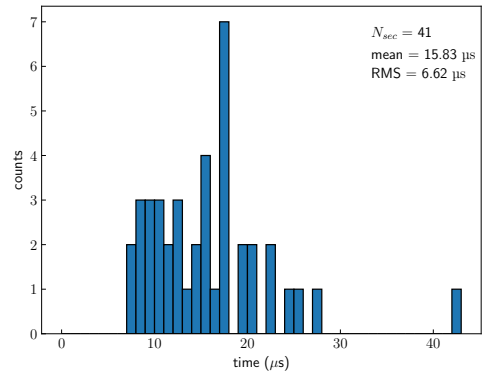


(d) $E_{Ind} = 6 \text{ kV cm}^{-1}$.

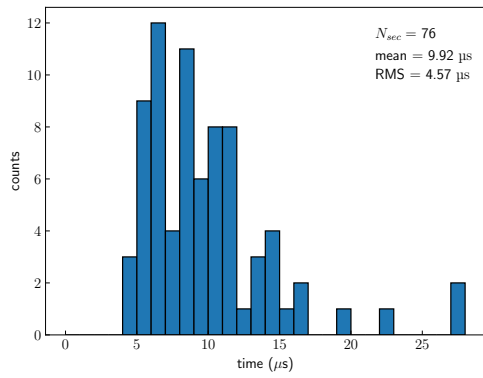
Figure C.12: Distributions of the time between primary and secondary discharge in Ar-CO₂ (85-15).



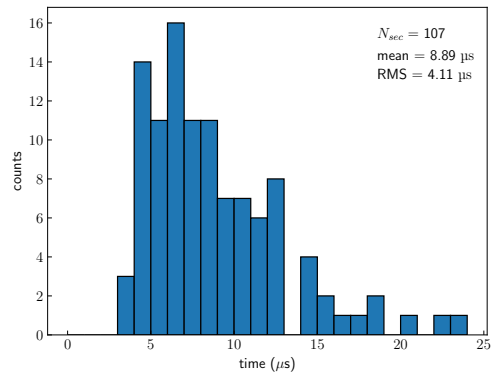
(a) $E_{Ind} = 5.75 \text{ kV cm}^{-1}$.



(b) $E_{Ind} = 6 \text{ kV cm}^{-1}$.

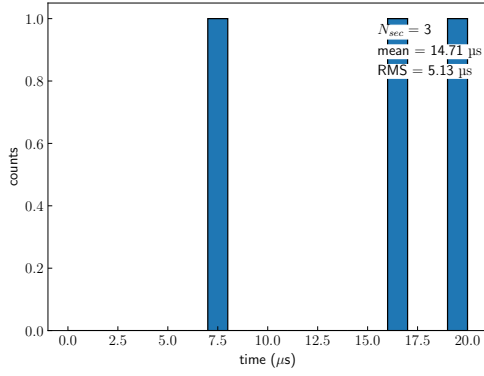


(c) $E_{Ind} = 6.25 \text{ kV cm}^{-1}$.

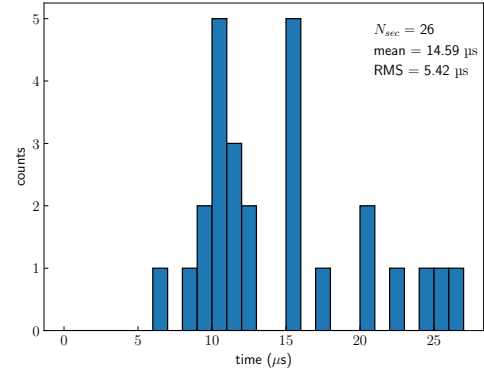


(d) $E_{Ind} = 6.5 \text{ kV cm}^{-1}$.

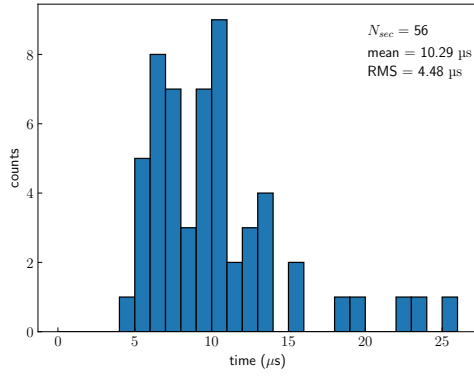
Figure C.13: Distributions of the time between primary and secondary discharge in Ar-CO₂ (80-20).



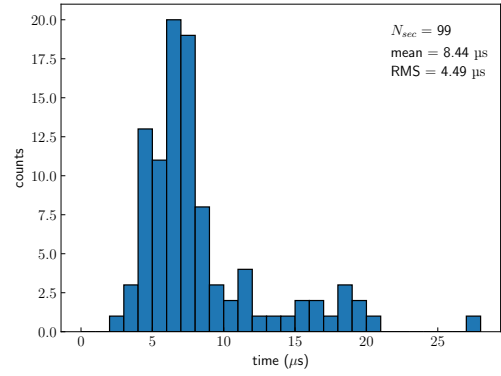
(a) $E_{Ind} = 6 \text{ kV cm}^{-1}$.



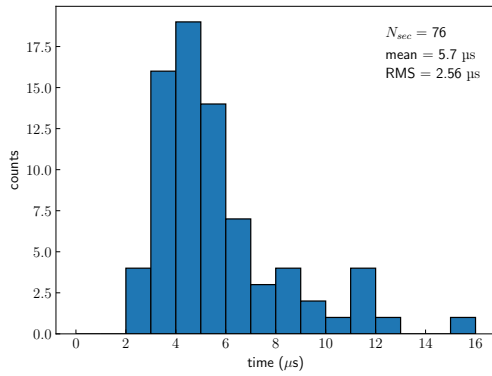
(b) $E_{Ind} = 6.25 \text{ kV cm}^{-1}$.



(c) $E_{Ind} = 6.5 \text{ kV cm}^{-1}$.

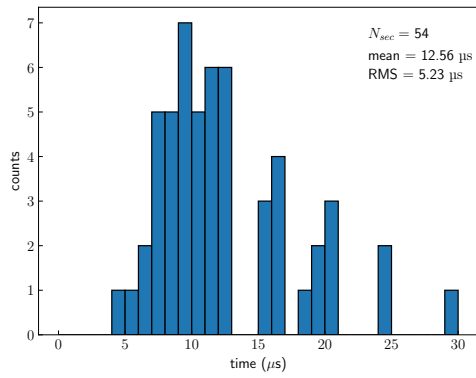


(d) $E_{Ind} = 6.75 \text{ kV cm}^{-1}$.

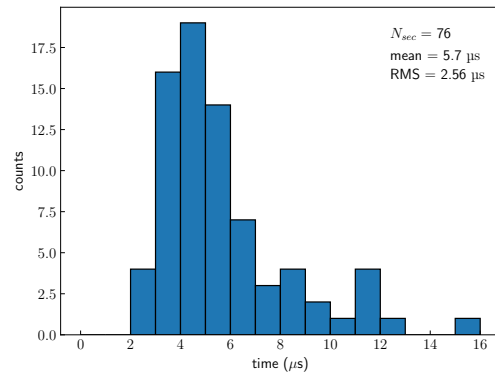


(e) $E_{Ind} = 7 \text{ kV cm}^{-1}$.

Figure C.14: Distributions of the time between primary and secondary discharge in Ar-CO₂ (75-25).

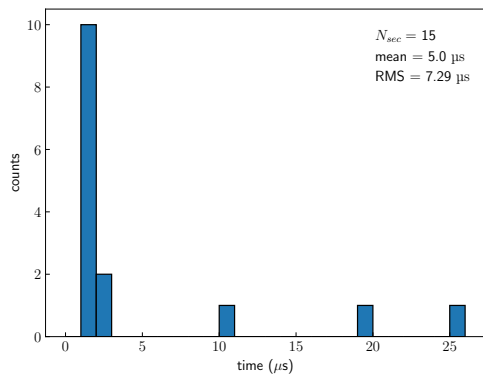


(a) $E_{Ind} = 6.75 \text{ kV cm}^{-1}$.

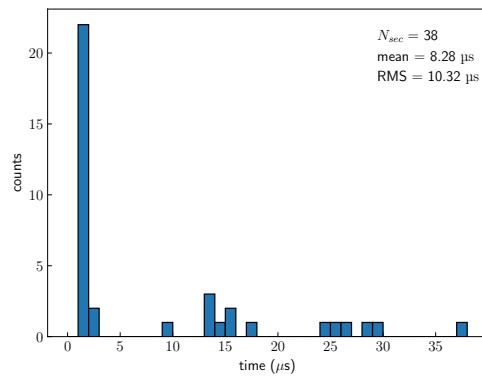


(b) $E_{Ind} = 7 \text{ kV cm}^{-1}$.

Figure C.15: Distributions of the time between primary and secondary discharge in Ar-CO₂ (70-30).



(a) $E_{Ind} = 4 \text{ kV cm}^{-1}$.



(b) $E_{Ind} = 4.25 \text{ kV cm}^{-1}$.

Figure C.16: Distributions of the time between primary and secondary discharge in Ne-CO₂-N₂ (90-10-5).

D Bibliography

- [1] The ALICE Collaboration. “The ALICE experiment at the CERN LHC”. In: *Journal of Instrumentation* 3.08 (2008), S08002. URL: <http://stacks.iop.org/1748-0221/3/i=08/a=S08002>.
- [2] Martin L. Perl, Eric R. Lee, and Dinesh Loomba. “Searches for Fractionally Charged Particles”. In: *Annual Review of Nuclear and Particle Science* 59.1 (2009), pp. 47–65. DOI: [10.1146/annurev-nucl-121908-122035](https://doi.org/10.1146/annurev-nucl-121908-122035). eprint: <https://doi.org/10.1146/annurev-nucl-121908-122035>. URL: <https://doi.org/10.1146/annurev-nucl-121908-122035>.
- [3] E. Eichten et al. “Spectrum of Charmed Quark-Antiquark Bound States”. In: *Phys. Rev. Lett.* 34 (6 Feb. 1975), pp. 369–372. DOI: [10.1103/PhysRevLett.34.369](https://doi.org/10.1103/PhysRevLett.34.369). URL: <https://link.aps.org/doi/10.1103/PhysRevLett.34.369>.
- [4] G. Parisi, R. Petronzio, and F. Rapuano. “A measurement of the string tension near the continuum limit”. In: *Physics Letters B* 128 (Sept. 1983), pp. 418–420. DOI: [10.1016/0370-2693\(83\)90930-9](https://doi.org/10.1016/0370-2693(83)90930-9).
- [5] M. Tanabashi et al. “Review of Particle Physics”. In: *Phys. Rev. D* 98 (3 Aug. 2018), p. 030001. DOI: [10.1103/PhysRevD.98.030001](https://doi.org/10.1103/PhysRevD.98.030001). URL: <https://link.aps.org/doi/10.1103/PhysRevD.98.030001>.
- [6] N. Cabibbo and G. Parisi. “Exponential hadronic spectrum and quark liberation”. In: *Physics Letters B* 59.1 (1975), pp. 67–69. DOI: [https://doi.org/10.1016/0370-2693\(75\)90158-6](https://doi.org/10.1016/0370-2693(75)90158-6). URL: <http://www.sciencedirect.com/science/article/pii/0370269375901586>.
- [7] A. Bazavov et al. “Equation of state in $(2 + 1)$ -flavor QCD”. In: *Phys. Rev. D* 90 (9 Nov. 2014), p. 094503. DOI: [10.1103/PhysRevD.90.094503](https://doi.org/10.1103/PhysRevD.90.094503). URL: <https://link.aps.org/doi/10.1103/PhysRevD.90.094503>.
- [8] Peter Braun-Munzinger and Johanna Stachel. “The quest for the quark–gluon plasma”. In: *Nature* 448.7151 (2007), p. 302.
- [9] Tapan K. Nayak. “Heavy Ions: Results from the Large Hadron Collider”. In: *Pramana* 79 (2012), pp. 719–735. DOI: [10.1007/s12043-012-0373-7](https://doi.org/10.1007/s12043-012-0373-7). arXiv: [1201.4264](https://arxiv.org/abs/1201.4264) [nucl-ex].
- [10] Michael L. Miller et al. “Glauber Modeling in High-Energy Nuclear Collisions”. In: *Annual Review of Nuclear and Particle Science* 57.1 (2007), pp. 205–243. DOI: [10.1146/annurev.nucl.57.090506.123020](https://doi.org/10.1146/annurev.nucl.57.090506.123020). eprint: <https://doi.org/10.1146/annurev.nucl.57.090506.123020>. URL: <https://doi.org/10.1146/annurev.nucl.57.090506.123020>.

- [11] B. Abelev et al. “Centrality determination of Pb-Pb collisions at $\sqrt{s_{NN}} = 2.76$ TeV with ALICE”. In: *Phys. Rev. C* 88 (4 Oct. 2013), p. 044909. DOI: [10.1103/PhysRevC.88.044909](https://doi.org/10.1103/PhysRevC.88.044909). URL: <https://link.aps.org/doi/10.1103/PhysRevC.88.044909>.
- [12] Helmut Satz. “The Quark-Gluon Plasma: A Short Introduction”. In: *Nucl. Phys.* A862-863 (2011), pp. 4–12. DOI: [10.1016/j.nuclphysa.2011.05.014](https://doi.org/10.1016/j.nuclphysa.2011.05.014). arXiv: [1101.3937](https://arxiv.org/abs/1101.3937) [hep-ph].
- [13] P. Braun-Munzinger and J. Stachel. “Charmonium from Statistical Hadronization of Heavy Quarks – a Probe for Deconfinement in the Quark-Gluon Plasma”. In: *Landolt-Börnstein - Group I Elementary Particles, Nuclei and Atoms. Vol. 23: Relativistic Heavy Ion Physics*. Ed. by R. Stock. accessed 2018-11-12. Springer-Verlag Berlin Heidelberg, 2010. DOI: [10.1007/978-3-642-01539-7_14](https://doi.org/10.1007/978-3-642-01539-7_14). arXiv: [0901.2500](https://arxiv.org/abs/0901.2500) [nucl-th]. URL: https://materials.springer.com/lb/docs/sm_lbs_978-3-642-01539-7_14.
- [14] “An overview of experimental results from ultra-relativistic heavy-ion collisions at the CERN LHC: Hard probes”. In: *Reviews in Physics* 1 (2016), pp. 172–194. DOI: <https://doi.org/10.1016/j.revip.2016.11.001>.
- [15] Francesco Noferini and ALICE Collaboration. “ALICE results from Run-1 and Run-2 and perspectives for Run-3 and Run-4”. In: *Journal of Physics: Conference Series* 1014.1 (2018), p. 012010. URL: <http://stacks.iop.org/1742-6596/1014/i=1/a=012010>.
- [16] “An overview of experimental results from ultra-relativistic heavy-ion collisions at the CERN LHC: Bulk properties and dynamical evolution”. In: *Reviews in Physics* 1 (2016), pp. 154–171. DOI: <https://doi.org/10.1016/j.revip.2016.11.002>.
- [17] E. Botta. *Particle identification performance at ALICE*. Tech. rep. Proceeding of the Fifth Annual Conference on Large Hadron Collider Physics, May 15-20, 2017, Shanghai, Cina. Sept. 2017. arXiv: [1709.00288](https://arxiv.org/abs/1709.00288). URL: <https://cds.cern.ch/record/2282027>.
- [18] J. Alme et al. “The ALICE TPC, a large 3-dimensional tracking device with fast readout for ultra-high multiplicity events”. In: *Nuclear Instruments and Methods in Physics Research A* 622 (Oct. 2010), pp. 316–367. DOI: [10.1016/j.nima.2010.04.042](https://doi.org/10.1016/j.nima.2010.04.042). arXiv: [1001.1950](https://arxiv.org/abs/1001.1950) [physics.ins-det].
- [19] K. Kleinknecht. *Detektoren für Teilchenstrahlung*. Vieweg+Teubner Verlag, 2005. DOI: [10.1007/978-3-322-82205-5](https://doi.org/10.1007/978-3-322-82205-5).
- [20] Walter Blum, Werner Riegler, and Luigi Rolandi. *Particle Detection with Drift Chambers*. 2nd ed. Particle Acceleration and Detection. Springer-Verlag Berlin Heidelberg, 2008. DOI: [10.1007/978-3-540-76684-1](https://doi.org/10.1007/978-3-540-76684-1).
- [21] Steffen Georg Weber and Anton Andronic. “ALICE event display of a Pb-Pb collision at 5.02A TeV”. General Photo. July 2016. URL: <https://cds.cern.ch/record/2202730>.

- [22] Betty Bezverkhny Abelev et al. “Performance of the ALICE Experiment at the CERN LHC”. In: *Int. J. Mod. Phys. A* 29 (2014), p. 1430044. DOI: [10.1142/S0217751X14300440](https://doi.org/10.1142/S0217751X14300440). arXiv: [1402.4476](https://arxiv.org/abs/1402.4476) [nucl-ex].
- [23] Elena Botta. “Particle identification performance at ALICE”. In: *5th Large Hadron Collider Physics Conference (LHCP 2017) Shanghai, China, May 15-20, 2017*. 2017. arXiv: [1709.00288](https://arxiv.org/abs/1709.00288) [nucl-ex].
- [24] S. Masciocchi. “Physics of particle detectors. Gaseous Detectors I and II”. Ruperto-Carola-University of Heidelberg, 2017.
- [25] Y Belikov et al. *TPC tracking and particle identification in high-density environment*. 2003. arXiv: [physics/0306108](https://arxiv.org/abs/physics/0306108) [physics.data-an].
- [26] J. Wiechula. “ALICE TPC lectures”. University of Frankfurt, 2015. URL: <http://alijatpc.web.cern.ch/alijatpc/SeminarsAndLectures/Frankfurt2015/JensWiechula/>.
- [27] C. Zhao et al. “First performance results of the ALICE TPC Readout Control Unit 2”. In: *Journal of Instrumentation* 11.01 (Jan. 2016), pp. C01024–C01024. DOI: [10.1088/1748-0221/11/01/c01024](https://doi.org/10.1088/1748-0221/11/01/c01024). URL: <https://doi.org/10.1088/1748-0221/11/01/c01024>.
- [28] *Upgrade of the ALICE Time Projection Chamber*. Tech. rep. CERN-LHCC-2013-020. ALICE-TDR-016. Oct. 2013. URL: <https://cds.cern.ch/record/1622286>.
- [29] F. Sauli. “GEM: A new concept for electron amplification in gas detectors”. In: *Nuclear Instruments and Methods in Physics Research Section A: Accelerators, Spectrometers, Detectors and Associated Equipment* 386.2 (1997), pp. 531–534. DOI: [https://doi.org/10.1016/S0168-9002\(96\)01172-2](https://doi.org/10.1016/S0168-9002(96)01172-2). URL: <http://www.sciencedirect.com/science/article/pii/S0168900296011722>.
- [30] DuPont. *DuPont™ Kapton®. Summary of Properties*. URL: <http://www.dupont.com/content/dam/dupont/products-and-services/membranes-and-films/polyimide-films/documents/DEC-Kapton-summary-of-properties.pdf> (visited on 11/15/2018).
- [31] Fabio Sauli. “The gas electron multiplier (GEM): Operating principles and applications”. In: *Nuclear Instruments and Methods in Physics Research Section A: Accelerators, Spectrometers, Detectors and Associated Equipment* 805 (2016). Special Issue in memory of Glenn F. Knoll, pp. 2–24. DOI: <https://doi.org/10.1016/j.nima.2015.07.060>. URL: <http://www.sciencedirect.com/science/article/pii/S0168900215008980>.
- [32] Marco Villa et al. “Progress on large area GEMs”. In: *Nuclear Instruments and Methods in Physics Research Section A: Accelerators, Spectrometers, Detectors and Associated Equipment* 628.1 (2011). VCI 2010, pp. 182–186. DOI: <https://doi.org/10.1016/j.nima.2010.06.312>. URL: <http://www.sciencedirect.com/science/article/pii/S0168900210015020>.

- [33] F. V. Böhmer et al. “Simulation of Space-Charge Effects in an Ungated GEM-based TPC”. In: *Nucl. Instrum. Meth.* A719 (2013), pp. 101–108. DOI: [10.1016/j.nima.2013.04.020](https://doi.org/10.1016/j.nima.2013.04.020). arXiv: [1209.0482](https://arxiv.org/abs/1209.0482) [physics.ins-det].
- [34] M. Killenberg et al. “Modeling and measurement of charge transfer in multiple GEM structures”. In: *Nucl. Instrum. Meth.* A498 (2003), pp. 369–383. DOI: [10.1016/S0168-9002\(02\)02079-X](https://doi.org/10.1016/S0168-9002(02)02079-X). arXiv: [physics/0212005](https://arxiv.org/abs/physics/0212005) [physics].
- [35] *Addendum to the Technical Design Report for the Upgrade of the ALICE Time Projection Chamber*. Tech. rep. CERN-LHCC-2015-002. ALICE-TDR-016-ADD-1. Feb. 2015. URL: <https://cds.cern.ch/record/1984329>.
- [36] A. Deisting. “Measurements of ion mobility and GEM discharge studies for the upgrade of the ALICE time projection chamber”. PhD thesis. Ruperto-Carola-University of Heidelberg, 2018.
- [37] E. Hellbär. “Ion Movement and Space-Charge Distortions in the ALICE TPC”. Master thesis. Institut für Kernphysik, Goethe-Universität, Frankfurt am Main, 2015. URL: <https://www.uni-frankfurt.de/59428504/Hellbaer-Masterarbeit.pdf>.
- [38] *ALICE selects gas electron multipliers for its new TPC*. URL: <https://cerncourier.com/alice-selects-gas-electron-multipliers-for-its-new-tpc/> (visited on 10/03/2018).
- [39] Andreas Mathis. “From gated to continuous readout - the GEM upgrade of the ALICE TPC”. In: *5th International Conference on Micro Pattern Gas Detectors (MPGD2017) Temple University, Philadelphia, USA, May 22-26, 2017*. 2018. arXiv: [1803.04140](https://arxiv.org/abs/1803.04140) [physics.ins-det].
- [40] C. Lippmann. “A continuous read-out TPC for the ALICE upgrade”. In: *Nuclear Instruments and Methods in Physics Research Section A: Accelerators, Spectrometers, Detectors and Associated Equipment* 824 (2016). Frontier Detectors for Frontier Physics: Proceedings of the 13th Pisa Meeting on Advanced Detectors, pp. 543–547. DOI: <https://doi.org/10.1016/j.nima.2015.12.007>. URL: <http://www.sciencedirect.com/science/article/pii/S0168900215015752>.
- [41] Yuri P. Raizer. *Gas Discharge Physics*. Ed. by John E. Allen. Springer-Verlag Berlin Heidelberg, 1991.
- [42] P. Fonte. *Calculation of streamer development in MPGDs in an axisymmetric hydrodynamic model*. 5th RD51 Collaboration Meeting. Freiburg, Germany, May 24, 2010. URL: https://indico.cern.ch/event/89325/contributions/2108964/attachments/1089488/1554083/Calculation_of_streamer_development.pdf.
- [43] V. Peskov and P. Fonte. *Research on discharges in micropattern and small gap gaseous detectors*. 2009. arXiv: [0911.0463](https://arxiv.org/abs/0911.0463) [physics.ins-det].

- [44] P. Gasik et al. “Charge density as a driving factor of discharge formation in GEM-based detectors”. In: *Nuclear Instruments and Methods in Physics Research Section A: Accelerators, Spectrometers, Detectors and Associated Equipment* 870 (2017), pp. 116–122. DOI: <https://doi.org/10.1016/j.nima.2017.07.042>. URL: <http://www.sciencedirect.com/science/article/pii/S0168900217307878>.
- [45] Filippo Resnati. *Effects of space charge in GEM-based detectors*. RD51 Collaboration Meeting and the “MPGD Stability” workshop. Technical University of Munich, June 18–22, 2018. URL: https://indico.cern.ch/event/709670/contributions/3008617/attachments/1672143/2683052/RD51_2018.pdf.
- [46] S. Bachmann et al. “Discharge studies and prevention in the gas electron multiplier (GEM)”. In: *Nuclear Instruments and Methods in Physics Research Section A: Accelerators, Spectrometers, Detectors and Associated Equipment* 479.2 (2002), pp. 294–308. DOI: [https://doi.org/10.1016/S0168-9002\(01\)00931-7](https://doi.org/10.1016/S0168-9002(01)00931-7). URL: <http://www.sciencedirect.com/science/article/pii/S0168900201009317>.
- [47] A. Datz. “Studies on Secondary Discharges and their Mitigation with a two GEM detector”. Bachelor thesis. Ruperto-Carola-University of Heidelberg, 2017.
- [48] A. Deisting et al. *Secondary discharge studies in single and multi GEM structures*. Submitted to NIM A. 2019. arXiv: 1901.06035v2 [physics.ins-det].
- [49] J. A. Merlin, P. Thuiner, and M. Gruchala. *Effect of discharges on GEM detectors - Single Hole Setup*. RD51 Collaboration Meeting and the “MPGD Stability” workshop. Technical University of Munich, June 18–22, 2018. URL: https://indico.cern.ch/event/709670/contributions/3008626/attachments/1672294/2683230/JMERLIN_RD51ColMeeting_GEM_DischargeEffects_24052018.pdf.
- [50] P. Gasik. *Discharge Studies with single- and multi-GEM Structures in a scope of the ALICE TPC Upgrade*. Talk at the RD51 Collaboration Meeting. Mar. 2016. URL: https://indico.cern.ch/event/496113/contributions/2008281/%20attachments/1242032/1827187/gasik_11032016_sparks_RD51.pdf.
- [51] Antonija Utrobičić, Marinko Kovačić, and Mirko Planinić. *Usage of single hole THGEM foil for delayed discharge propagation analysis*. RD51 Collaboration Meeting and the “MPGD Stability” workshop. Technical University of Munich, June 21, 2018. URL: https://indico.cern.ch/event/709670/contributions/3027853/attachments/1672132/2682893/Discharge_propagation_THGEM_v2.pdf.
- [52] P. Gasik. *Discharge propagation studies with a single GEM in various Ar- and Ne- based gas mixtures*. Talk at the ALICE TPC Upgrade Meeting. Mar. 2016. URL: https://indico.cern.ch/event/496488/contributions/2016582/attachments/1247147/1837245/gasik_22032016.pdf.

- [53] L. Lautner and P. Gasik. *Secondary discharge mitigation by HV scheme optimisation*. RD51 Collaboration Meeting and the “MPGD Stability” workshop. Technical University of Munich, June 21, 2018. URL: https://indico.cern.ch/event/709670/contributions/3008618/attachments/1672022/2682672/RD51_Stability_Workshop_HVschemeOpt_21062018.pdf.
- [54] P. Gasik. *Resistor studies*. Talk at the ALICE TPC project review. Sept. 2016. URL: <https://indico.cern.ch/event/563976/>.
- [55] CAEN. *MOD. N 470 4 CHANNEL PROGRAMMABLE H.V. POWER SUPPLY*. 2002. URL: http://www.tunl.duke.edu/documents/public/electronics/CAEN/caen_n470.pdf (visited on 11/23/2018).
- [56] CAEN. *MOD. N 471 2 FOLD H.V. POWER SUPPLY*. 2002. URL: http://www.tunl.duke.edu/documents/public/electronics/CAEN/caen_n471.pdf (visited on 11/23/2018).
- [57] *R&S® RTE Oscilloscope. User Manual*. 2018. URL: https://cdn.rohde-schwarz.com/pws/dl_downloads/dl_common_library/dl_manuels/gb_1/r/rte_2/RTE_UserManual_en_14.pdf (visited on 11/24/2018).
- [58] T. E. Bortner and G. S. Hurst. “Ionization of Pure Gases and Mixtures of Gases by 5-Mev Alpha Particles”. In: *Phys. Rev.* 93 (6 Mar. 1954), pp. 1236–1241. DOI: 10.1103/PhysRev.93.1236. URL: <https://link.aps.org/doi/10.1103/PhysRev.93.1236>.
- [59] P. M. M. Correia et al. “A dynamic method for charging-up calculations: the case of GEM”. In: *JINST* 9 (2014), P07025. DOI: 10.1088/1748-0221/9/07/P07025. arXiv: 1401.4009 [physics.ins-det].
- [60] Claude A. Pruneau. *Data Analysis Techniques for Physical Scientists*. Cambridge University Press, Oct. 2017. DOI: 10.1017/9781108241922.
- [61] T. Ullrich and Z. Xu. *Treatment of errors in efficiency calculations*. 2007. arXiv: physics/0701199 [physics.data-an].
- [62] *ROOT Data Analysis Framework*. URL: <https://root.cern.ch> (visited on 12/10/2018).
- [63] Michael Galarnyk. *Understanding Boxplots*. URL: <https://towardsdatascience.com/understanding-boxplots-5e2df7bcbd51> (visited on 01/29/2018).
- [64] *Website of the EP-DT-DD Micro-Pattern Technologies (MPT) service*. URL: <https://ep-dep-dt.web.cern.ch/micro-pattern-technologies> (visited on 12/09/2018).
- [65] John R. Rumble, ed. *CRC Handbook of Chemistry and Physics*. 99th. CRC Press, 2018.
- [66] *Python 2.7.15 documentation*. URL: <https://docs.python.org/2.7/> (visited on 12/20/2018).

- [67] Stephen Biagi. “Magboltz 2”. In: *CERN computer newsletter No.2000-001 in section 'Scientific Applications and Software Engineering'* (Apr. 2000). URL: <http://cds.cern.ch/record/1018382>.
- [68] Alexander Deisting, Chilo Garabatos, and Alexander Szabo. “Ion mobility measurements in Ar-CO₂, Ne-CO₂, and Ne-CO₂-N₂ mixtures, and the effect of water contents”. In: *Nuclear Instruments and Methods in Physics Research Section A: Accelerators, Spectrometers, Detectors and Associated Equipment* 904 (2018), pp. 1–8. DOI: <https://doi.org/10.1016/j.nima.2018.07.008>.

Erklärung:

Ich versichere, dass ich diese Arbeit selbstständig verfasst habe und keine anderen als die angegebenen Quellen und Hilfsmittel benutzt habe.

Heidelberg, den (Datum)